THE BEHAVIOUR OF THE L3 MUON CHAMBERS IN A MAGNETIC FIELD

JOHANNES ONVLEE

THE BEHAVIOUR OF THE L3 MUON CHAMBERS IN A MAGNETIC FIELD

ACADEMISCH PROEFSCHRIFT

TER VERKRIJGING VAN DE GRAAD VAN DOCTOR AAN DE UNIVERSITEIT VAN AMSTERDAM, OP GEZAG VAN DE RECTOR MAGNIFICUS PROF. DR. S. K. THODEN VAN VELZEN IN HET OPENBAAR TE VERDEDIGEN IN DE AULA DER UNIVERSITEIT (OUDE LUTHERSE KERK, INGANG SINGEL 411, HOEK SPUI), OP DONDERDAG 7 SEPTEMBER 1989 TE 15.00 UUR.

door

JOHANNES ONVLEE

geboren te Sumba (Indonesië)

Promotores : Prof. Dr. D. Harting

Prof. J. Branson

The work described in this thesis is part of the research program of the "Nationaal Instituut voor Kernfysica en Hoge-Energie Fysica (NIKHEF-H)" in Amsterdam. The author was financially supported by the "Stichting voor Fundamenteel Onderzoek der Materie (FOM)"

Aan mijn ouders, die me hebben leren rekenen en schrijven.

Contents

Chapter 1

The L3 detector

1.1 Introduction

The subject of high energy physics is the study of the ultimate constituents of matter and the fundamental interactions between them. Experiments are carried out by colliding a high energy particle beam with a fixed target or with another particle beam and studying the reaction products. High energy is desirable for two reasons: firstly, because one needs radiation with extremely short wavelengths to study the small scale of distances associated with the elementary constituents of matter, and secondly because many of the fundamental particles have large masses and require correspondingly high energies for their creation and study. The Large Electron Positron (LEP) facility, which is scheduled to start operation in the middle of 1989, is one of the latest colliders developed for experimental high energy physics. Bunches of electrons (e^-) and positrons (e^+) with a maximum beam energy of 55 GeV circulate in opposite directions through a beam pipe with a circumference of 27 km. More than 3000 bending magnets and almost 2000 focussing and correction magnets keep the beams in place.

L3 is one of the four detectors built for the LEP facility at CERN. The detector was originally proposed and accepted in 1982 [1], and has been under construction since then. It is expected that physics experiments will begin soon after the startup of the LEP machine in the middle of 1989.

Historically, most of the major discoveries at particle accelerators were totally unpredicted at the time of their construction. Independent of any theoretical speculations, recent history shows that major discoveries in particle physics from both proton accelerators and e^+e^- colliding beams have been made with detectors specially designed to measure very precisely both the lepton and the photon channels. This is because the single photon and/or leptonic channels provide a clean signal with a small background which is easy to understand and to control. The discovery of several new particles such as $J/\Psi, \Upsilon, \tau$ and Z_o, was possible only because the mass resolution of the detectors reached $\Delta M/M \leq 2\%$ [1][2][3][4][5][6].

The L3 detector was therefore designed with strong emphasis on high precision lepton measurements. The special qualities of the L3 detector are: 1) good charge identification

up to 50 GeV with the central tracking detector, 2) high precision electron and photon energy measurement with the electromagnetic calorimeter, 3) high precision muon momentum measurement and 4) measurement of hadronic jets with the hadron calorimeter.

Realistic aims are:

- Determination of the sign of the electric charge for all charged particles
- Electromagnetic energy resolution for photons and electrons of 5% at 200 MeV, down to 1% for energies larger than 3 GeV .
- 2% muon momentum resolution for muons of 45 GeV.
- Determination of hadron energies with $50\%/\sqrt{E}$ resolution.

The L3 collaboration involves some 400 physicists from 32 institutes in 13 different countries [7]. The work described in this thesis is only a small contribution to the huge effort put in the construction and optimization of the detector. Many people have contributed to the effort in the test beam experiment described in chapters 4 and 5 of this thesis. Without their help much of the work described in this thesis would not have been possible.

1.2 The L3 detector

The e^- and e^+ beams intersect at four "interaction points" where interactions between the particles will take place. The L3 detector is situated at the second interaction point (IP2), 60 meters under ground at the foot of the Jura mountains in France. The e^-e^+ interactions result in energetic reaction products which become accessible to experiment by their interaction with the detector material. Detectors are usually complex structures with many different subdetectors, each specialized in measuring a specific type of particle or an important physical quantity. Physical quantities of interest are the momenta, energies and the charges of the particles, and, where possible, the type of particle. Using these data and the statistical distributions related to these quantities, the properties of the interactions between the primary e^+ and e^- particles can be investigated.

In the next section some of the detection techniques used in L3 are described, with emphasis on the detection of muons in the different L3 subdetectors.

1.2.1 Detection techniques in colliding beam experiments

In a typical colliding beam experiment one can distinguish two main classes of apparatus: the "total absorption detectors" or calorimeters which can measure the direction and the

energy of charged and uncharged particles, and "tracking detectors" which accurately trace the track of a charged particle.

In a calorimeter the particle deposits all its energy in the form of a shower of lower-energy particles. The original properties of the detected particle are changed drastically during this process. The position and the total energy of the shower can be determined and often the type of particle can be deduced from the shape of the shower. The detector is constructed in such a way that a certain fraction of the deposited energy is converted to a measurable signal such as light or electrical charge. If this fraction is constant, the signal is proportional to the energy of the incoming particle. Electromagnetic calorimeters, for the detection of photons and electrons, are often made from a homogeneous material like NaI or BGO. These materials are very good absorbers for electromagnetic energy and transparent for the light produced in the shower. The main interaction processes at high energy are pair creation and bremsstrahlung, that give well behaved and well understood "signals" which allow high resolutions. Hadronic calorimeters are usually built as sampling devices consisting of absorber layers (Fe,Cu,U) interleaved with transparent layers like scintillators or drift chambers. The absorber layers produce the shower which is converted to a measurable signal in the transparent layers. In these calorimeters strong interactions with the nuclei play the most important role. This results in complex reactions and many different types of secondary particles, all behaving differently in the detector medium. This complexity strongly limits the achievable accuracies and resolutions.

The second class of detectors, the tracking detectors, are as transparent as possible so that the trajectory and the other properties of the particles are not disturbed. However, the Coulomb field of the charged particles interacts sufficiently with the atomic electrons to produce a track of ionized atoms. The created electrons and ions are collected such, that the position and time of their creation can be reconstructed. From these data the track of the crossing charged particle can be found. If the detector is situated in a magnetic field the momentum of the particle can also be determined from the track curvature.

Some examples of tracking detectors are wire chambers and silicon microstrips. In wire chambers the created electrons drift towards an anode plane where charge amplification takes place and the signal is measured. From the arrival times of these signals the original track can be reconstructed. In silicon microstrip detectors the ionization electrons change the electrical properties of a strip which results in a detectable signal. Combining many strips in different planes will result in a measurement of the track.

1.2.2 Detection techniques used in L3

The global right-handed cartesian coordinate system of L3 is defined as follows: the z-direction is the direction of the e^- beam, and the y-direction is vertically upwards.

The origin is chosen to be the interaction point at the center of the detector. Often the corresponding cylindrical coordinates (r, ϕ, z) are used. The angle of a track with respect to the positive z-axis is denoted by θ.

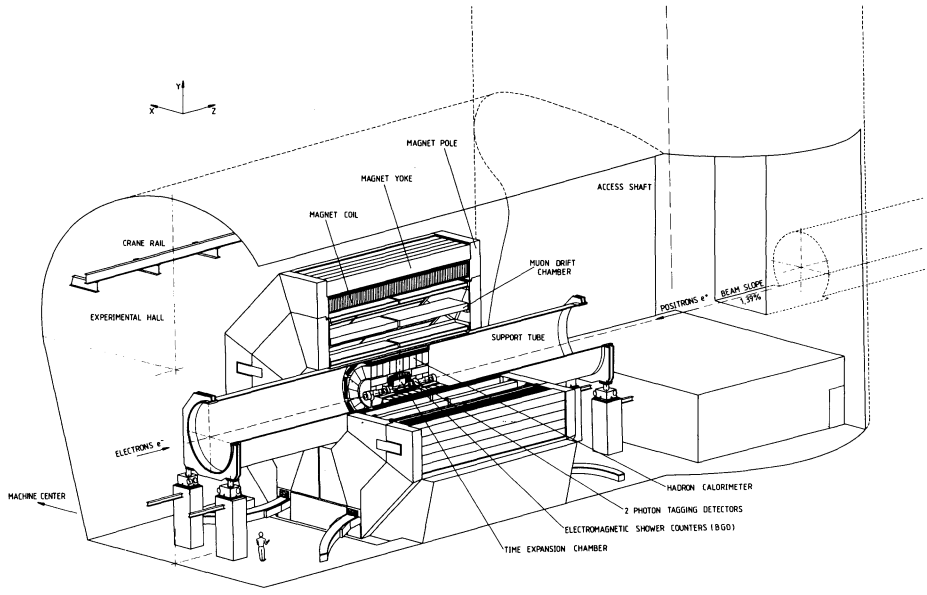

Figure 1.1: Perspective view of the L3 detector. Starting from the interaction point there are the Time Expansion Chamber (TEC), the electromagnetic calorimeter, the hadron calorimeter, the muon chambers, the aluminum coil and the return yoke of the magnet.

Figure 1.1 gives a schematic overview of the L3 detector. All the detector components are situated inside a magnetic cave, roughly 11 meters in diameter and 12 meters long. A magnetic field of $\approx$ 0.5 T (5000 gauss) is produced throughout this volume by a current of 30 kA in an octogonal helical coil surrounded by a one meter thick iron return yoke. Steel doors at both ends improve the field homogeneity. The detector components are kept in place by a support tube with an inner diameter of 4.45 meter, centered in the magnet parallel to the beam direction. Inside this tube the inner detector is situated, and on the outside the muon spectrometer is mounted.

Secondary particles produced in the e^-e^+ collisions moving out from the interaction point, first encounter the 4 mm thick beryllium beam pipe with a diameter of 18 cm. A

time expansion chamber (TEC) with a length of 110 cm and a diameter of 93 cm is built directly around the beam pipe. The TEC measures the track segments of all the crossing charged particles. These segments, curved due to the magnetic field, are used to determine the sign of the charge and the direction of the particle's momentum fourvector near the vertex point. The electromagnetic (EM) calorimeter consists of bismuth germanium oxide (BGO) crystals which absorb the photons and electrons and measure their shower structure and total energy. The energy of the hadrons is measured partly in the BGO, but mainly in the uranium/gas hadron calorimeter surrounding the BGO.

Three layers of muon chambers outside the support tube, between a radius of 2.5 meter and a radius of 5.5 meters, form the muon spectrometer. The φ position of the curved muon track is measured very accurately for three r values in the three layers of "p-chambers". From these measurements the momentum is deduced. The z-coordinate of the track is measured by four layers of "z-chambers" mounted on the top and bottom of the inner and outer p-chamber layers.

In the next section the detectors and the important parameters are described in more detail.

1.2.3 The magnet

The magnetic field is only used for charge and momentum measurements inside the TEC and the muon-spectrometer. The resolving power of a magnetic spectrometer is proportional to BL^2, where B is the magnetic field strength and L the length of the particle trajectory in this field. To improve the resolving power of a spectrometer one can either increase the field or increase the path length. The last option is more effective, because the resolving power depends on the square of the path length. L3 has chosen for a large warm magnet ($L \approx 2.9$ m for muons), with a relatively low field strength of 0.5T. The main components of the L3 magnet are the coil, the yoke and the doors. The aluminum, octagonal coil has an inner radius of 5.93 meter, an outer radius of 6.82 meter and a total length of 11.78 meter. In total there are 168 windings with a cross-section of 89 cm $\times$ 6 cm. For a field of 0.5 T a current of 30 kA is required, which corresponds to a power consumption of 4 MW and a total stored energy of 160 MJ. The return yoke consists of an octagonally shaped steel cylinder surrounding the coil and has an inner radius of 7 meter and an outer radius of 7.9 meter. The yoke is closed at each end by a 1 m thick door which fits around the support tube. The total weight of coil, yoke and support tube is 7810 tonnes.

For the off-line event reconstruction and analysis it is convenient when the magnetic field is homogeneous. The main field distortions are caused by the large holes in the two doors, and by the gaps surrounding the doors. In order to keep local field inhomogeneities small inside the detector, the amount of magnetic material inside the coil is kept as small as possible. The main pieces of magnetic material inside the coil are the supports for

the quadrupole beam magnets inside the support tube and the large rollers to move the inner detector and the muon detector along the support tube. The estimated range over which the field will be distorted more than 20 gauss by these rollers is $\approx$ 50 cm and extends only into the small part of the MI chambers next to the rollers. Smaller pieces of magnetic material near the muon chambers are the gauge blocks used in the vertical alignment system (see section 1.3.1). The effect of these small pieces on the magnetic field can be ignored.

1.2.4 Central tracking detector (TEC)

The Time Expansion Chamber (TEC) has an inner diameter of 18cm and an outer diameter of 93 cm. The gas filling is a mixture of 80% CO_2 and 20% isobutane at 2 atmospheres pressure.The detector is subdivided in an inner ring of 12 segments with 8 sense wires each and an outer ring of 24 segments with 54 sense wires per segment. The 1584 sense wires are read out by 100 MHz 6 bit ADCs which have excellent multi-hit capability. A special feature of the detector is the low drift velocity of 6 μm /ns ($\approx$ 10 times smaller than for conventional chambers) and the low diffusion. The expected track resolution is 40 μm , which has been achieved in test runs using a prototype chamber [8]. The z-coordinate of the track is measured in the z-chamber surrounding the TEC. It consists of 2 cylindrical proportional chambers, with cathode plane readout.

1.2.5 Electromagnetic calorimeter

The calorimeter of L3 is subdivided into an inner electromagnetic (EM) calorimeter and an outer hadron calorimeter. The EM calorimeter consists of $\approx$ 12000 bismuth germanium oxide (BGO) crystals pointing towards the interaction point and fills the space between 50 cm and 85 cm radius. The tapered BGO crystals are 24 cm long and measure 2x2 cm^2 at the inside and 3x3 cm^2 at the outside. All crystals are equipped with 2 photodiodes, each with a total active area of 1.5 cm^2. The detector is subdivided into two barrels of $\approx$ 4000 crystals each and two endcaps of $\approx$ 2000 crystals each. The endcaps will not be available before 1990. The barrel covers the polar range of $42^o \leq \theta \leq 138^o$ with small gaps where the two barrel pieces meet.The endcaps cover the ranges $12^o \leq \theta \leq 42^o$ and $138^o \leq \theta \leq 168^o$. Almost the full azimuthal range of $0^o \leq \varphi \leq 360^o$ is covered.

BGO was chosen because of its superior properties compared to other commonly used materials like NaI. It is not hygroscopic, has a good radiation resistance and a high energy resolution. BGO is the best material available to obtain the extremely high resolution for dilepton mass measurements aimed at in L3.

1.2.6 Hadron calorimeter

The hadron calorimeter fills up the space between the BGO and the support tube, between 88 cm and 213 cm radius. Mechanically the HC is subdivided into the barrel, the endcaps and the muon filter. The barrel consists of 9 rings of 16 modules each, and covers the polar range $35^\circ \leq \theta \leq 145^\circ$. Each of the two endcaps consists of three separate rings. They cover the ranges $5.5^\circ \leq \theta \leq 35^\circ$ and $145^\circ \leq \theta \leq 174.5^\circ$. Each module consists of about 60 uranium plates (5 mm thick, Ni coated) interleaved with 5 mm thick proportional chambers. By arranging alternate wire planes orthogonally one can determine the position of particles traversing a module. The muon filter is mounted on the inside wall of the support tube and adds 1 interaction length to the hadron calorimeter. It consists of 8 identical octants, each consisting of six 1 cm thick, 4 m long brass absorber plates interleaved with proportional chambers. Charge division readout is used in three of these chambers to determine the z coordinate of the particles. The muon filter reduces punch-through into the muon spectrometer.

The BGO and hadron calorimeters together represent 6-7 interaction lengths for hadrons. An energy resolution of $55/\sqrt{E} + 5\%$ for the hadron calorimeter has been measured in a test beam [9].

1.2.7 Muon spectrometer

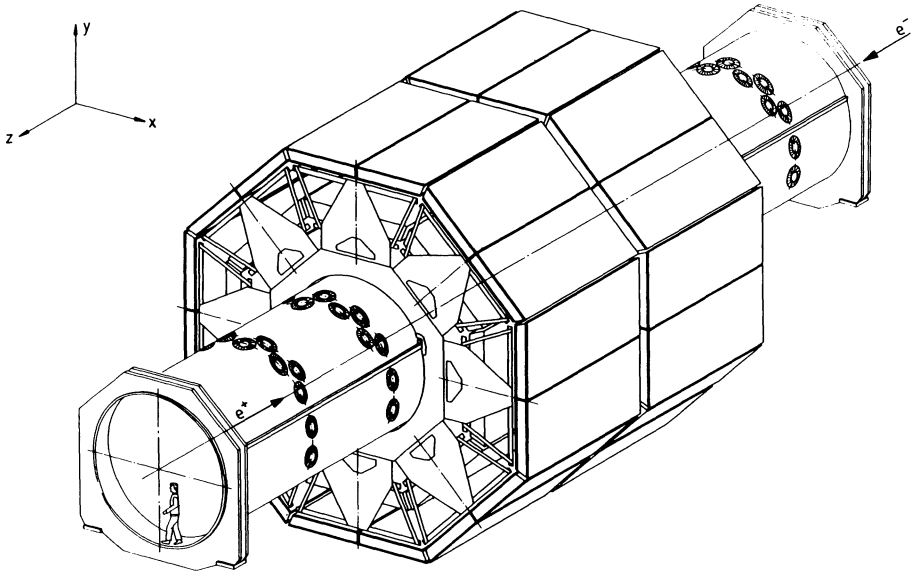

Figure 1.2: The L3 muon detector

The muon spectrometer is mounted around the support tube. The spectrometer is subdivided into 16 independent "octants" mounted on two "ferris wheels", one at each side of the interaction point. Figure 1.2 shows a cross section of the muon detector. In total there are 80 precision drift chambers divided over the muon inner layer (MI-chambers), the middle layer (MM-chambers) and the outer layer (MO-chambers) of the muon detector. The 1696 sense wires of an octant are connected to hybrid preamplifiers which are mounted on the chambers. The balanced output of these amplifiers is connected via cables to a discriminator where the signal is converted to ECL logic levels. The discriminator level will depend on the noise level and will have a value between 10 - 30 mV. The output of each discriminator is connected to a LeCroy common stop Fastbus Time to Digital Converter (TDC), again via cables. The TDCs have a time binning of 2ns. The gas in the muon chambers consists of 61.5% Argon and 38.5% Ethane.

1.2.8 Muon detection in the subdetectors

One of the important aims of L3 is the accurate measurement of high energy muon momenta. In the TEC the muon results in a track segment, in the BGO and hadron calorimeter in a position and energy loss measurement, and in the muon spectrometer in three accurate track segments. In the next subsection the muon detection in the different subdetectors is presented. The detection of muons in the muon spectrometer is discussed separately in the next section.

In the TEC, the muon leaves a trail of ionization pairs, which results in a series of signals in the flash ADCs. From the ADC data the track segment can be reconstructed with a resolution of 40 μm .

In the BGO the muon loses only a small amount of its energy. The average energy loss for minimum ionizing muons has been measured in a test beam and varies from 224 ± 5 MeV at 2 GeV to 249 ± 3 MeV for 50 GeV muons [10]. In principle the muon energy loss in BGO can be measured accurately (to better than 10%), but since the muon signal is very small compared to the signal of other particles like photons , electrons and hadrons, this measurement is only possible if the muon track is well separated from other particle tracks. If other particles are present, the average energy loss measured in the test beam can be used.

The L3 Monte Carlo program was used to calculate the energy loss for 50 GeV muons. The results are shown in figure 1.3. Most of the energy loss of a muon takes place in the hadron calorimeter. For 50 Gev muons the average total energy loss is about 3 GeV. The long tail towards high energy losses in figure 1.3 is due to the hard Brehmsstrahlung originating in the interaction of the muon with the coulomb field of the nuclei in the uranium plates.

The hadron calorimeter is not designed to measure muon energy loss accurately. A

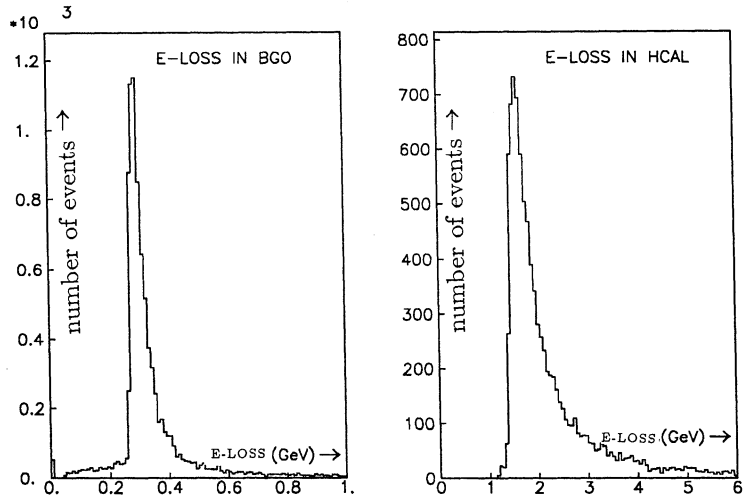

Figure 1.3: Muon energy loss in the electromagnetic calorimeter (left) and in the hadron calorimeter (right).

large signal in the hadron calorimeter only indicates that hard Brehmsstrahlung took place, but accurate measurement of the energy loss is not possible. Just like in the BGO detector, the muon-jet separation has to be good in order to be able to measure the muon signal at all. If the muon signal can not be disentangled from the data, the most probable energy loss as calculated from the Monte Carlo can be used. Note that the error on this value can be very large because of the long tail in the distribution. Tests with a large sample of Monte Carlo generated muon events showed that, if events with an energy loss > 5 GeV are discarded, the hadron calorimeter energy loss only increased the muon momentum resolution with ≈ 15 % [11].

1.3 Muons in the L3 muon spectrometer

The sagitta s of a circular track segment between 2 points is defined as the maximum deviation of the curve from the straight line connecting these two points [12]. From the three muon track segments measured in the three muon chamber layers one can calculate the sagitta of the muon track in the muon spectrometer. The transverse momentum of the muon is given by the expression:

$$p_t = \frac{0.3 \cdot BL^2}{8 \cdot s} \tag{1.1}$$

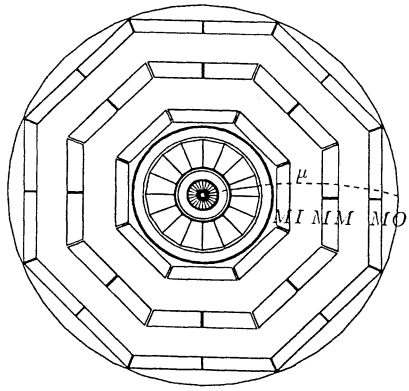

Figure 1.4: End view of the L3 detector showing the three chamber layers of the muon spectrometer outside the support tube. The momenta of muons will be determined by measuring the curvature of the muon tracks within the spectrometer.

where L is the distance between the inner and the outer chamber layers. The lengths s and L are expressed in meters, the magnetic field B in Tesla and p_t in GeV/c. The projection of the track on the r-z plane is a straight line, measured by the z-chambers. The intrinsic resolution of the z-chambers is of the order of 600 μm and systematic errors in the positioning of the z layers on the p-chambers can be of the order of 1 mm. Assuming that these errors add quadratically, one can estimate that the error in the θ angle of the track is $\approx$ 750 μrad.

For a 45 GeV muon the sagitta is 3.7 mm. Since $\Delta p/p = \Delta s/s$, this implies that, to reach the required 2% momentum resolution at 45 GeV the total error Δs in the sagitta measurement must be less than 70 μm . There are many sources of errors that contribute to Δs. The main contributions are:

- the multiple scattering in the region between the chambers Δs_{ms}
- the systematic error Δs_{sys}
- the intrinsic chamber resolution of the muon chambers Δs_{ch}.

Since the position of the track must be calculated from the TDC values measured for the individual sense wires, one needs good knowledge of the drift properties of the chambers and of the relative positions of the wires. The properties of the relation between the

recorded drift time and the position in the drift cell are the the subject of chapter 4. A schematic description of the alignment of the wires of the muon detector is the subject of the next section.

The multiple scattering error has been estimated to be $\Delta s_{ms} \approx 30\,\mu$m for a $p = 45$ GeV/c muon [12]. The sagitta is calculated from the average points found in the three muon chamber layers

$$s = \frac{1}{2}(x_{mi} + x_{mo}) - x_{mm}$$

where x_{mi}, x_{mm} and x_{mo} are the distances of the points to the central plane in the octant. From measurements with cosmic rays a single wire resolution of 150 μm was found (this number is in good agreement with the resolutions presented in chapter 5 of this thesis). Using the multiple sampling technique (16 wires in the inner and outer chambers, 24 wires in the middle chambers) described in [13] gives resolutions $\varepsilon_{mi} = \varepsilon_{mo} = 40\,\mu$m and $\varepsilon_{mm} = 32\,\mu$m for the three chamber points x_{mi}, x_{mo} and x_{mm}. The intrinsic chamber resolution is therefore:

$$\Delta s_{ch} = \left[\left(\frac{\varepsilon_{mi}}{2}\right)^2 + \left(\frac{\varepsilon_{mo}}{2}\right)^2 + \varepsilon_{mm}^2\right]^{1/2} \approx 43\,\mu\text{m}$$

If $\Delta s_{ch}, \Delta s_{ms}$ and Δs_{sys} are added in quadrature, one finds that Δs_{sys} must be less than 30 μm in order to obtain the required momentum resolution.

In order to keep the total systematic error below 30 μm , each individual systematic error has to be much smaller. It is not simple to exactly define all the systematic errors, or to set accurate acceptable limits: different sources of systematic errors will enter in statistically quite different ways, and the total number of different contributions depends on the way they are split up. In this thesis different sources of systematic errors are pointed out, and an upper limit of 10 μm for each individual contribution is used. For instance, an error in the magnetic field will cause an error in the drift angle, and therefore in the position. The error bounds on the magnetic field are set such that the average error in the position is less than 10 μm (see chapter 2 for details). Similar arguments are used in chapter 5, where the accuracy of the drift time - drift distance relation for the muon chambers will be discussed.

1.3.1 Wire and chamber alignment.

The alignment of the wires in an octant with the required accuracy of 30 μm is not a trivial task. High precision mechanical positioning techniques are required to meet the tolerances. In this section some of the details of the alignment system are described. Further details can be found in [7],[14].

The wires of each chamber are arranged in wire planes. The wires in each plane are aligned using three sets of precision glass plates, one at each end of a chamber, and one in

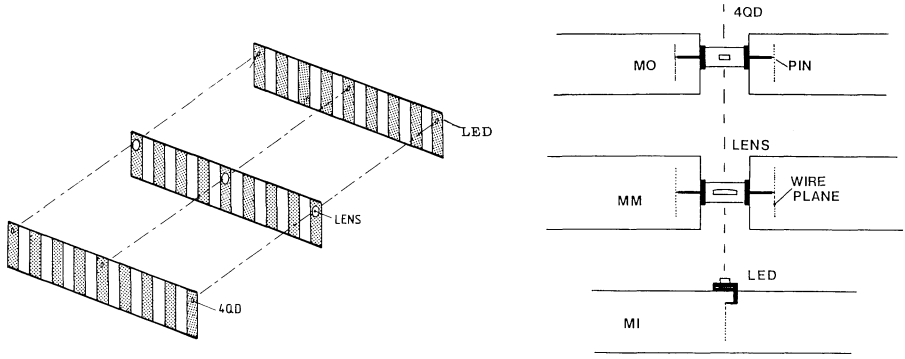

Figure 1.5: Figure (a) shows a schematic view of the carbon fibre-glass bridges mounted in a chamber with the three RASNIK alignment systems to align the wire planes in a chamber. Figure (b) shows the principle of the vertical alignment system to align the three chamber layers with respect to each other.

the middle to reduce gravitational sag (figure 1.5). Each plate has a width of 50.75 mm and supports a sense plane on one edge, and a mesh plane on the other. The flatness of the glass plate edges is better then 3 μm . The glass plates in each of the three sets are interconnected by means of a very stiff carbon fibre frame. This results in three "glass bridges" per chamber, one at each end and one in the middle of the chamber. Errors in the relative positions of the glass pieces in these frames are $\leq 2\,\mu$m .

The carbon fibre-glass bridges in the chamber are aligned using three independent opto-electrical alignment systems per chamber, mounted on the three glass bridges. Each system consist of a LED at one end, a lens on the middle bridge and a photodiode with four separate segments (four quadrant diode)[15][16] at the other end of the chamber. Light from the LED is projected through the lens onto the diode (see figure 1.6(a). From the ratios of the resulting four diode signals the center of gravity of the LED image can be determined, thus defining a straight line between the three glass bridges. In total there are 240 of these opto-electrical devices. Each system has an accuracy of 5 μm and can continuously measure the relative positions of the bridges within a range of 400 μm .

The wire planes of the two adjacent chambers in the MM and MO layers are positioned using two mechanical pins, one at each end of the chamber (see figure 1.6(b). The pins have a length of 203 mm $\pm$ 0.002 mm (exactly equivalent to the width of two cells). Each pin consists of a central gauge block carrying on each side a rod with a high precision end surface. The wire bridges of the two chambers are adjusted such that the pins are

just making electrical contact with a field wire of the first cell in the chambers. This method is sensitive to a movement of 2 μm of the wire plane with respect to the pin. The gauge blocks of the pins are used to align the different chamber layers. The gauge blocks of the two pins at the ends of the MO chamber layer contain two four-quadrant diodes and the gauge blocks of the MM layer contain a lens. Gauge blocks are also mounted on the ends of the single MI chamber, each containing two LED's. The position of these gauge blocks with respect to the wire planes of the MI chamber is also known to within 2 μm accuracy. This results in an opto-electrical vertical alignment system at each end of the octant. Each of these vertical alignment systems is duplicated for internal checks. These systems define two accurate straight reference lines for the relative alignment of the wire planes in the three chamber layers (figure 1.5). Finally these two reference lines have to be aligned such that they lie accurately in the same plane. For this purpose a laser beacon was designed [17]. A laser beam is reflected by a rotating mirror. The resulting sweeping laser beam defines a central yz-plane of the octant within an accuracy of 15 μm . The position of the six gauge blocks with respect to this plane is measured using high precision read-out strips mounted on the blocks.

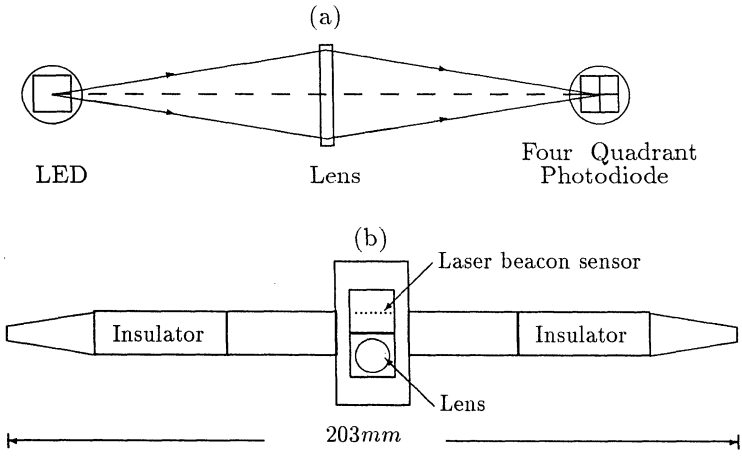

Figure 1.6: The opto-electrical alignment systems in the muon spectrometer. Figure (a) shows the LED, lens and four-quadrantdiode, as used in RASNIK and in the vertical alignment systems. Figure (b) shows the principle of the mechanical pins mounted between the two MM chambers.

The above outline already shows that there are many potential sources of error. All the octants were assembled and tested at CERN. Besides mechanical checks,the alignment was checked directly by measuring cosmic ray tracks and ionization tracks produced by

a UV laser [18]. Details on these tests can be found in [15] and [16]. The tests showed that the alignment accuracy is better than aimed for in the L3 technical proposal [19].

1.4 The L3 muon chamber drift cell

The position of the muon track in a chamber follows from the recorded drift time data through the relation $X(t)$ between the drift distance and the drift time measured by the Time to Digital Converters (TDCs). This relation is called the "cellmap function" from now on. This cellmap function depends on several physical processes at the atomic level. Some of these processes are well understood and can be predicted from first principles, others are only known empirically. In this section the design of the L3 muon chamber drift cell and its properties will be treated heuristically. No attempt will be made to explain the underlaying processes in great detail. First the cell geometry is explained and motivated. Next the properties of the gas and effects on the cellmap function are discussed. The details of the drift time - drift distance relation will be the subject of chapters 4 and 5.

1.4.1 Wire configuration and electrostatics.

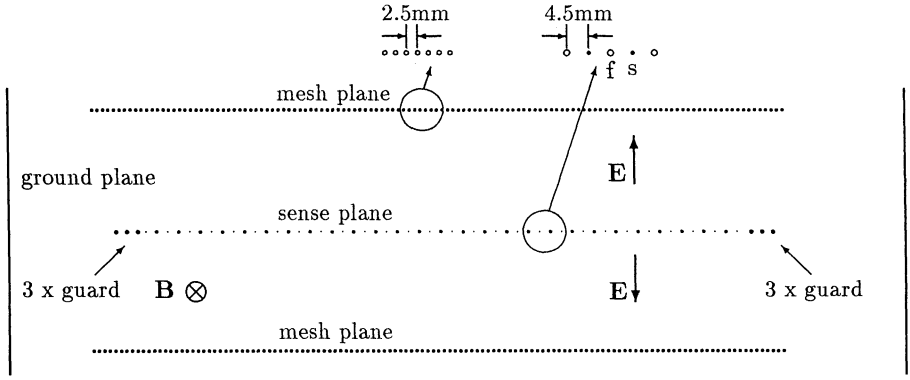

Figure 1.7: Wire configuration for the MM chambers. The MO and MI chambers are exactly the same, but with less wires. MM has 28, MO and MI have 20 sense wires.The letters f and s in the figure stand for sense and field wire.

Figure 1.7 shows a cross section of the MM drift cell. A sense wire plane consists of 30 μm W-Au sense wires spaced at 9 mm intervals, with 75 μm CuBe field wires in

between. In total there are 28 sense wires in a plane, of which only 24 are read out by the Time to Digital Converters. The two outermost sense wires on each side, together with three guard wires, are only used for field shaping. Sense wire planes are separated by mesh wire planes which consist of 96 W-Au wires, 30 μm thick and 2.25 mm apart. The distance between a sense- and a mesh plane is 50.75 mm. The MI and MO chamber cells have a similar lay-out but there are only 20 sense wires of which 16 are read out.

The top and bottom covers of the MM chambers are aluminum honeycomb panels. These panels are strong enough to withstand 20mbar over-pressure in the chamber and add only a minimal amount of material along the muon path. The covers of the MI and MO chambers consist of 6 cm thick z-chambers, which measure the z coordinate of the tracks. The multiple scattering in the z-chambers will be bigger, but the effect of scattering at the MO and MI chambers does not effect the sagitta measurements.

All the wires of the mesh planes are kept at the same (negative) voltage. The wires of the sense planes are at positive voltage, but with different settings for sense, guard and field wires. The voltages are optimized for good field homogeneity in the drift region between the planes, good gas amplification near the sense wires and equal signal development on all the sense wires and they are tabulated in 1.1. Since the introduction of a magnetic field changes the drift properties drastically, typical values are given for both **B**=0 T and **B**=0.5 T. The honeycomb panels and the z-chambers serve as an electrostatic ground. For both high voltage settings the gain is the same, and corresponds with 300 mV signals at the output of the pre-amplifiers. The voltages are chosen such that the zero voltage contour lies in the middle of the cell.

wires	B = 0T	B=0.5T
sense	3385	4350
guard	3285	4250
field	1250	2750
mesh	-2400	-3200

Table 1.1: High Voltage settings with and without magnetic field.

The electric potential and electric field distribution in a cell have been calculated with the wire chamber simulation program GARFIELD [20]. This program calculates the fields given the wire and ground plane positions and the voltages tabulated above. The resulting equations are solved assuming an infinite number of cells, which is a good approximation for the L3 muon chambers.

The outermost cells of the chambers have a special lay-out. The outer mesh plane is replaced by large printed circuit boards. The part of the boards parallel to the sense plane has a continuous conducting surface, the sloping part carries conducting strips parallel to the sense wires. The voltages of these strips are set by a resistor ladder network to a potential such that the electric potential of the strip is the same as the electrostatic

potential in a normal cell at the corresponding point. In this way the electric field distribution in the edge cells can be made very similar to that in a normal cell. However, some difference is unavoidable, because of the relatively large mechanical tolerances on the position of the printed circuit boards.

1.5 The gas filling.

The drift process for ions can be treated in a satisfactory way with classical gas theory. For ions, the drift velocity is proportional to the electrical field and can be written as $V_d^+ = \mu^+ E$, where μ^+ is the mobility of the ion in the chosen drift gas mixture. This mobility is quite insensitive to changes in the electrical field. For electrons the situation is much more complicated; the collision cross-section, the mean free path between collisions and the mean energy of the electrons, and thus the drift velocity V_x , vary drastically as function of the electrical field. This is a consequence of the fact that the electron wavelength approaches that of the electrons bound in the molecules, so that complex quantum-mechanical interactions take place. A description of all the processes can be found in [21]

Figure 1.8(a) shows the measured drift velocity V_x for the electrons for the Argon:Ethane gas mixture used in the L3 muon chambers as a function of the electric field E. For low values of E the drift velocity increases with E until a plateau is reached and then decreases. At very high fields, e.g. close to the sense wires, the drift velocity increases again. Figure 1.8(b) shows the drift velocity for high values of E as measured by F.Hartjes (see also [22]). The voltages in the chamber are set such that the drift field corresponds to the plateau in the curve shown in fig 1.8(a). This minimizes variations in V_x due to small variations in the drift field.

It appears that small changes in the gas mixture, introducing small changes in the average energy, drastically affect the drift properties of the gas. Data for many types of gases can be found in the literature [21],[23]. For the L3 gas the dependence of V_x on the N_2 concentration has been measured in detail (see section 3.2). If a small fraction of electro-negative gas such as water or O_2 is added to the drift gas mixture, a part of the drift electrons is captured and will not contribute to the finally detected signal. If λ_c is the mean free path for electron capture, then, starting with n_o drift electrons, the number of electrons as function of the drift distance decays exponentially as $n_x = n_o e^{-x/\lambda_c}$. The effect of small amounts of electronegative gas can be quite large [21]. Water is added deliberately because of its positive influence on aging of the chambers. No measurements were done to check the dependence of the drift velocity on the water concentration; measurements performed in different gas mixtures [24] suggest possible effects which should be accounted for. It is planned to measure these effects on the drift velocity in the L3 gas mixture with a seperate testbeam experiment at CERN.

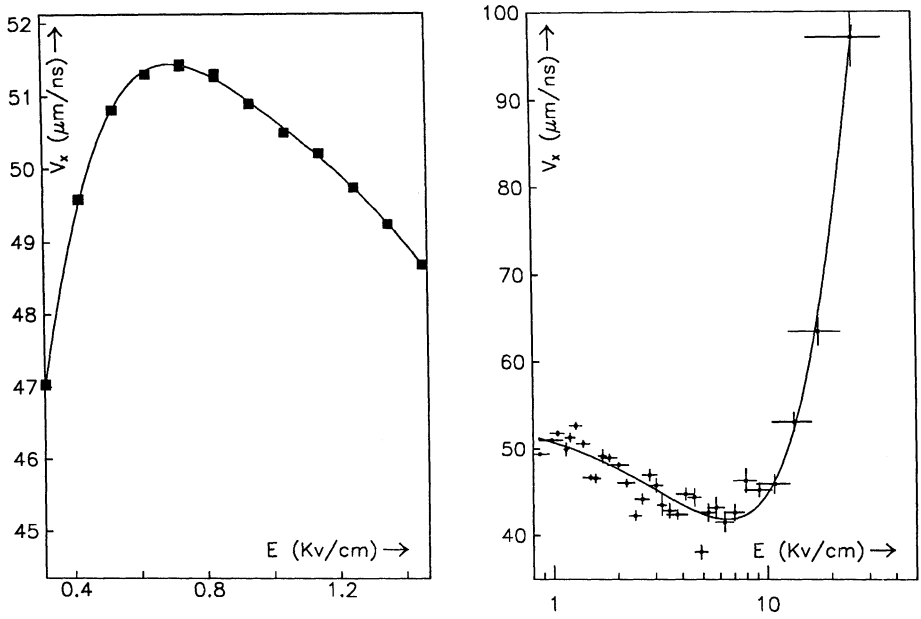

Figure 1.8: Drift velocity V_x as function of electric field (a). In figure (b) the value of V_x at very high electric fields is shown.

1.5.1 Gas amplification.

The electrons drifting towards the sense wires enter a region of very high electric fields just around the sense wires; here the electrons can receive enough energy between the collisions to excite and ionize a gas molecule at collision. The primary electron, and the newly created electron, continue the drift process towards the sense wire, and the process repeats itself which results in an "avalanche". The final number of electrons can be $10^4 - 10^5$, and result in a detectable signal at the end of the sense wire.

1.6 Reconstruction of muons in L3

The first step in the reconstruction of muons in L3 is the reconstruction of track segments in individual chambers. If sufficient data are found in three neighbouring cells of a p-chamber, a pattern finder collects all the TDC data that might be part of the same track segment and a fit procedure is started. However, only part of the corrections can be applied to the data at this stage. For instance, time of flight corrections can only be applied after the z-position of the track segment has been determined after a search

for z-segments in the z-chambers. Each muon that crosses the detector will result in both p-segments in the p-chambers and z-segments in the z-chambers. Since there is no provision to determine on which side of a sense plane the particle passed in the p-chambers, data found in one cell can usually be fitted to two line segments. In this case both line segments are stored. If the track passes through more than one cell, e.g. if the particle crossed a mesh plane, this ambiguity can be resolved directly.

After repeating this procedure in all the muon chambers of an octant, the p-chamber segments are matched to form, projected on the rϕ-plane, complete muon tracks traversing the three layers. At this stage most of the unambiguities can be resolved. The tracks found in the p-chambers and in the z-chambers are combined, and the data are corrected for the time of flight. Once the complete track has been reconstructed the particle's momentum and energy in the muon spectrometer can be deduced. However, for physics analysis these quantities at the interaction point are needed, which will be different from the one found in the spectrometer due to multiple scattering and energy loss in the inner detector. The particle is tracked back through the hadron calorimeter to the outer wall of the TEC using the L3 simulation package SIGEL3, and the best approximation for the average energy loss for this specific track is calculated. Then the TEC data are analyzed. All the track segments in the TEC are reconstructed, among which should be the segment corresponding to the muon. The track vector of the muon at the TEC outer wall is matched with tracks reconstructed in the TEC to find the correct muon segment in this subdetector. Combining all this information, the best track parameters at the interaction point can be calculated, which are stored for physics analysis.

Chapter 2

The L3 magnetic fieldmap

2.1 Introduction

Magnetic fields play a major role in almost all particle detectors; momenta of charged particles can be determined from the radius of curvature of the track and, if the direction of flight is known, the sign of the charge of the particles follows from the direction of deflection. In the L3 detector the TEC measures the charge and momenta of all charged particles, while the muon detector does the same, but for muons only.

For practical reasons the magnetic field as function of the position in space is represented by a "fieldmap". This fieldmap should be able to describe the different components of the actual magnetic field strength at a given point in the detector with the desired accuracy.

This chapter is organized as follows. In the first section the effect of errors in the magnetic fieldmap on the reconstructed muon momentum is discussed and upper limits for ΔB are derived. In section 2.2 the procedures used to construct the L3 fieldmap are explained in detail. The results from magnetostatic simulation programs are presented in section 2.3. The results of these calculations were used to decide on the magnetic sensor distribution presented in section 2.4. Two alternative methods for reconstructing the fieldmap from the probe readings are discussed in section 2.5. Some concluding remarks concerning the magnetic field are made at the end of the chapter.

2.1.1 Effects of errors in the fieldmap

Errors $\Delta\mathbf{B}$ in the fieldmap used in the analysis programs contribute to the error in the muon momentum in three different ways:

1) The first contribution comes from errors in the calculated track curvature; the transverse momentum p_t is calculated from the measured sagitta and the magnetic field value according to:

$$p_t = \frac{0.3 \cdot BL^2}{8 \cdot s} \tag{2.1}$$

$\frac{\Delta p}{p} \propto \frac{\Delta B}{B}$

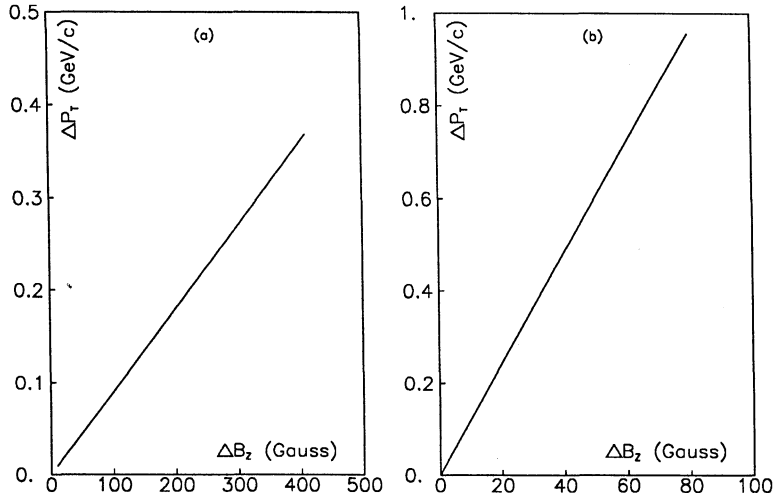

Figure 2.1: Error Δp_t as result from an error ΔB_z in the magnetic field: (a) for fixed measured track positions (assuming $B_z = 0.5T$), and (b) including the change in measured track positions due to changes in the drift angle, at $B_z = 0.5$ T and $x = 25$ mm.

For $B_z = 0.5\,\mathrm{T}$, the sagitta s is 3.7 mm for a 45 GeV/c muon (L=3 meter). For fixed sagitta an error of ΔB_z Gauss in the magnetic field will result in an error Δp_t in the reconstructed momentum of

$$\Delta p_t = 0.96.10^{-3} \Delta B_z$$

This error is shown in figure 2.1(a).

2) The second contribution to the error in the muon momentum is a consequence of the drift properties of the muon chambers. The muon chamber configuration is such that all the wires are aligned parallel to the z-axis, and thus parallel to the main component of the magnetic field. Primary electrons created by a crossing muon will start to drift towards the sense wires in a plane perpendicular to B_z. Due to the Lorentz force they will drift along a path with a Lorentz angle α with respect to the electric field (see figure 2.2). This angle depends on the magnetic field and on all the parameters that the drift velocity depends on. Ignoring variations in the drift velocity due to variations in B_z, the dependence of α on the magnetic field can be written as

$$\tan \alpha = k.B_z \tag{2.2}$$

where k is a constant. For the normal voltages of the L3 muon chambers and a magnetic field of 0.51 T, the drift velocity $V \approx 50 \mu$m/ns and the drift angle $\alpha \approx 19^o$, corresponding to a value of $k = 0.675$.

For a fixed drift drift velocity $V = |\mathbf{V}|$ and fixed measured drift time T the change in the measured x coordinate of the track due to a change in the drift angle α is given by

$$\Delta x = VT\Delta\cos(\alpha) = \frac{x}{\cos(\alpha)}\Delta\cos(\alpha) \tag{2.3}$$

Substitution of 2.2 in 2.3 gives:

$$\Delta x = -\frac{k}{2}x\sin(2\alpha)\Delta B \tag{2.4}$$

The reconstructed muon track will shift towards the sense plane (if $\Delta B > 0$ as in figure 2.2), or away from it (if $\Delta B < 0$). The error Δx as function of ΔB is plotted in figure 2.1(b).

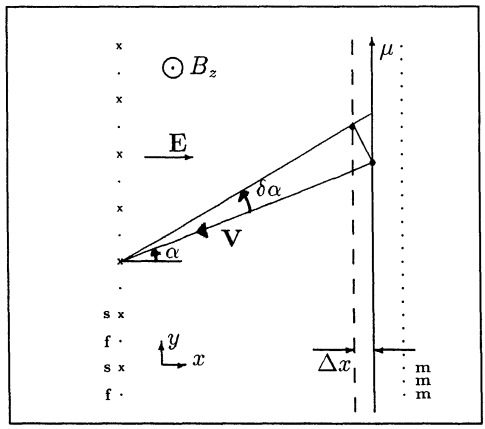

Figure 2.2: Error Δx in the reconstructed track position in a muon chamber due to an error in the drift angle α caused by an error in B_z .

The influence of magnetic field errors on the calculated muon momentum due to the resulting change in the drift angle α depends on the topology of the muon track in the three muon chamber layers; if, for instance, the track segments in all the three chambers are on the same side of a sense plane, the error partly cancels: all three track segments shift to the same side so that the measured sagitta is almost not affected. If the track segment is on one side in the MM chamber and on the opposite side of the sense plane in the MI and MO chambers, the effect on the sagitta, and thus on the error in p_t, doubles. In figure 2.1(b) the error Δp_t is presented for this worst possible case.

3) Another small contribution comes from the minor components of the field: if the radial component B_r is fairly large, say a few hundred Gauss, the Lorentz force will not

only deflect the drift electrons in the x direction due to B_z, but also in the z direction due to B_r (B_y in figure 2.2). The effect can be estimated using relation 2.4, α now denoting the (small) angle between the drift path and the x-y plane. Since the error is proportional to $\sin\alpha$ this effect is smaller than the effect due to B_z. In figure 2.3 is shown that an error of 200 Gauss in B_r gives the same contribution to the error Δp_t as an error of ≈ 20 Gauss in B_z.

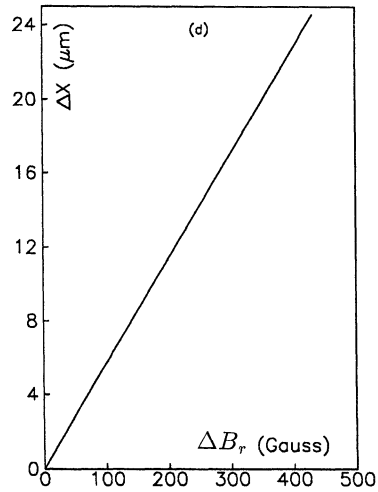

Figure 2.3: Error Δx in the reconstructed drift distance in the muon chambers caused by an error in B_r, one of the minor components of the magnetic field. A drift distance $x = 25$mm and a magnetic field of 0.5 T is assumed.

2.1.2 Accuracy requirements for the fieldmap

In order to keep the total systematic error Δx_{sys} of the track position measurement in the muon chambers below the measurement errors, the upper limit of any individual systematic error contribution was set such that its contribution to Δx_{sys} is at most 10 μm (see section1.3). For the fieldmap this implies that ΔB_z and ΔB_r should be less than 20 and 200 Gauss respectively inside the fiducial volume of the muon chambers. Outside the muon chambers only the error in the sagitta (the first error mentioned in the previous section) will be important. If the maximum contribution of ΔB_z outside the muon chambers on the error Δp_t is chosen to equal the contribution of an error $\Delta B_z = 20$ Gauss inside a chamber (curve (b) in figure 2.1), then an error ΔB_z of ≈ 200 Gauss can be tolerated in the region between the chambers[1]. The B_φ component does not affect the

[1]Note however, that this error does not depend on the track topology. The resulting error Δp_t has to be added linearly to the other error contributions.

drift properties inside the muon chambers because the drift of the electrons is mainly in the φ (or x) direction.

2.2 Discussion of methods

The amount of effort that goes into the construction of a fieldmap depends on the required accuracy; one could, for instance, measure the field at the center of the detector (roughly 5100 Gauss), and use that constant value as the fieldmap for the whole detector. In that case the deviations of the field from the fieldmap will be in the order of $\approx$ 100 to $\approx$ 150 Gauss in the MI and MM chambers, and up to $\approx$ 600 Gauss in the MO chambers. This solution is obviously simple to realize, but too inaccurate for our purpose.

A better solution is to switch on the magnet before any detector components are mounted, and to measure the field at a large number of points. Some interpolation scheme can then be used to calculate the field at an arbitrary point. For this method to be acceptable one has to assume that the field can be remeasured at regular intervals or does not change significantly over a long period of time. However, as shown in the previous section, the demands on the fieldmap accuracy are quite high; it is not reasonable to assume that one can make a fieldmap, once and for all, which will stay within the error limits over a period of several years. Changes in the fieldmap may be expected as a result of varying, or even reversing, the current in the coil. Due to hysteresis effects upon the magnetic materials the past history of the current will also affect the coercive field. Remeasuring the field throughout the volume of the chambers is out of the question because of inaccessibility.

Therefore it was decided to mount magnetic field sensitive probes on the muon chamber surfaces, and monitor the magnetic field during the data taking runs. The total collection of magnetic sensors is called the probe distribution. The type of probes used in L3 to do the measurements for the fieldmap, and the probe distribution in the L3 detector are discussed in section 2.4. Each of the 992 mounted probes will measure the field with a maximum error of 20 Gauss.

Once the probes are mounted, one needs a computer program to calculate the complete fieldmap. This program will have the magnetic field values as read by the probes and the probe positions as input and should be able to calculate the field anywhere within the detector volume with the desired accuracy. Programs of this type are called magnetic field reconstruction programs. The different reconstruction programs tried for L3 are described in sections 2.5.

The magnetic field sensors have to be constructed and mounted on the detector surfaces long before the muon chambers are positioned inside the magnet. Once the detector is operational, it is very difficult to open the detector and to change something in the probe distribution. It is therefore necessary to know beforehand how many field

probes are needed and how they are to be distributed in space. If there are not enough probes, or if the probes are in the wrong positions, the reconstruction program may not be able to produce a satisfactory fieldmap.

One might try to guess the total number of probes on the basis of past experience with other large magnets. These estimates vary from person to person: for the number of magnetic probes needed in L3, numbers between 200 and 10000 have been considered. A better approach is to use a computer program, called magnetostatic simulation program, that simulates the real magnetic field of L3. The input for this program is the geometry and magnetic properties of the iron of the L3 magnet and of the aluminum coil, and the current in the coil. The resulting simulated magnetic field distribution can then help to decide on the total number and the position of the magnetic probes. A 2-dimensional magnetostatic simulation program was used to model the field (see also section 2.3). The precise arguments used to decide on the probe positions are discussed in section 2.4.

The field strengths at these selected probe positions (according to the magnetostatic simulation) can then be used as input for the reconstruction program to produce a fieldmap, that can be compared with the original simulated magnetic field at many points to decide whether the fieldmap is accurate enough. If not, more probes can be added, or different probe positions can be selected and the procedure repeated until a satisfactory fieldmap is produced. One can then guarantee that the same probe distribution in the real field, together with the same reconstruction program, will result in a satisfactory fieldmap of the real field. In subsection 2.5.2 the reconstruction method that is most likely to be used in L3 is presented. An alternative method favoured by the author of this thesis is described in subsection 2.5.3. These two methods have been tested, using simulated magnetic field values at the fixed probe positions, approximating the octagon by a cylinder and ignoring any φ dependences. Both reconstruction methods can be extended to 3 dimensions.

2.3 Magnetostatic field simulations

2.3.1 Introduction

A computer model of the field should be able to describe local structures in the field with an accuracy comparable to the accuracy required of the fieldmap. Since the reconstruction algorithm will be some kind of fit procedure through the data supplied by the magnetic probes, the gradients of the field are more important than the absolute value of the field: a fit becomes more complicated if the gradients are large whereas a change in the absolute value will result in a global scale factor which in general does not complicate the fit.

To obtain an exact 3-dimensional (3D) description of the L3 magnetic field is a com-

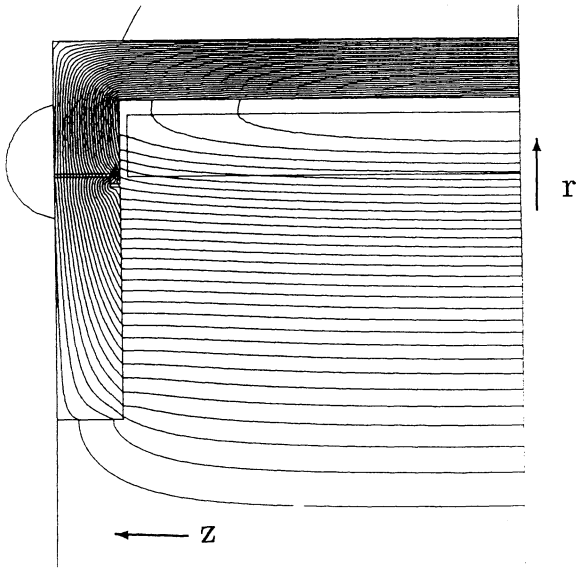

Figure 2.4: Results from 2-dimensional (2D) calculations: field lines in one quarter of the detector [34].

plicated task; not only the model definition is difficult, but also the numerical problems can become very large, in terms of both computer memory and computer time. A 3D problem can be reduced to a 2D one if the magnet is symmetric in one of the coordinates. In the case of L3 the octagonal structure can, to a good approximation be described by a cylinder. The φ variations of the field are ignored and the field is described as a function of r and z only. As will be explained in section 2.4.2 the distribution of magnetic probes on top of the muon chambers that was eventually chosen, was based mainly on 2D results [25]. The 2D model is expected to be in good agreement with the real L3 field in the middle region. Deviations will occur close to the coil, and near the door, where the octagonal shape of the holes and gaps will introduce a φ dependence of the field. The 3D model has been used in a later phase to test the reconstruction programs.

2.3.2 2D model

The program used for the 2D calculations is POISSON [26], available from the CERN program library. For this model the coil and the magnet yoke are considered to have a perfect cylindrical shape. The diameters of the coil and the yoke are chosen equal to the average diameters of the octagonal coil and yoke. The model contains circular holes in the doors with a diameter of 2.53 meter, and a 10 cm gap around the door (fig 2.4). A permeability $\mu(\mathbf{H})$ as shown in table 2.1 was used. The resulting field lines in the r-z plane are shown in figure 2.4. The $\mathbf{B}_z$ component along the top and bottom of the muon

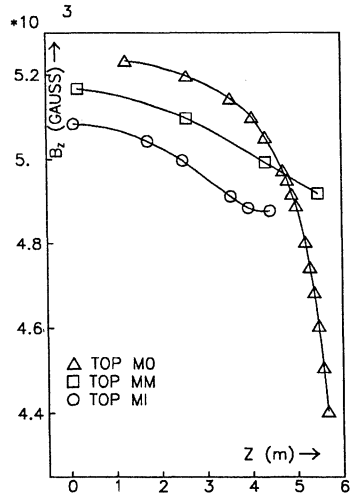

Figure 2.5: B_z on the top of the MO, MM and MI chambers, as calculated by the 2D magnetostatic simulation program POISSON. The positions of the symbols correspond to points where the field will be measured with magnetic sensors.

B[T]	**H**[A/m]	**B**[T]	**H**[A/m]
0.0	0.0	1.6	4000.
0.5	80.	1.7	8000.
1.0	400.	1.8	16000.
1.2	800.	1.9	32000.
1.4	1600.	1.95	64000.
1.5	2400.		

Table 2.1: B-H relation used in the 2D magnetic field calculations

chambers is shown in figure 2.5. From this figure it follows that the field is reasonably smooth and homogeneous except for large z values near the MO and MI chambers, due to the gap around the doors and the large central hole in the doors respectively.

2.3.3 3D model.

To include the octagonal structure of the L3 magnet in the calculation, one needs a 3D model of the geometry, which will result in a 3D model of the field. To construct a 3D model of the magnetic field one can either solve the Maxwell integral equations, with the advantage that the problem definition is simple but with complex related integrals to be solved, or one can solve the Maxwell differential equations with some finite elements

method, which implies a complex problem definition but solvable numerical equations. A good compromise is formed by the two scalar potential method [27] outlined in this section.

The basic equations for non-linear magnetostatics are:

$$\begin{aligned} \nabla \cdot \mathbf{B} &= 0 \\ \nabla \times \mathbf{H} &= \mathbf{J} \end{aligned} \tag{2.5}$$

where $\mathbf{B}$ is the magnetic inductance and $\mathbf{H}$ the field intensity. The current density $\mathbf{J}$ is assumed to be a known function. The general relation between $\mathbf{B}$ and $\mathbf{H}$ is:

$$\mathbf{B} = \mu(\mathbf{H})\mathbf{H} \tag{2.6}$$

where $\mu(\mathbf{H})$ is the material permeability tensor. If one has a current-free region Ω_f then $\nabla \times \mathbf{H} = 0$ in that region, implying that the total field in that region can be described by the gradient of a "total magnetic scalar potential" ψ :

$$\mathbf{H}_f = -\nabla\psi \tag{2.7}$$

In a region Ω_c that contains all the currents defined in the problem but no magnetic materials, $\mathbf{H}$ can be separated in two parts:

$$\mathbf{H}_c = \mathbf{H}_m + \mathbf{H}_s \tag{2.8}$$

where $\mathbf{H}_s$ is the field produced by the currents in this volume and $\mathbf{H}_m$ the remainder of the field for which we have again $\nabla \times \mathbf{H}_m = 0$. This component can therefore be represented by a "reduced magnetic scalar potential" ϕ

$$\mathbf{H}_m = -\nabla\phi \tag{2.9}$$

and $\mathbf{H}_s$ can be calculated from the integral:

$$\mathbf{H}_s = \frac{1}{4\pi} \int_{\Omega_c} \mathbf{J} \times \nabla \left(\frac{1}{R}\right) d\Omega \tag{2.10}$$

where R is the distance from the source to the point where $\mathbf{H}_s$ is evaluated.

After substitution of $\mathbf{H}_f$, $\mathbf{H}_m$ and $\mathbf{H}_s$ into equation 2.6, the divergence $\nabla \cdot \mathbf{B} = 0$ can be written as:

$$\begin{aligned} -\nabla \cdot \mu\nabla\phi + \nabla \cdot \mu\mathbf{H}_s &= 0 \quad \text{in } \Omega_c \\ -\nabla \cdot \mu\nabla\psi &= 0 \quad \text{in } \Omega_f \end{aligned} \tag{2.11}$$

At the interface between the regions Ω_c and Ω_f, the normal component of the magnetic induction $\mathbf{B}$ and the tangential components of the field intensity $\mathbf{H}$ must be continuous. If $\hat{n}$ is the outward normal from Ω_f and $\hat{t}$ a tangent unit vector to the surface then:

$$\begin{aligned} \mathbf{B}_f.\hat{n} &= \mathbf{B}_c.\hat{n} \\ \mathbf{H}_f.\hat{t} &= \mathbf{H}_c.\hat{t} \end{aligned} \tag{2.12}$$

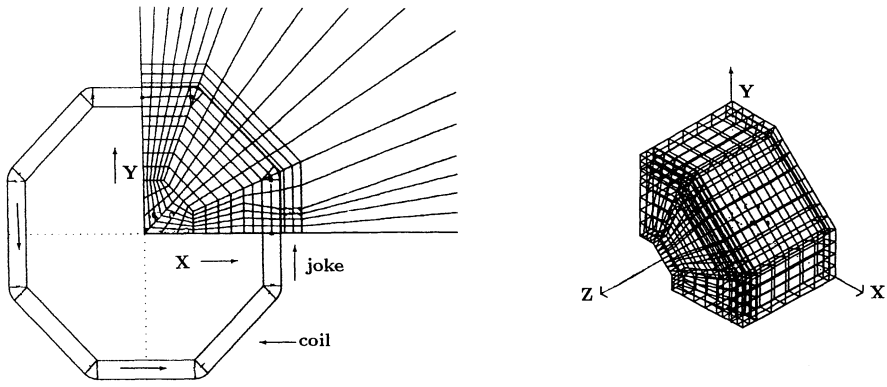

Figure 2.6: Finite element grid used by TOSCA. The grid is chosen such that the holes in the yoke and the gap in the door can easily be taken into account.

at the interface. At the outer boundary of Ω the Neumann boundary conditions were used: [2]

$$\begin{aligned} \mathbf{B}_f \cdot \hat{n}_\Omega = 0, \mathbf{B}_c \cdot \hat{n}_\Omega = 0 \\ \mathbf{H}_f \cdot \hat{n}_\Omega = 0, \mathbf{H}_c \cdot \hat{n}_\Omega = 0 \end{aligned} \tag{2.13}$$

The vector $\hat{n}_\Omega$ is the outward vector normal to the boundary of Ω. The program package TOSCA can solve magnetostatic problems with the above problem definition, and has been shown to be able to produce accurate results, also for complicated geometries [27]. Equations 2.11 are solved with a finite element method. The complete coil is described by rectangular current blocks and circular corner blocks (fig 2.6). The current density in these blocks is taken to be equal to the current density in the L3 coil at 30 kA. The volumes inside and around the magnet are described on a suitable grid. First a 2-dimensional grid is defined in the x-y plane. The holes in the doors are included in the model. Through the points defined in this grid one draws lines parallel to the z-axis. The 3-dimensional finite element blocks are defined by a set of planes perpendicular to the z-axis. Each of the resulting prisma shaped blocks is "filled" with the proper material like "air"(with $\mu = 1$), or "iron"(with a permeability μ defined in table 2.2). These planes are again chosen such that the detector structures can be modeled correctly. As an example, one needs a plane at both sides of the door in order to define the door by

[2] An alternative condition is to set the fields equal to 0 on the outer boundary. As long as the outer boundary is situated far enough from the region of interest (inside L3), the particular choice for the outer boundary condition does not affect the solution significantly.

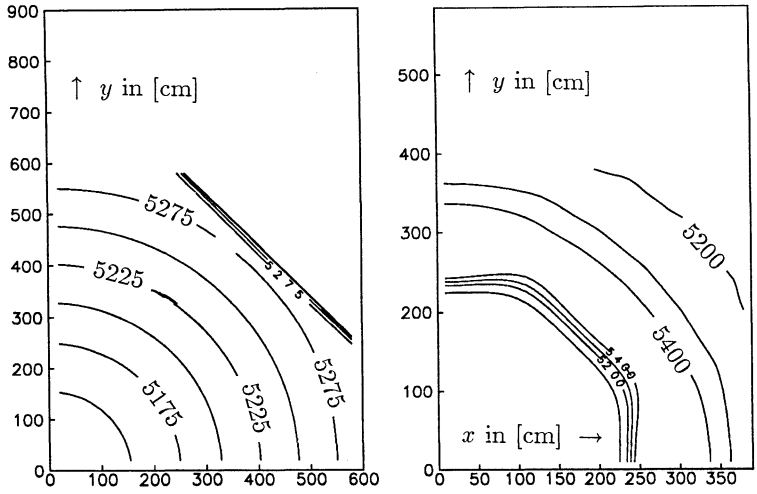

Figure 2.7: Contours of constant B_z as calculated by the program TOSCA for z=0 m (a) and z=5.50 m. (b).

filling the proper blocks with "iron". More planes can be chosen at arbitrary z-values to reduce the block sizes. Figure 2.6 illustrates the grid. In (a) the 2-dimensional grid in the x-y plane which extends up to 40 meters outwards in x, y and z is shown and in (b) the 3-dimensional grid.

To minimize the problem, the total grid is kept as small as possible by introducing additional symmetries. First the detector is assumed to be symmetric with respect to the central (z=0) plane. The solution is chosen to be perpendicular to this plane, thus $\mathbf{B} \cdot \hat{t} = 0$ for any point of the plane z=0. Furthermore the solution is assumed to be symmetric in the planes x=0 and y=0. On these planes Neumann boundary conditions are assumed: $\mathbf{B} \cdot \hat{n} = 0$ with $\hat{n}$ the normal vector to these planes. The total grid therefore describes only 1/8 of the total volume Ω.

2.3.4 TOSCA results

The B_z component of the magnetic field as function of x and y at z=0 and at z=5.5 meter is presented in figure 2.7. It shows that the field is everywhere almost cylindrical symmetric, except near the holes in the door and close to the coil. The variation of B_z on top of the three muon chambers is shown in figure 2.8. Values are given for z=0.0 meter and z=5.5 meter. On top of the MO chamber the variations are smallest: close to the coil the equal-B_z contours are parallel to the coil. This simplifies the measurement of B_z on the MO chambers.

B[T]	H[A/m]	B[T]	H[A/m]
0.012	18.2	0.949	490
0.032	39.5	1.08	660.
0.039	44.7	1.29	1193
0.101	81.7	1.38	1618
0.353	149	1.58	3963
0.664	270.	1.76	9706

Table 2.2: B-H relation used by TOSCA, as measured with a steel sample (sample 2, 21/05/85)

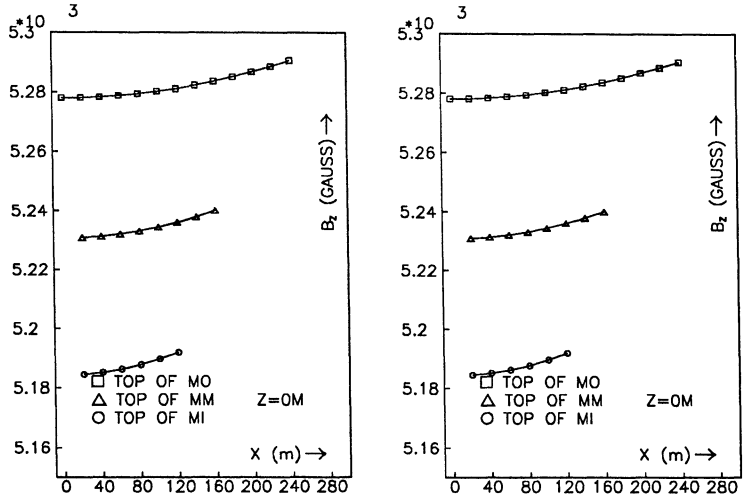

Figure 2.8: Variation of B_z vs x on top of the muon chambers at z=0.0m (a) and z=5.5m (b). The middle of the octant is at x=0.

2.4 Probes and probe distribution

2.4.1 Magneto resistors

Cheap magneto resistors (FP30N60K from Siemens) were chosen for the construction of the magnetic field probes. Magneto resistors (MR) are field dependent resistors based on the Hall effect. The current carriers in the semiconductor material (InSb/NiSb) are deflected by a transversal magnetic field. Needles of low resistance NiSb crystals oriented perpendicular to the current direction in the InSb base plate compensate the deflection of the current carriers. This will increase the path length, and thus the total resistance over the MR, independent of the sign of the field.

The resistance of MRs is mainly dependent on the field component normal to the probe surface with small corrections for the components parallel to this surface. If R is the resistance, then $R = R(\tilde{B})$ where:

$$\tilde{B} = \sqrt{B_\perp^2 + \alpha_i^2 B_i^2 + \alpha_j^2 B_j^2} \tag{2.14}$$

The $\perp$ direction is the direction perpendicular to the MR plate, and the i,j directions are parallel to the plate. The constants $\alpha_i \approx 0.2$ and $\alpha_j \approx 0.1$ are experimentally determined [33]. The probes are aligned such that the $\perp, i, j$ directions correspond to the z, φ and r directions of the main L3 coordinate system. From the field simulations $B_r/B_z \leq 20\%$ and $B_\varphi/B_z \leq 10\%$, resulting in:

$$\frac{\tilde{B}}{B_z} = \sqrt{1 + \alpha_i^2 \left(\frac{B_\varphi}{B_z}\right)^2 + \alpha_j^2 \left(\frac{B_r}{B_z}\right)^2} \leq 1.0004 \tag{2.15}$$

This shows that the influence of the minor components on the measurement of B_z can be neglected. The alignment of the magneto resistors is critical; to obtain probe readings with errors below 0.3%, the alignment should be better than 77 mrad (if $B_r = 0$). If the minor components are large the alignment error should be even smaller (e.g. for $B_r = 500$ Gauss the alignment should be better than 35 mrad).

2.4.2 Probe distribution

The results of the 2D calculations led to the probe distribution which will eventually be used to reconstruct the fieldmap [32]. In section 2.1 it was shown that the map needs to be most accurate inside the fiducial volume of the muon chambers. The best place to mount probes is therefore on the top and on the bottom surfaces of these chambers. The probe distribution finally chosen is shown in figure 2.9. The decision to use this particular probe distribution was based upon the following arguments:

1) The distance between the probes on one chamber surface has been chosen such that the field variation between 2 neighbouring probes is ≤ 0.04 T. This requires 16 probes on the MO, 4 on the MM and 6 on the MI chambers [25] for each row in the z-direction. (see also figure 2.5)

2) From the 2D calculations the variations in the x-direction at fixed z on top of a chamber can be estimated: $\Delta B_z < 50$ Gauss on all the chambers and for all values of z. The variations in the φ-direction over one chamber are small enough to use only 2 measurements in φ. Close to the door on top of MO the 2D model is least reliable because of the presence of the gap around the doors that was not accurately represented in the model. Additional probes were therefore mounted on top of MO to map the field in these corners close to the door. This is in agreement with the 3 dimensional results presented in figure 2.8.

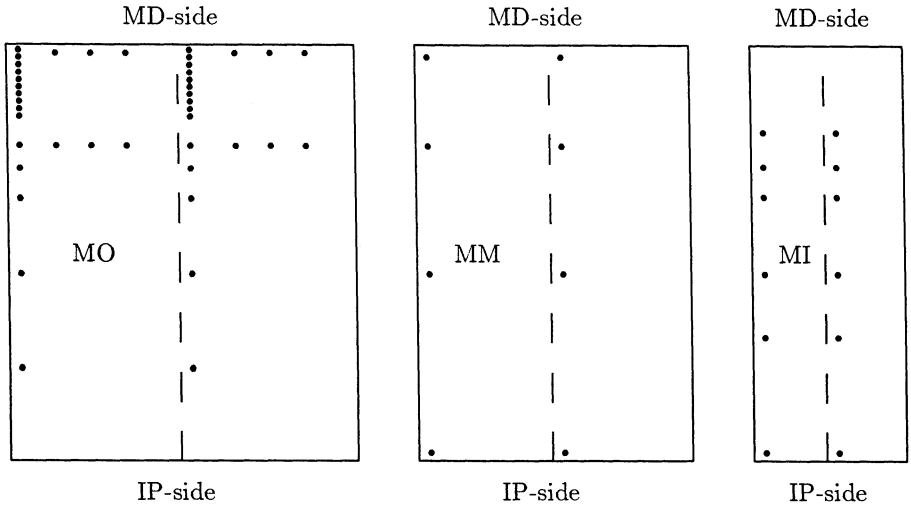

Figure 2.9: Distribution of the MR probess on the top of the 3 muon chamber layers. Most of the probes are mounted on the MO chambers where the field irregularities are biggest.

In total 992 magneto resistors (MR) probes have been mounted on the top of all the muon chambers. Figure 2.9 shows the probe distribution on the top surfaces of the 3 muon chamber layers in one octant. The probes are divided in two rows in the z-direction, one in the middle and one at one side of the octant.

2.5 Magnetic field reconstruction

2.5.1 Introduction.

In this section the various methods are discussed which are available for deriving the magnetic fieldmap from the field measurements supplied by the MR-probes. Three methods are considered here:

1) One has tried a direct 3D interpolation with polynomials or splines without using any additional properties of the magnetic field. This method has been ruled out, because

the solutions tend to behave unphysically and because one has no check on the accuracy achieved [28]. There is also no analytical way to derive the minor components from the solution.

2) In the second method the general form of the solution of the field equations is taken into account. Only solutions of the equation $\Delta B_z = 0$ are considered and a least squares fit is made to the field values measured by the probes [29]. The function fitted is a truncated solution of the Laplace equation in a simplified geometry (for the L3 volume a cylinder was used). The number of free parameters is reasonably low. Some details on this method are presented in the next section.

3) The third method, a variation of method two, was developed and successfully tested by H.Wind for simply shaped volumes like rectangular boxes and cylinders [30][31]. Only field input data on the boundary of the given volume are used in this method. The resulting boundary value problem is solved by fitting an expansion of orthogonal functions, which are solutions of the Laplace equation, to the field measurements. Results from tests of this method on the 2D simulated field are discussed in section 2.5.3

2.5.2 The least squares fit method

The volume of the L3 detector can be approximated reasonably well by a cylinder. The amount of magnetic material inside this volume is very small and can safely be ignored. Since the volume is current free, $\nabla \times \mathbf{B} = 0$ and thus

$$\mathbf{B} = -\nabla\psi$$

Also:

$$\nabla(\nabla \cdot \mathbf{B}) = \Delta\mathbf{B} = 0 \tag{2.16}$$

Expressed in cylindrical coordinates, this results in $\Delta B_z = 0$, and two coupled differential equations for the other components B_r and B_φ. From now on only component B_z will be considered.

A function B_z obeying the condition $\Delta B_z = 0$ is fitted to the data points from the magnetic probes and/or to interpolated points, which result from a one-dimensional fit through subsets of these magnetic probe points. Only a fit in 2 dimensions was done, selecting a subset of all the probes which lay in one r-z plane. The function considered is a truncated orthogonal function expansion in cylindrical coordinates:

$$B_z = B_o + \sum_i A_i J_i(p_i r)\left(e^{p_i z} + e^{-p_i z}\right) + \sum_{k=\text{odd}} B_k I_k(\mu_k r) cos(\mu_k z) \tag{2.17}$$

The method can easily be extended to 3 dimensions by including some adequate φ terms.

The unknown constants A_i and B_k are determined by a least squares fit of this function to the probe data. The fitting method works reasonably well, with the largest

errors in the corners of the MO chambers, close to the gap around the door. Using data from a test run of the magnet, and using some data from additional measurements along the doors, the fit errors are ≤ 30 Gauss for the muon chamber region. Some additional probes along the doors were mounted on some of the octants in a later phase in order to supply the additional measurement needed in that region. The number of unknowns A_i,B_k can be varied to find the optimum, and the function can be extended to three dimensions, by adding the φ dependence of the field.

2.5.3 Boundary value method

H.Wind showed [30][31] that it is possible to construct a fieldmap for all three components of the field by measuring one of the components on the boundary surface of the volume of interest. From measurements $B_{z,i}$ on the cylindrical boundary one has to solve:

$$\begin{array}{lll} \Delta B_z & = 0 & \text{inside cylinder} \\ B_z & = B_{z,i} & i = 1, ..., N \end{array} \tag{2.18}$$

The solution B_z is approximated by the truncated orthogonal function expansion for the solution of the Laplace equation in cylindrical coordinates. Since the Δ operator is linear, the problem can be subdivided into sub-problems with simpler boundary conditions. For the first sub-problem one assumes $B_z \neq 0$ on the end plates of the cylinder and $B_z = 0$ on the cylindrical surface. This problem has solutions of the form:

$$\begin{array}{lll} B_z^a & = & \sum_{m,k} \alpha_{m,k}^{odd} \sin(\lambda_m \varphi) \sinh(\mu_k z) J_m(\mu_k r) \\ B_z^b & = & \sum_{m,k} \alpha_{m,k}^{even} \cos(\lambda_m \varphi) \cosh(\mu_k z) J_m(\mu_k r) \end{array} \tag{2.19}$$

For the second sub-problem one assumes $B_z = 0$ on the end plates and $B_z \neq 0$ on the cylindrical surface. This results in solutions of the form:

$$\begin{array}{lll} B_z^c & = & \sum_{m,k} \beta_{m,k}^{odd} \sin(\lambda_m \varphi) \sin(\mu_k z) I_m(\mu_k r) \\ B_z^d & = & \sum_{m,k} \beta_{m,k}^{even} \cos(\lambda_m \varphi) \cos(\mu_k z) I_m(\mu_k r) \end{array} \tag{2.20}$$

where J_m and I_m are the ordinary and modified Bessel functions of integer order. The coefficients $\alpha_{m,k}^{odd,even}$ and $\beta_{m,k}^{odd,even}$ are fitted separately to the odd and even parts of the given boundary condition. The final solution is a linear combination of the above derived solutions and is written as:

$$\tilde{B}_z = B_z^a + B_z^b + B_z^c + B_z^d \tag{2.21}$$

This calculated $\tilde{B}_z$ is the fieldmap for B_z. The magnetic scalar potential ψ can be expressed in $\tilde{B}_z$ in the following way:

$$\psi(r, \varphi, z) = h(r, \varphi) - \int_o^z \tilde{B}_z(r, \varphi, \zeta) d\zeta \tag{2.22}$$

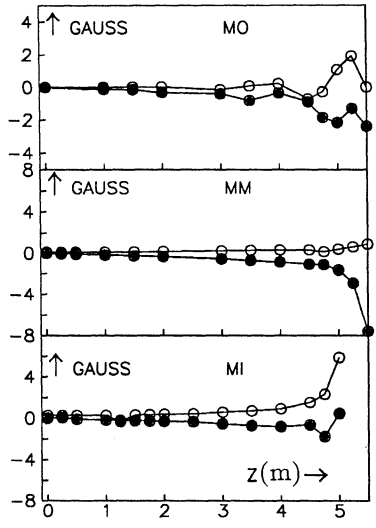

Figure 2.10: Differences in the fieldmap calculated by the method of this section and the original values calculated by POISSON. The errors are shown for B_z (open circles) and B_r (closed circles), at the top of the MO, MM and MI chambers.

where $h(r,\varphi)$ is a z-independent function. This function h is the only part of ψ that can not be obtained from measurements of B_z alone. The other components are found by differentiation of the above found ψ:

$$\begin{aligned} B_r &= \partial\psi/\partial r \\ B_\varphi &= \tfrac{1}{r}\partial\psi/\partial\varphi \end{aligned} \tag{2.23}$$

It can be shown that the contribution of h can be neglected for magnetic fields that are (almost) symmetric with respect to the plane $z = 0$. If one sets $z = 0$, equation 2.22 reduces to $\psi(r,\varphi,0) = h(r,\varphi)$. If the field is perfectly symmetric in this plane, then $B_r = 0$ and $B_\varphi = 0$ on this plane. As a consequence $h(r,\varphi)$ will be constant and does not contribute to the field. If the field is almost symmetric in this plane, as is the case in L3, then there will be a number M such that $B_r < M$ and $B_\varphi < M$ on this plane. This means that the gradients of $h(r,\phi) < M$, and therefore the contribution of $h(r,\varphi)$ to the field anywhere inside the cylinder is limited by M. The number M is determined by small asymmetries in the L3 geometry and by the (possible) misalignment of the magnetic z-axis with the detector z-axis.

The model described above has been tested with the 2D POISSON simulation pre-

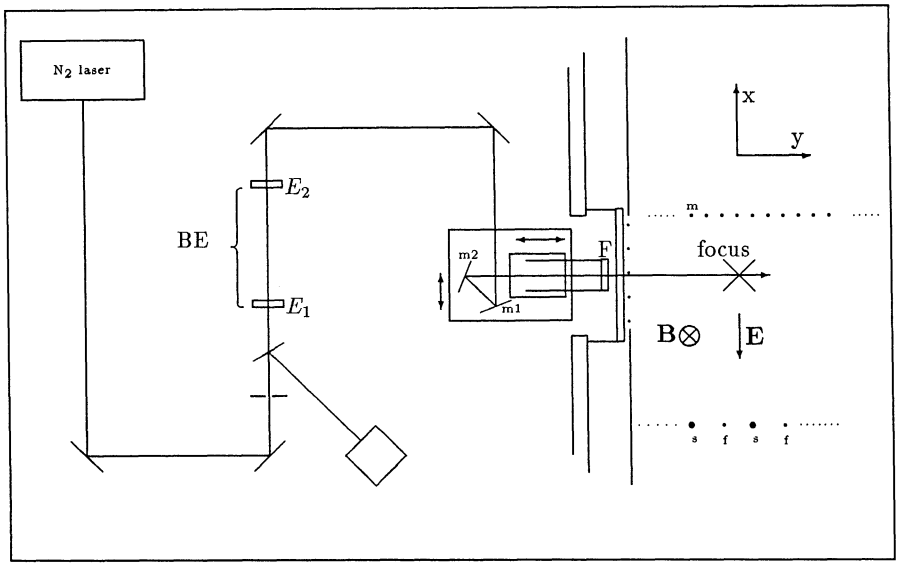

Figure 3.1: Schematic view of the setup in the magnet, as used to measure the drift velocity with the laser.

sense wires passed through hybrid preamplifiers, ECL discriminators and after converting from ECL to NIM signals, into a LeCroy 4208 time-digitizer (TDC) with a resolution of 1 ns. A 5 mm thick BK7 glass window was mounted on the chamber, as close as possible to the wire planes. The mirrors M_1, M_2 were mounted on an anti-magnetic sledge, and the focusing lens on a second sledge perpendicular to, and on top of, the first one. The sledges were moved by remotely controlled motors placed outside the magnetic field and allowed a precision positioning of the focal point in a region of $\approx$ 6 cm by 7 cm in the x-y plane with increments of 1.25 μm in both directions. The movement of the sledges was controlled by the online VAX 750 computer available at the testbeam. The optical focus had a length of 600 μm (in y) and a diameter of $\leq 5\,\mu$m (in x).

The drift time does not only depend on the x position of the focus, but also on the y position. This is caused by the drift path length variations in the cell (see also figure 4.2). The average drift time was measured at two distances from the sense plane, at x=1.5 cm and x=3.5 cm, for a number of values of y. At both distances the laser beam focus was moved over 25 mm in the y direction in steps of 1.25 mm. For each x,y position of the focus, data of 200 laser shots were collected from which the average drift time for both wires was determined. The laser shots were selected using the reference diode response in order to minimize fluctuations in ionization probability. In figure 3.2 the average drift

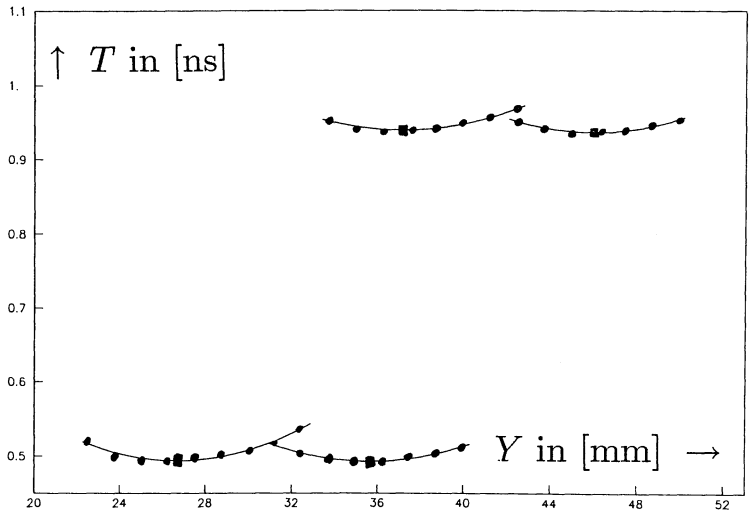

Figure 3.2: Drift time vs. y for the two wires at x=1.5 cm and x=3.5 cm. The curves are parabolic fits to the data points.

time as function of y is plotted, for both wires and for both x-values. The curves in the plot are parabolic fits through the measurements. The drift time and the position of the minimal points were used to calculate the drift velocity and drift angle, which are assumed to be constant between x=1.5 cm and x=3.5 cm.

The drift velocity was measured at 10 different settings of the high voltages as tabulated in table 3.1. The difference between V_{sense} and V_{field} was chosen such that the signal amplitude at the output of the preamplifiers was 300 mV for all the settings. The field strength E corresponding to the high voltage settings was calculated with the program GARFIELD [20].

The results are presented in figure 3.3(a) and (b). Both V_x at B=0 Tesla and V_x at B=0.5 T are shown. The plateau value of the electric field is 0.75 kV/cm at B=0 Tesla, and 1.14 kV/cm at B=0.5 Tesla.

3.3 Longitudinal diffusion (σ_L) measurement

Consider a large sample of tracks at a fixed position in a drift chamber. The variations in the drift time of the electrons depend among other things on the variance of the drift

V_{sense} (Volt)	V_{field} (Volt)	V_{mesh} (Volt)	E ($V.cm^{-1}$)
3240	960	-1920	676
3518	1383	-2240	793
3795	1805	-2560	910
4073	2228	-2880	1030
4350 (L3)	2650	-3200	1140
4628	3073	-3520	1260
4905	3495	-3840	1380
5183	3918	-4160	1500

Table 3.1: Voltage settings and the corresponding electrical field strength in the test chamber used for the drift velocity measurements. The row marked with L3 corresponds to the settings used for the L3 muon chambers.

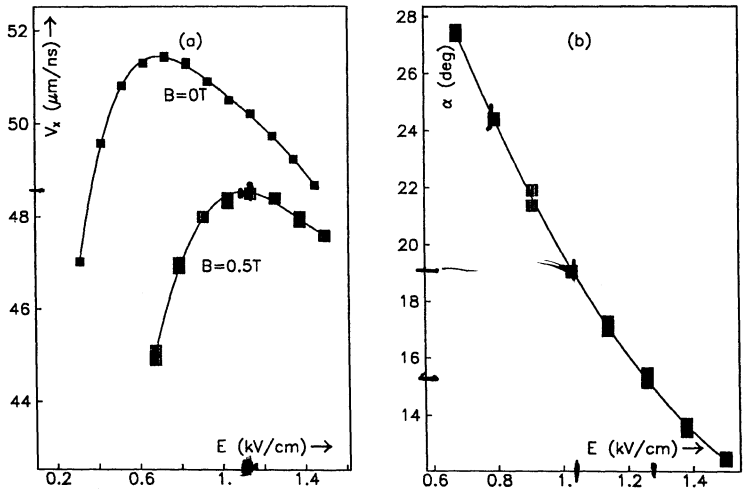

Figure 3.3: Drift velocity and drift angle in the L3 muon chambers at zero magnetic field and at B=0.5 tesla (a), and the drift angle versus the electric field at 0.5 T (b). The curves are polynomial fits to suit the eye.

time of the drift electrons due to longitudinal diffusion. There is no straightforward method to calculate the longitudinal diffusion from this variance of the drift time. One method to measure the longitudinal diffusion accurately is described in this section. A UV laser is used to create single electron events at different distances from the sense wire. According to the idealized solution of the one dimensional transport equation, the

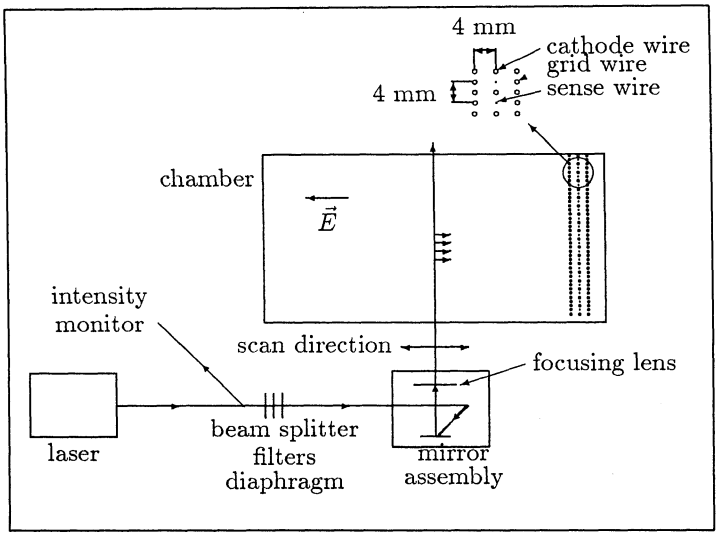

Figure 3.4: Experimental set-up to measure drift velocity and longitudinal diffusion.

distribution of the time of arrival is Gaussian [38]:

$$\frac{\Delta n(x,t)}{\Delta t} \propto \exp -\{(x - V_x t)^2/4D_L t)\} \tag{3.1}$$

where V_x is the drift velocity, D_L the longitudinal diffusion coefficient, and $n(x,t)$ the number of electrons that arrived after a time t from a distance x. The longitudinal dispersion in the drift time distribution σ_L is related to D_L by $\sigma_L = \sqrt{2D_L t}$. If one defines σ_{oL} as the longitudinal diffusion for 1 cm drift length, this becomes $\sigma_L = \sigma_{oL}\sqrt{x}$, which can be calculated directly from the measured time of arrival spectrum:

$$\sigma_{oL} = \frac{\sigma_L}{\sqrt{x}} = \frac{\sigma_t V_x}{\sqrt{x}} \tag{3.2}$$

The units used are [ns] for σ_t, [μm /ns] for V_x and [μm /$\sqrt{\text{cm}}$] for σ_{oL}. If the time of arrival distribution is measured with a cluster of electrons, some complicated corrections on the above distribution are necessary (see for instance [38]). These corrections are necessary to compensate for field inhomogeneities near the wire and drift path length variations. Further corrections are required to compensate contributions to σ_t caused by electronic noise and by the finite laser beam width. If one uses a large collection of single electron events and if one considers the average time of arrival of these single electrons as function of drift distance, these corrections can easily be removed from the problem. The variance in the average time of arrival spectrum σ_t is expressed in terms of σ_L. A

constant contribution σ_o to σ_t, which is assumed to add quadratically, is included:

$$\sigma_t^2 = \frac{\sigma_L^2}{V_x^2} x + \sigma_o^2 \tag{3.3}$$

Here x is the drift distance. The constant σ_o contains the effects of the finite beam width, electronical noise and the fluctuations in the drift time caused by differences in the various possible drift paths. All these effects are independent of the drift distance and can therefore easily be removed from the data.

Different attempts have been made to measure σ_L this way (e.g. [35]), but usually only one drift distance was used. The contribution of σ_o to the measured σ_L had to be estimated in order to derive the correct number for σ_L. One measurement was performed using different distances [36], but only one readout wire was used: at larger drift distances this results in a contribution of σ_t to the measured σ_L. The method described in this section measured the time of arrival spectrum corresponding to a large number of drift distances. This allows a very straightforward determination of σ_L without any complicated corrections.

The setup used to measure the drift velocity and longitudinal diffusion in the L3 drift gas was developed at NIKHEF-H [37]. A schematic view of the setup is shown in figure 3.4. It consists of a drift chamber with a maximum drift distance of 10 cm that could operate with the high gain needed to detect the signal that results from the avalanche induced by one electron arriving at a sense wire. For the production of the drift electrons the UV laser described in the previous section was used, but at very low intensity. Six of the sense wires were read out by hybrid preamplifiers. The signal passed into a second amplifier (LeCroy 612A) with two outputs. One of the outputs was connected to a charge integrating Analog to Digital Converter(ADC, LeCroy 2249W) and the other output to a Time to Digital Converter (TDC, LeCroy 4208, 1 ns resolution).

The laser beam passed a beamwidth adapter that reduced the beamwidth to 2 mm. This narrow beam was focused into the chamber, with the focus in the middle of the drift region covered by the six sense wires. The diffraction limited focus is stretched over several centimeters, which results in an almost constant ionization in all six cells. As a result the event probability for all these sense wires was almost the same, and the data of all the wires could be combined in order to increase the efficiency (after calibration of the ADC and TDC offsets).

The beam intensity was reduced such that the event probability, taking all active wires together, was less than 10%. Under these conditions almost all events are single electron events. This was checked by varying the gas gain: if the event probability is low but the chamber is not operating in single electron mode, the event probability will be very sensitive to the gain, whereas the shape of the ADC spectrum is constant. On the other hand, if the chamber is operating in single electron mode, the ADC spectrum does depend on the gain while the event probability does not. The ionization follows the

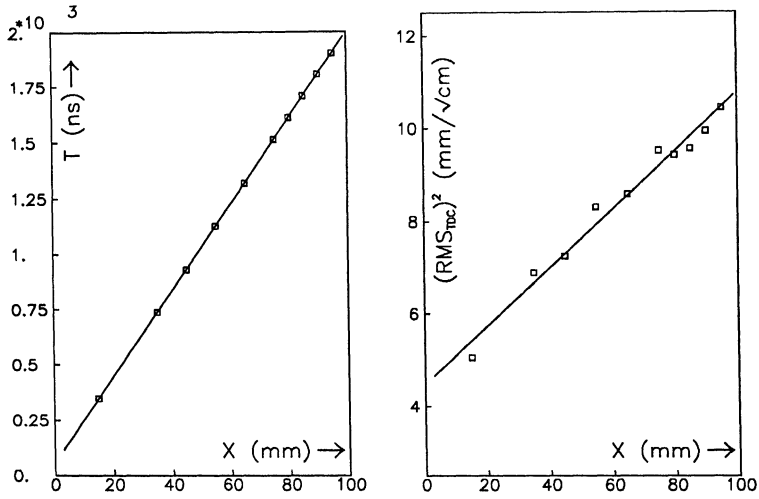

Figure 3.5: Average drift time vs drift distance (a), and average rms of drift time vs drift distance (b). The drift velocity is calculated from the slope of (a), and the longitudinal diffusion from the slope of (b).

Poisson statistics. From this, one can calculate that about 5% of the events are 2-electron events.

For the calculation of σ_L a total of 1,000,000 laser shots were analyzed. The drift time was measured for 10 different drift distances between 15 and 95 mm. The ADC and TDC data were collected and processed by a super CAVIAR. First the laser amplitude was read out. If the amplitude was too far from the nominal value, the event was rejected. Next the TDC and ADC were read out. Events with two neighbouring hits were rejected (possible incorrect timing caused by induction from the neighbouring wire), as well as events with negative data on the ADC (induced crosstalk). The accepted TDC and ADC data were booked in histograms. For each drift distance, data were collected until 1000 good events were found. Such a large number of events is needed to achieve a good accuracy on the width of the TDC spectrum (TDC rms), which varied between 30 ns and 200 ns (3σ). To reduce the background from noise and cosmic rays, a fixed width cut was made in a 30 ns wide window around the TDC bin with the largest number of entries, and all the histograms were refilled. After this refilling the procedure was repeated 4 times, but now for a window width of 6 times the sigma of the distribution of the previously selected TDC data. Typical results are shown in figures 3.5 where the average drift time and the square of the rms of the drift time are plotted as function of drift distance.

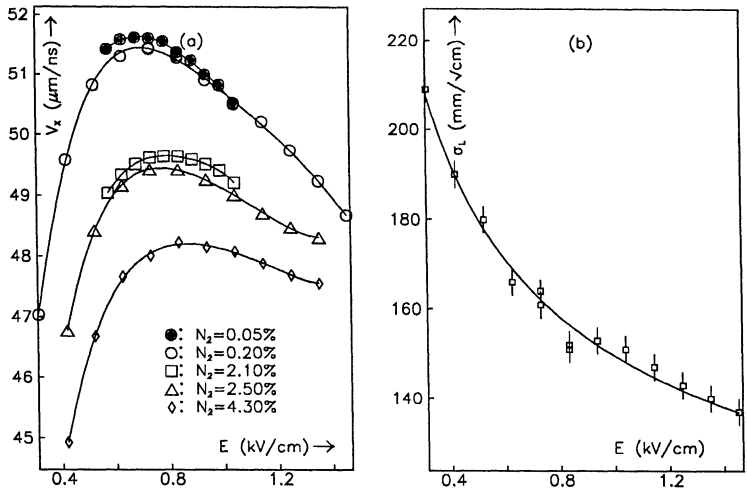

Figure 3.6: Drift velocity as function of electric field for different amounts of N_2 in the muon chamber drift gas (a) and the longitudinal diffusion in the muon chamber driftgas as function of the electric field (b).

The longitudinal diffusion σ_L is calculated from these data by fitting

$$t(x) = \frac{1}{V_x}x + t_o \text{ and } \sigma_t^2 = \frac{\sigma_L^2}{V_x^2}x + \sigma_o^2 \tag{3.4}$$

Here x is the drift distance, $t(x)$ and t_o the average drift time and the zero time constant, σ_t and σ_o the standard deviation of the TDC data and the standard deviation at zero drift distance. The whole procedure was repeated for ten different values of the electric field. The drift velocity as function of the electric field was presented earlier in figure 3.3. The longitudinal diffusion is shown in figure 3.6.(b).

3.3.1 Effect of N_2 in driftgas on V_x

With the L3 muon chamber gas control system the ethane content of the chamber gas mixture can be controlled to within 0.1%. Small fluctuations in the gas composition are caused by contamination of the gas bottles and by small gas leaks in the system. Common contaminations are O_2 and N_2 (air). The oxygen can easily be removed from the gas (during the octant tests the O_2 concentration could be kept below 100 ppm), but N_2 is quite inert and therefore harder to remove. Some N_2 is therefore likely to be present in the gas mixture. A method to remove the N_2 from gas mixtures has been developed by Dijkman[39], but has not been used for the L3 muon chamber gas mixture.

A separate set of measurements was done to measure the dependence of the drift velocity on small N_2 contaminations of the drift gas. For the drift velocity measurements one needs only the average drift time. This can be determined accurately from 50 events per drift distance (compared to 1000 needed for the diffusion measurement). The Argon and Ethane gas flow was regulated with Brooks mass flow controllers, and checked daily with a soap bubble flow meter. The N_2 flow was measured with a soap bubble flow meter only. Measurements were done with gas compositions as tabulated in table 3.2.

run	Argon	Ethane	Nitrogen
1	61.4%	38.4%	0.2%
2	60.2%	37.7%	2.1%
3	60.2%	37.3%	2.5%
4	59.0%	36.7%	4.3%

Table 3.2: Gas composition used for drift velocity vs N_2 measurements.

For each tabulated gas mixture the whole measurement procedure described in the previous section was repeated, but only the fit to V_x was done. A compilation of the results is presented in figure 3.6(a). All the curves are polynomial fits to suit the eye.

3.4 Conclusions

The drift velocity at B= 0.5 T in an Argon : Ethane = 61.5 : 38.5 mixture was measured as a function of the electric field in order to determine the plateau value. From the results it can be concluded that the standard high voltage settings used in the L3 muon chambers are slightly higher than the optimal plateau value found in these measurements, but since the average magnetic field in L3 will be slightly higher than the 0.5 Tesla used in the measurements described in this chapter, the HV values should be considered adequate.

The dependence of the drift velocity on N_2 contaminations has been measured. The change in the drift velocity V_x as function of the N_2 concentration at fixed electric field values is shown in figure 3.7. Although these results were obtained at zero magnetic field, figure 3.7 can be used to estimate the allowable N_2 contamination in the L3 drift gas. Assuming the effect at B=0.5 Tesla to be somewhere in between the two curves drawn in figure 3.7, one finds $|\Delta V_x|/V_x = (1.2 \pm 0.3)[N_2]$, where $[N_2]$ is the N_2 concentration in %.

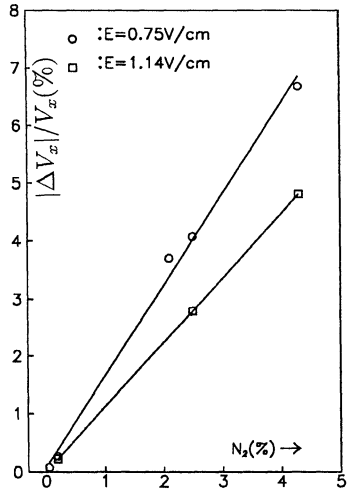

Figure 3.7: Relative change in the drift velocity as function of N_2 concentration in the L3 muon chamber drift gas. Results are shown for two values of the fixed electric field strength and for zero magnetic field.

Chapter 4

Muon chamber testbeam

4.1 Introduction

The purpose of the muon chamber testbeam experiment is to obtain a good description of the behaviour of the L3 muon chambers in a magnetic field under various conditions. From the testbeam measurements a relation between the drift time and the drift distance is determined which is valid for different values of these conditions. This relation is called the "cellmap". Some of these conditions are only partly under control and vary in time or for different parts of the L3 detector. For example, the pressure P varies in time with the outside barometric pressure and the temperature T is different for different parts of the detector. The magnetic field B is constant in time but varies over the different parts of the muon spectrometer, and even over each individual muon chamber. It is very difficult to determine the drift time - drift distance relation accurately with the L3 muon detector using only highly energetic muons or cosmic rays: firstly, a considerable amount of time is required to collect enough events at various points in the muon detector to reduce statistical errors and secondly, it is not possible to use an external device like silicon strip detectors for beam definition. Using a full scale L3 muon chamber in a testbeam inside a magnet is also unpractical because of the large dimensions of the chamber. Therefore a special model chamber with the same wire configuration as the MM chambers, but with fewer and shorter cells, has been constructed. This model chamber consists of only 5 cells (compared to 15 in the MM chambers) with a length of only 65 cm (compared to 5.5 m for the MM chambers). The dimensions of the test chamber were chosen to fit the gap size of the spectrometer magnet available at the testbeam zone, which has a height of 80 cm, a width of 160 cm and a length of 120 cm in the beam direction. To measure the drift distance - drift time relation for different drift distances and track slopes, the chamber was mounted on a high precision translation-rotation table. Silicon strips at both sides of the setup were used for beam definition (see figure 4.1).

The drift time - drift distance relation depends in principle on all the quantities which influence the drift process. In practice the magnetic field B, the track slope S, the temperature T and the pressure P are the main parameters considered in constructing the cellmap. Variations in gas composition and contamination have not been studied. The testbeam experiment was designed in such a way that a good fraction of the ranges

	Min. (test beam)	Max. (test beam)	Min. (L3)	Max. (L3)
B	0.486 T	0.524 T	0.5 T	0.58 T
P	747 mmHg	768 mmHg	740 mmHg	800 mmHg
T	295 K	296 K	293 K	298 K

Table 4.1: **B**, P and T values at the testbeam and at L3

of possible combinations of B and P values listed in table 4.1 could be covered. The pressure could be adjusted to within one mbar over a range of 50 mbar, by means of a bubbler with a variable water level. The magnetic field was known to within 0.1%. The temperature was not under control but could be measured to within 0.1 degree.

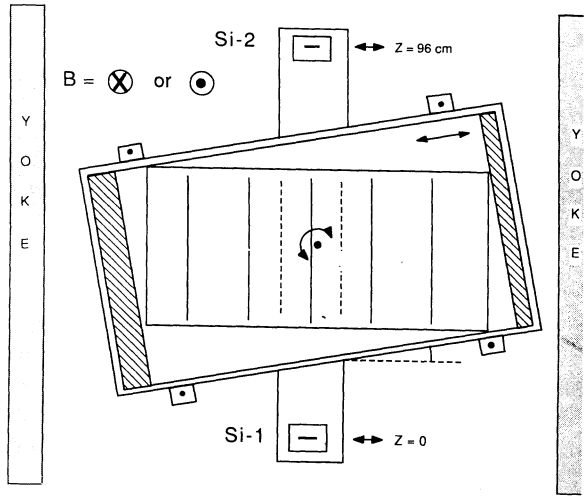

Figure 4.1: Schematic drawing of the test chamber and the translation rotation table. The translation range is 10 cm, the rotation range 22°. Silicon strip detectors at each side of the chamber are used as an external reference for the beam position.

In the next section the cellmap function for the L3 muon chambers will be discussed in detail. Section 4.3 is devoted to a description of the testbeam, the testbeam hardware

and the data collection. Chapter 5 deals with the construction of the cellmap function from these data, together with results and a discussion on the applicability of the function for L3.

4.2 The cellmap function $X(t)$.

A muon that crosses an L3 muon chamber creates about 100 ion-electron pairs per cm. All the created electrons start to drift towards the sense wires along different drift paths. The gas amplification in the vicinity of the wires results in about $10^4 - 10^5$ electrons collected on the sense wire per arriving drift electron, which corresponds to a signal of 300 mV at the output of the pre-amplifier. The threshold of the discriminator behind the pre-amplifier is set to 30 mV. This threshold level will be reached after the avalanches of $\approx$ 10 drift electrons have arrived at the sense wire.

From the drift time recorded in the TDC connected to one wire one can calculate a point P with coordinates $(X(t), Y(t))$ that lies on the muon track. $Y(t)$ will also depend on y_w, the y-coordinate of the wire; for the calculation of $X(t)$ the x-coordinate of the wire x_w is assumed to be zero. The original muon track parameters are determined from a fit through a set of such points collected for all the wires (16 in an MI or MO chamber, and 24 in an MM chamber). In principle all the points P are points in three dimensional space, but since the z-coordinate is not measured in the p-chambers but determined independently by the z-chambers, the problem of finding the point P in the p-chambers is treated in 2 dimensions.

The functions $X(t)$ and $Y(t)$ are taken to be the same for all the wires in a cell. They depend on the parameters $\tilde{B}, \tilde{P}$ and on the variables $\tilde{S}$ and t. The $\tilde{B}$ and $\tilde{P}$ stand for normalized deviations of the magnetic field and the pressure from nominal, fixed, values and are well known quantities (see equations 4.4 and 4.8). $\tilde{S}$ stands for the normalized slope of the track, where the slope of the track is the tangent of the angle between the track and the wire plane (see equation 4.2). The average value of the track slope for high energetic muons is about 11°. The drift time recorded by the TDC, after correction for the zero-time offset and the time of flight differences, is represented by t. The aim of the testbeam experiment is to find the relations $(X(t), Y(t))$, given the pressure and the magnetic field. The different effects to be taken into account are discussed in the following sections. For simplicity, the cellmap function is first derived for zero magnetic fields.

4.2.1 Geometrical effects

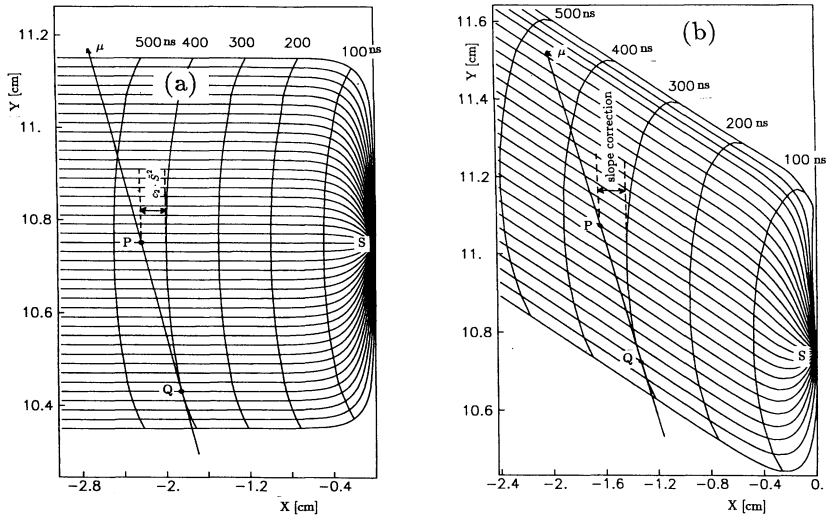

Figure 4.2: Slope correction without magnetic field (a) and with a magnetic field of about 0.5 T (b). Without magnetic field the slope correction is symmetric with S.

Consider a muon drift cell at zero magnetic field and at constant pressure and a muon track parallel to the wire planes of this cell. A first approximation of the position of this track as measured by one of the wires is :

$$\begin{aligned} X(t) &= V_x.t \\ Y(t) &= y_w \end{aligned} \tag{4.1}$$

where t is the corrected drift time, V_x the drift velocity and y_w the y-coordinate of this wire. All the electrons drift to this wire along different drift paths and arrive at slightly different times. The position along the track where the first few (≈ 10) drift electrons, that determine the trigger, originate from corresponds with the point Q where the track touches a line of equal average drift time, an "isochrone"(see figure 4.2).

The point $P = (X(t), Y(t))$ is defined as the point where the track crosses a "standard drift path". In the case of zero magnetic field the line $y = y_w$ is used: in the case of non-zero magnetic field, the Lorentz drift angle is taken into account and a line shown in figure 4.2(b) is used as standard drift path. The aim of the fit procedure is to collect enough points on the track in order to fit a track segment to the measurements found in the cell. All the wires in the cell are treated as being equivalent.

For the above sketched situation of a track parallel to the wire planes, the points P and Q are the same. If, on the other hand, the track is not parallel to the wire plane, the point Q does not correspond with $P = (X(t), Y(t))$ and additional corrections are needed (figure 4.2(b)). The slope of a track is defined as the tangent of angle ζ between the track and wire plane normalized to the tangent of 22.5^o:

$$\tilde{S} = \tan\zeta / \tan 22.5^o \tag{4.2}$$

The function $X(t)$ depends on the slope of the track. For tracks with nonzero slopes a correction on the drift distance calculated from equation 4.1 is needed. If no magnetic field is present, the correction is symmetric with respect to $\tilde{S}$. If the isochrones are perfectly parabolic, then this correction is parabolic in $\tilde{S}$, and the $X(t)$ relation becomes:

$$\begin{aligned} X(t) &= V_x.t + c_2.\tilde{S}^2 \\ Y(t) &= y_w \end{aligned} \tag{4.3}$$

If one assumes that the shape of the isochrones is constant in the cell, the slope correction does not depend on the drift distance or time. This assumption is not valid in the regions close to the sense and mesh planes where special corrections are needed. These corrections are discussed in section 4.2.5. Equation 4.3 was used during the extensive octant tests at zero magnetic field, which were done to check and calibrate the octants with cosmic rays and UV laser beams. Analytic estimates of the parameter c_2 were calculated using the wire chamber simulation program Garfield. For the standard L3 high voltages at B=0.5 T, running at B=0 ,a value of 1.95 was found for c_2 [40].

4.2.2 Pressure and temperature variations

The drift velocity is a function of the electric field **E** and of the particle density n which, in turn, is a function of P/T, where T is the temperature and P the pressure. The pressure in the chamber varies with the barometric pressure and is therefore not under control. If the cellmap function $X(t)$ is to be valid for all reasonable barometric pressures that can be expected during the running periods of the L3 experiment, then the pressure and temperature variations have to be incorporated into $X(t)$. One solution is to keep the cellmap function very simple, like equation 4.3, but to determine all the parameters for small ranges of P/T. This approach is impractical because a similar argument holds for the other quantities that affect the cellmap function, such as the magnetic field. Each combination of parameter settings needs its own data set and results in an independent fit. A more elegant solution is therefore to include some "pressure terms" and "magnetic field terms" in $X(t)$. This also introduces the possibility to check the dependence of $X(T)$ on B and P/T in a simple way.

In the following it is assumed that the electric field is constant, and well defined. The electric field is assumed to be equal to the plateau value. The variation of the drift

velocity around the plateau value can be expanded in a Taylor series expansion in P/T around the plateau value at nominal pressure and temperature, $P_o = 760$ mbar and $T_o = 293$ K respectively. The variation in P/T is written as:

$$\tilde{P} = \frac{\frac{P}{T} - \frac{P_o}{T_o}}{\frac{P_o}{T_o}} = (P\frac{T_o}{T} - P_o)/P_o \tag{4.4}$$

and the drift velocity is expanded as:

$$V_x = V_{x,o} + p_1\tilde{P} + p_2\tilde{P}^2$$

Pressure variations, and therefore density variations, will also affect the gain in the chamber. A linear gas gain correction as function of $\tilde{P}$ has been included. The relation $X(t)$ now becomes:

$$X(t) = p_o\tilde{P} + (V_{x,o} + p_1\tilde{P} + p_2\tilde{P}^2).t + c_2.\tilde{S}^2 \tag{4.5}$$

where $p_o.\tilde{P}$ is the gas gain correction, which enters through the threshold settings.

4.2.3 Geometrical effects at B $\neq 0$

If a magnetic field is present, the particles will drift under an angle α with respect to the electric field, as shown in figure 4.2 (b). The first complication presented by a nonzero field is the dependence of α on the electric and magnetic fields (see figure 3.3). The

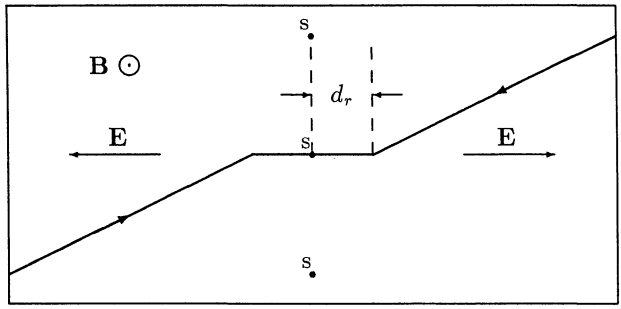

Figure 4.3: Standard drift path in a nonzero magnetic field. At distances $x < d_r$ the field and the standard drift path are perpendicular to the sense wire plane.

standard drift path is now chosen as follows:

$$y = \begin{cases} y_w & (x \leq d_r) \\ y_w + I_b \cdot \tan(\alpha) \cdot (x - d_r) & (x > d_r) \end{cases} \tag{4.6}$$

The shape of this line roughly corresponds to the drift line of the earliest arriving electrons. Very close to the sense wire the electric field increases. Since the drift angle is proportional to B/E, the particles start to drift parallel to the field lines, which at short distances, are more or less radial with respect to the sense wire. From extensive Monte Carlo studies [41] the distance d_r over which the drift paths are radial was estimated to be 3.5 mm, which is consistent with rough results determined with the UV laser [42]. The precise value chosen is not critical for the accuracy of the cellmap function, as long as it is fixed. The number I_b is 1 or -1, depending on which side of the sense plane the particle crossed the cell and on the sign of the magnetic field. The geometrical effects in a magnetic field are now not symmetric with respect to $\tilde{S}$. This means that a correction to $X(t)$ is required which is odd in $\tilde{S}$. Higher order terms in $\tilde{S}$ are included to compensate for deviations of the isochrones from a parabola; these terms are only important for large slopes. Collecting all the terms defined up to now results in:

$$X(t) = c_o + p_o.\tilde{P} + (V_{x,o} + p_1\tilde{P} + p_2\tilde{P}^2).t + c_1.\tilde{S} + c_2.\tilde{S}^2 + c_3.\tilde{S}^3 + c_4.\tilde{S}^4 \qquad (4.7)$$

4.2.4 Magnetic field corrections

The magnetic field in the vicinity of the L3 muon chambers varies as function of position. In the middle region the field is approximately 0.51 T, but closer to the doors the field goes up to 0.58 T (see chapter 2). The variable $\tilde{B}$ is introduced, which corresponds to the normalized deviation of the magnetic field from the nominal value of $B_o = 0.51$ T:

$$\tilde{B} = \frac{(B - B_o)}{B_o} \qquad (4.8)$$

Variations due to variations in the magnetic field can be incorporated in $X(t)$ in two different ways, from now on called method I and method II.

Method I. In this method a fixed drift angle α of 18^o is chosen, which corresponds to the drift angle at B=0.51 T, which implies that the standard drift path defined in equation 4.6 does not correspond to any physical electron drift paths in the cell whenever the magnetic field deviates from the nominal value. This results in a number of additional compensating corrections in $X(t)$:

$$\begin{aligned} X_1(t) &= c_o + V_{x,o}\cdot t + c_1\cdot\tilde{S} + c_2\cdot\tilde{S}^2 + c_3\cdot\tilde{S}^3 + c_4\cdot\tilde{S}^4 + c_5\cdot 0.049\cdot t\cdot\tilde{S} \\ &+ (b_o + b_1\cdot t + b_2\cdot\tilde{S} + b_3\cdot t\cdot\tilde{S} + b_4\cdot t\cdot\tilde{S}^2)\cdot\tilde{B} \\ &+ (p_o + p_1\cdot t + p_2\cdot\tilde{S} + p_3\cdot t\cdot\tilde{S} + p_4\cdot t\cdot\tilde{P})\cdot\tilde{P} \\ &+ \text{near-wire corrections} \\ Y_1(t)) &= y_w + I_b\cdot\tan(18^o)\cdot(X(t) - d_r) \end{aligned} \qquad (4.9)$$

Variations in the gain caused by variations in the magnetic field are included to first order $(b_o\cdot\tilde{B})$ in a similar way as the corrections in the gain due to pressure changes were

included. The terms $p_2.\tilde{S}.\tilde{P}$ and $b_4.\tilde{S}.\tilde{B}$ are corrections to first order in $\tilde{P}$ and $\tilde{B}$ on the lowest order slope correction term. All the other extra terms are corrections on the drift velocity V_x to compensate the deviation of the drift angle α from the assumed value of 18°.

Method II. The second method was developed to allow the drift angle to change with $\tilde{P}$ and $\tilde{B}$ including effects up to first order $\tilde{B}$ and up to second order in $\tilde{P}$. Since

$$\tan\alpha \propto \frac{B}{E/P}$$

the following parametrization was chosen:

$$\tan\alpha = \alpha_o.B + \alpha_1.\tilde{P} \tag{4.10}$$

The only additional magnetic field correction included in equation 4.7 is an additional correction to the drift velocity. The final expression used in the second method is therefore:

$$\begin{aligned} X_2(t) &= c_o + p_o.\tilde{P} + b_o.\tilde{B} + (V_{x,o} + p_1\tilde{P} + b_1.\tilde{B} + p_2\tilde{P}^2).t + c_1.\tilde{S} + c_2.\tilde{S}^2 + c_3.\tilde{S}^3 + c_4.\tilde{S}^4 \\ Y_2(t) &= y_w + I_b.(X(t) - d_r).(\alpha_o.B + \alpha_1.\tilde{P}) \end{aligned} \tag{4.11}$$

All the other corrections which were introduced in $X_1(t)$ are supposed to be absorbed in the corrected drift angle.

4.2.5 Near-wire corrections

Very close to the sense and mesh wires the electric field starts to deviate strongly from the homogeneous field in the middle region of the cell. An attempt was made to include several corrections to $X(t)$ for these regions. All these corrections are of the form:

$$\left(\frac{d - X(t)}{d - x_w}\right)^2 F_d(\tilde{S}) = \begin{cases} 0 & (X(t) \geq d) \\ \neq 0 & (X(t) < d) \end{cases} \tag{4.12}$$

where x_w is the x-coordinate of the wire (0 mm for a sense- and 50.7 mm for a mesh wire), and $F_d(s)$ is some function that only depends on the slope and is 0 for distances larger than d from the wire. Corrections were made for d=10 mm, 6 mm, and 3 mm with x_w=0 (near sense wire corrections) and for d=45 mm, 48 mm, 50 mm and 51 mm with x_w=50.7 mm (near mesh wire corrections). The first term in equation 4.12 is a weight function that ensures that the corrected drift time - drift distance relation $X(t)$ is still continuous. The correction is exactly 0 at the edge of the region (where $X(t) = x_d$) and

reaches its maximum at the wire. The functions $F_d(\tilde{S})$ have the form:

$$\begin{aligned} F_{10}(\tilde{S}) &= w_o + w_1.\tilde{S} + w_2.\tilde{S}^2 + w_3.\tilde{S}^3 \\ F_6(\tilde{S}) &= w_4 + w_5.\tilde{S} + w_6.\tilde{S}^2 + w_7.\tilde{S}^3 \\ F_3(\tilde{S}) &= w_8 + w_9.\tilde{S} + w_{10}.\tilde{S}^2 + w_{11}.\tilde{S}^3 \\ F_{45}(\tilde{S}) &= w_{12} + w_{13}.\tilde{S}^2 \\ F_{48}(\tilde{S}) &= w_{14} \\ F_{50}(\tilde{S}) &= w_{15} \\ F_{51}(\tilde{S}) &= w_{16} \end{aligned} \tag{4.13}$$

The constants $w_o, w_1, ...w_{16}$ have to be determined from the testbeam data. Both methods I and II (equations 4.9 and 4.11) use the same form for the near-wire corrections.

A complication with the near-wire corrections is the calculation of the inverse function for the Monte Carlo simulation program. Up to now the functions can be inverted analytically to determine the precise inverse function. This allows one to treat Monte Carlo data in exactly the same manner as real data as far as the fits are concerned. As soon as near-wire corrections are introduced, things become slightly more complicated: in the reconstruction one starts with

$$x_1 = V(\tilde{B}, \tilde{P}) \cdot t + x_o(\tilde{B}, \tilde{P}, \tilde{S}) \tag{4.14}$$

where V and x_o are known functions of $\tilde{B}$,$\tilde{P}$and $\tilde{S}$. If near-wire corrections are needed, say for $x \leq d$, then the calculated drift distance x is of the form:

$$x_2 = x_1 + F_d(\tilde{S})(\frac{x_d - x_1}{x_d - x_w})^2 \tag{4.15}$$

This is easily generalized in case more corrections are needed. The inverse function is needed to calculate the drift time t from the known drift distance x_2. Equation 4.15 can not be inverted in a simple way, since the quantity x_1 is unknown. This problem, which rapidly becomes more complicated if more near-wire correction terms are added to $X(t)$, was solved by modifying the cellmap function slightly, and iterating the correction in 4.15 several times:

$$\begin{aligned} x_2 &= x_1 + F_d(\tilde{S})(\tfrac{x_d - x_2}{x_d - x_w})^2 \\ x_3 &= x_1 + F_d(\tilde{S})(\tfrac{x_d - x_2}{x_d - x_w})^2 \\ \vdots &\quad \vdots \quad \vdots \\ x_n &= x_1 + F_d(\tilde{S})(\tfrac{x_d - x_{n-1}}{x_d - x_w})^2 \end{aligned} \tag{4.16}$$

With the correction functions of the form specified in 4.13 this converges rapidly such that $x_n \rightarrow \tilde{x} = x_\infty$ for n relatively small. Now the inverse function can be calculated directly from a given $\tilde{x}$ as:

$$\begin{aligned} x_1 &= \tilde{x} - F_d(\tilde{S})(\tfrac{x_d - \tilde{x}}{x_d - x_w})^2 \\ \tilde{t} &= (x_1 - x_o(\tilde{B}, \tilde{P}, \tilde{S}))/V(\tilde{B}, \tilde{P}) \end{aligned} \tag{4.17}$$

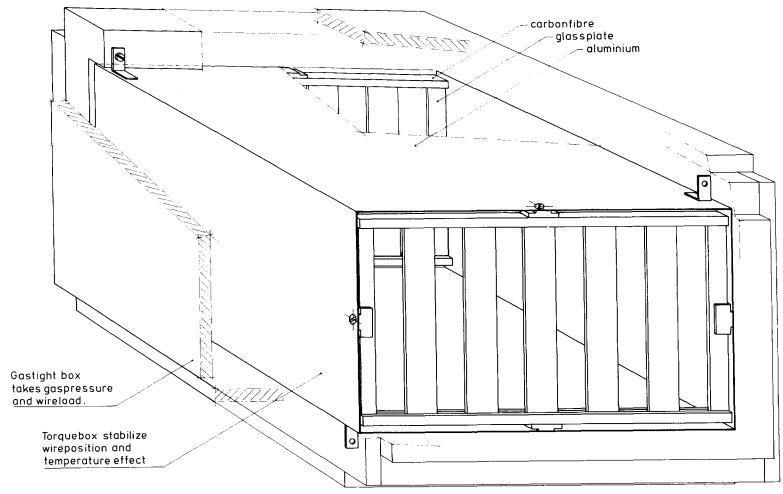

Figure 4.4: Drawing of the model chamber used in the testbeam experiment

The number of iterations required to let x_n converge depends mainly on $\tilde{S}$. For $\tilde{S} \leq 1$ about 4 iterations are enough to guarantee that $|\tilde{x} - X(\tilde{t})| \leq 1\,\mu$m .

In the next sections a testbeam setup will be described that was used to measure the unknown constants $p_o, ..c_0, .., b_o, ..., w_{16}$ with a small model chamber in an SPS testbeam at CERN. The analysis and results of these tests are presented in chapter 5, together with a discussion on the reliability of the parameters.

4.3 The test beam setup

4.3.1 The test chamber

A general problem associated with scale models is that the physical behaviour of the model is never exactly the same as that of the real system. This complicates the comparison. One has to take care to design and operate the model in such a way that the resemblance is as good as possible.

For the small test chamber, whenever possible, the same type of components were used as were used in the real L3 muon chambers. In total 5 cells with a length of 65 cm each were made. Small glass bridges were made at MIT with the same carbonfibre-

glass construction and the same assembly procedures as used for the L3 muon chambers. Instead of incorporating an adjustable middle bridge with a position monitor to correct for deformations in the chamber, a very stiff torsion free aluminum box is used. Since the box, the outer wall and the motor blocks are all constructed from aluminum, temperature effects on the glass bridge positions are minimized. The combination of the carbonfiber-glass bridges and this torsion box guarantees a very stable wire position. No correction mechanism or position monitor is required.

The electrostatic field in the test chamber had to be identical to the electrostatic field in the MM chamber. The dimensions of the torsion box are chosen such that the distance between the walls of the box and the wire planes is the same as the distance between the honeycomb covers of an MM chamber and the wire planes in the MM chambers. This keeps the electrostatic ground in the test chamber at the same relative position as in the real chambers. The drift properties of the chamber are not sensitive to the precise position of the electrostatic ground. Errors of up to 1 cm in the position of the ground plane will not significantly affect the drift properties of the chamber. [40]. Windows were cut in the box to allow the beam to pass through with minimum multiple scattering. The windows were covered with a fine wire grid to provide an electrostatic ground at the windows.

4.3.2 The precision translation and rotation table

In order to translate and rotate the chamber in the beam a very flat translation-rotation table was designed at ETH-Zürich. The bottom part of the table is a frame which is bolted to the magnet yoke. This frame, 730 mm wide and 1000 mm long, contains 4 steel strips to support a translation table. The height of frame and translation table together is 48 mm. The translation table can be translated over 16 cm by means of a hydraulic system. A rotation platform is mounted on top of the translation table. The rotation axis is exactly in the center of the translation table. The platform can be rotated independently by means of a second hydraulic cylinder, also mounted on the translation table. The total rotation range of the plateau is 22° (from $-11°$ to $+11°$). The test chamber is mounted on the rotation plateau and kept in place between two arms.

Two high precision incremental length measuring systems (Heidenhain, LS 803) were used to read out the relative table position within 10 μm . These measuring systems consist of two glass scales with a 40 μm increment grating, shifted over 20 μm with respect to each other. A scanning head with a long-life lamp at one side of the grid and two photo cells at the other side were guided along the glass scale. The grating was mounted to the table frame and the scanning head on the translation table (and similar for the rotation platform). If the scanning head moves along the glass scale, two signals are produced with a relative phase difference of 90°. These signals were processed by an incremental position decoder (up-down counter type SEN 2IPE-2019 in CAMAC). Using

the phase information of the two signals this results in a relative position measurement of 10 μm .

The hydraulics of the table was fully computer-controlled (see figure 4.5). The signal produced by a Digital to Analog Converter (SEN DAC2011/0) passed a Power Amplifier (Heller Hydraulik, VG40) and controlled the proportional valves in the hydraulic system of the table. Together with the table position readout this resulted in a feedback control system. Due to the usual problems of delayed responses in the control loop the table position could be controlled only to within 50-100 μm . However, the absolute position of the table, measured with the two incremental length measuring systems, was known to within 10 μm .

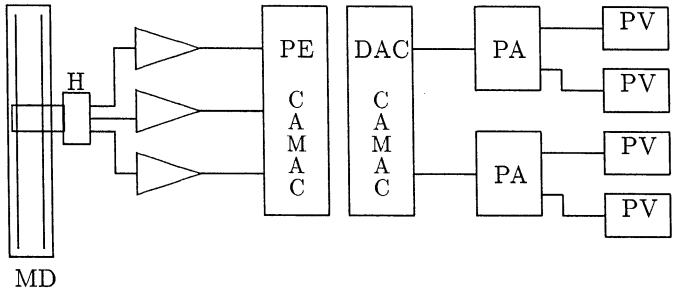

Figure 4.5: Principle of the table position control loop. The translation and rotation positions are read out by the optical measurement device (MD). The output of the photo cells (two cells for the position, one for the calibration marks) is amplified and passed to the Position Encoder (PE). The VAX online computer controlled the position and movement via a dual DAC. The DAC output was amplified (PA), and passed onto the Proportional Valves (PV) to control the movement.

4.3.3 Extended rotation range

In order to map the whole range of possible L3 muon chamber track segments, a rotation range from -22^o up to $+22^o$ is needed, which is twice the available range. To achieve this, the table frame was mounted with a fixed angle of $\approx 11^o$, called ψ, with respect to the beam axis. This results in a range of 0^o to $+22^o$. The range from -22^o to 0^o was mapped by reversing both the polarity of the magnetic field and the sign of the charge of the particle beam (see figure 4.6). This procedure does not affect the particle trajectory through the setup but inverses the drift angle, which is equivalent to tracks with slopes in the range of -22^o to 0^o.

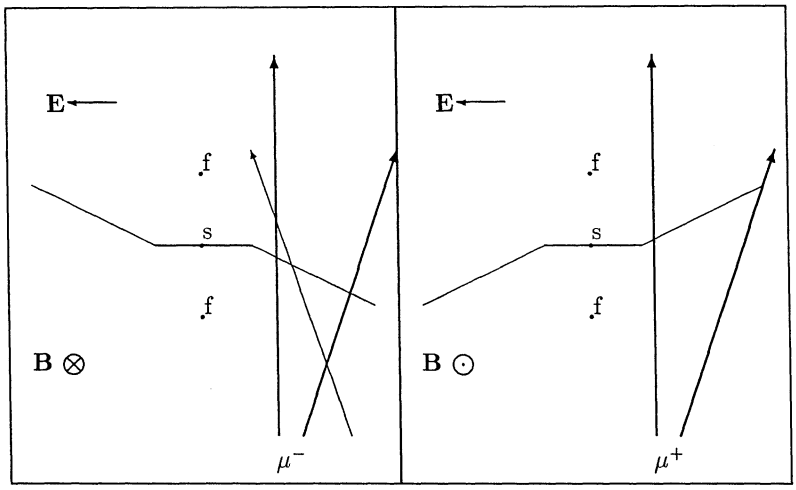

Figure 4.6: Reversing the magnetic field and the sign of the charge of the beam particles does not effect the particle trajectory in the chamber, but reverses the drift angle. This is equivalent to mapping the negative slope tracks: the bold track in the right figure is equivalent to the thin track in the left figure.

4.3.4 The table geometry.

For the fit procedure described in the next chapter one needs the position of the particle track, measured by the silicon strip detectors, in the local chamber coordinate frame. The coordinate transformation between the laboratory frame (defined by the magnet and the silicon strips) and the chamber frame (defined by the wire planes in the chamber) is discussed in this section. An attempt was made to make a high precision survey of the setup in order to fix the 6 geometrical quantities that determine the coordinate transformations: the translation and rotation offsets T_o and R_o, the rotation point (x_o, y_o) of the table, the length of the rotation arm L_r and the fixed angle ψ of the frame with respect to the beam. However, since this survey turned out to be far too inaccurate, these geometrical quantities are now determined from the data simultaneously with the cellmap parameters.

The table frame is bolted on the magnet yoke at an angle ψ of roughly 11° with the beam direction. The silicon strips are mounted on rigid feet, which are bolted on two aluminum support plates of 8 cm width and 2 cm thickness. These plates are fixed to the frame and thus to the magnet. The first coordinate system to be defined is the laboratory frame $\vec{x}^{lab} = (x^{lab}, y^{lab})$. The axes of the laboratory frame are defined with respect to the

silicon strips. The y-axis goes through the first microstrips of both silicon strip detectors and is pointing roughly parallel to the beam. The x-axis lies in the horizontal plane parallel to the strips (see figure 4.1). The silicon strips can be shifted on their supports to align the strips with the particle beam. After this alignment their positions are locked to the laboratory frame with lock screws.

The precision translation table is mounted on the fixed frame (see figure 4.1). For the table frame the table coordinate system $\vec{x}^t = (x^{tr}, y^{tr})$ is defined, which is the laboratory frame rotated over the angle ψ and translated over a distance determined by the translation readout. This transformation from the laboratory frame to the translated table frame can be written as

$$\vec{x}^{tr} = R_\psi(\vec{x}^{lab}) + \vec{T} \tag{4.18}$$

where R_ψ is the rotation matrix for rotation over ψ and $\vec{T}$ the translation vector

$$\vec{T} = (I_x * 10\mu\text{m} + T_o, 0) \tag{4.19}$$

determined by the translation offset T_o, and the translation readout I_x in counts of $10\,\mu$m . The rotation platform is fixed on top of the translation table and the chamber is rigidly fixed on this platform. The chamber is rotated via a linear displacement of a rotation arm, again within an accuracy of 10μm. The rotation angle is defined by the rotation readout I_r, the rotation offset T_r, and the rotation arm length L_r as

$$\varphi = \arctan((I_r * 10\mu\text{m} + T_r)/L_r) \tag{4.20}$$

The coordinate transformation from the translated table frame to the chamber frame $\vec{x}^{ch} = (x^{ch}, y^{ch})$ then becomes:

$$\vec{x}^{ch} = R_\varphi(\vec{x}^{tr} - \vec{x}_o) + \vec{x}_o \tag{4.21}$$

where R_φ is the rotation matrix for rotation over φ.

The only interesting coordinate systems are the laboratory frame $\vec{x}^{lab}$ and the chamber frame $\vec{x}^{ch}$, since one either wants to express the silicon strip track in the chamber frame, or the chamber track in the laboratory frame. Combining all the elementary intermediate coordinate transformations defined above, one obtains for the transformation from beam frame to chamber frame and for the transformation from chamber frame to beam frame respectively:

$$\vec{x}^{ch} = R_\varphi(R_\psi(\vec{x}^{lab}) + \vec{T} - \vec{x}_o) + \vec{x}_o \tag{4.22}$$

$$\vec{x}^{lab} = R_{-\psi}(R_{-\varphi}(\vec{x}^{ch}) - \vec{x}_o) + \vec{x}_o - \vec{T}) \tag{4.23}$$

4.3.5 Silicon strip detectors

Two silicon strip detectors were used as an external beam reference. These systems, together with all the readout electronics, were supplied by Zeuthen, DDR. Each detector

consists of a silicon crystal with p-doped electrodes at one side (50 μm wide and 2 cm long) and an n-doped electrode at the other side. A constant voltage difference of $\approx$ 100 Volt is maintained over the strips in the reversed bias direction, creating a homogeneous electric field between the strips and the positive electrode. If a highly energetic particle crosses the detector it will ionize atoms along its path. The resulting electron cloud drifts towards the strips where the charge is collected and amplified. In total 120 strips on each detector were read out.

The strips were mounted with the microstrips in the vertical (y) direction, and therefore measured the x coordinate of the crossing particles in a 6 x 20 mm^2 window. The position resolution is calculated assuming a homogeneous distribution of particles over each strip, and equals $\sigma_x = 50/\sqrt{12}$ μm for both strip detectors.

4.3.6 The testbeam and the trigger

For the measurements the testbeam X3 in the SPS-west area was used. This is a tertiary beam, custom-built for L3 testbeam experiments. Protons in the momentum range of 400-450 GeV were slowly extracted from the SPS beam and directed towards a target. The secondary particles are divided over two beams, H1 and H3. The H3 beam is focused on a second target to produce tertiary particles, which are then momentum-selected and transported as X3 beam into the test area. For the muon chamber testbeam only particles with a momentum of 50 GeV/c were used. Lead filters behind the target were used to remove the electrons. The resulting beam contained $\approx$ 90% $\pi^{\pm}$ and $\approx$ 10% $\mu^{\pm}$, where the sign of the particles was defined by the secondary beam.

The center of the beam was steered with the bending magnets through the first silicon strip detector. The second silicon strip detector was then moved into the beam. The position of the beam focus point was tuned with the quadrupole magnets and was used to optimize the trigger rate. The trigger was defined by the coincidence of three

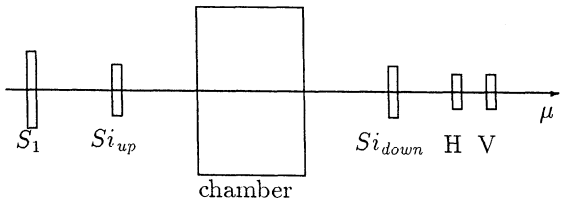

Figure 4.7: Schematic drawing of the counters used in the trigger.

scintillation counters S_1,H and V (see figure 4.7). The beam first crossed a large counter S_1 about 8 meters in front of the test setup. This signal was used as a trigger for the slow

silicon strip readout, in coincidence with a veto from the "VAX-busy" signal if the online computer was not ready. Next the particle crossed the upstream silicon strip detector Si_{up}, the test chamber and the downstream silicon strip detector Si_{down}. Just behind Si_{down} two small scintillator counters were mounted, with active areas of 1 x 2 cm^2. One of the two was mounted in the horizontal (H) plane and the other in the vertical (V) plane. The coincidence between the H and V counters determined the trigger. Since the silicon strip detectors are only 6 mm wide, the fraction of triggers having good silicon strip data was about 60 %. Due to the much smaller area of the H and V counters, their timing was more accurate than the timing of the large S_1 counter. The delays between the different scintilator counter signals were chosen such that the the combination of H and V determined the trigger.

4.3.7 The testbeam magnet.

The testbeam magnet W75 at the X3 testbeam zone is a dipole spectrometer magnet with a field adjustable between +1.1 Tesla and −1.1 Tesla. The region of interest is a small "box" in the middle of the magnet where the tracks are passing and the drift process takes place. This box extends in the horizontal plane up to the longest drift distance, which is 5 cm, and is limited in the vertical direction by the size of the horizontal trigger finger counter, which is 1 cm high. In order to keep the field as homogeneous as possible no magnetic materials were used in the setup except for the steel rails in the table. These rails consist of four steel strips and are located inside the translation table about 1 cm from the bottom magnet pole. Since the magnetic field distortions fall off quadratically, this will not influence the field in the central region, 40 cm above the table, significantly.

Measurements of the magnetic field were made at 0.3, 0.5 and 0.7 T with the steel rails in place. A field map was produced with a Hall probe to measure the field homogeneity and direction and the central field value was measured with a NMR probe. In the small region of interest around the beam the field was homogeneous to within 3 gauss.

All the measurements were made by first turning up the field to 1.1 Tesla, and then lowering it down to the final setting. This is done in order to magnetize the iron yoke in a well defined manner.

Chapter 5

Testbeam data analysis

5.1 Introduction

The analysis of the testbeam data was performed with an adapted version of the L3 muon chamber reconstruction program. Special additions were needed to incorporate the silicon strip analysis. The silicon strips measure the track independent of the test chamber. Time of flight calculations were simplified and the track ambiguity was resolved in an early stage by means of the silicon strip data. In section 5.2 the "p-segment" reconstruction in the L3 muon chambers is outlined. The analysis of the testbeam data is explained in section 5.3. The track reconstructed from the silicon strip hits is compared with the track reconstructed from the test chamber data. A χ^2-fit is used to minimize the difference between these two reconstructed track segments with respect to the 6 geometry parameters defined in section 4.3.4 and the cellmap parameters for the different cellmap functions presented in section 4.2. The results of these fits are presented in this chapter. It turns out that both methods I and II to convert from drift time to drift distance, introduced in chapter 4, give comparable results with comparable errors. Since the second method, which incorporates a variable drift angle, results in a simpler cellmap function, this method should be favoured in the L3 reconstruction and Monte Carlo programs. Additional simplifications are possible if data very close to the wire planes are removed from the fit and slightly larger errors at small drift distances are accepted. Some results using a simple cellmap function are presented in section 5.6.3. The chapter concludes with some remarks on the accuracy of the results and their applicability to L3.

5.2 Track fits in the L3 muon chambers

First consider the case of real L3 data. The data from the muon detector are ordered per octant, chamber and cell. Under normal conditions only a few track segments will be found in the data. All the hits in three neighbouring cells are studied simultaneously to locate "p-segments". A p-segment is that part of a muon track which is reconstructed in one of the three p-chamber layers of the detector, and a z-segment the part fitted in one z-chamber layer. First a histogram method is used to collect data from these three

cells that may belong to the same track segment: a straight line is fitted through pairs of wire hits and the slope and offset are booked in a histogram. Since it is not yet known on which side of the sense plane the particle crossed, the line fit is done on both sides of the sense plane. If a track crossed the cells, this will result in two or more peaks in this histogram. The data points that contribute to the highest peak are collected and a first χ^2-fit is made to a parabola, which is a good approximation for a circular track segment. After the first fit all the data are reconsidered: a 10 mm wide road is defined around the track segment and all the data within this road are "picked up" for the next fit. After refitting with this extended data set, the points with the largest contribution to the χ^2 value of the fit are dropped if the distances between these points and the track are larger than 1 mm. The remaining data are refitted. This procedure is repeated once more. Then the final track parameters are determined and stored for global track matching.

The above fits are performed to points $\{X_i, Y_i\}$ calculated from the TDC data and the drift-time drift-distance relations presented in section 4.2. The drift time t used in the calculations is the time registered by the TDC corrected for signal propagation delays and time of flight of the particle. To calculate these quantities one needs the position of the particle track in the detector, which is only known after the p- and z-segments found in the different muon chamber layers have been matched to form complete tracks. As long as this information is not available, an average signal propagation and time of flight is calculated using the relation $z = 0.4 \cdot y$, which corresponds with a track roughly through the middle of the octant. The cellmap function also requires the values of **B**,P,T and the track slope S. The pressure and temperature can be assumed to be known exactly (assumed constant over the volume of a chamber). The magnetic field on the other hand, can vary appreciably as function of z, especially in the MO chambers as shown in figures 2.5 and 2.8 in chapter 2. Final values of the local magnetic field are again only available after a global fit has been made. The track slope influences the precise value of the calculated values of $\{X_i, Y_i\}$ with up to ≈ 1 mm corrections on X_i. Before the first fit is made to the data points $\{X_i, Y_i\}$ in the chamber, the parameter S in the cellmap function is set to zero. For the later fits S is chosen to be the track slope calculated from the previous fit to the same segment. Tests with the reconstruction software showed that this procedure converges rapidly.

After the p-segments and z-segments have been constructed independently, the segments are matched to form complete tracks through the muon detector. This results in the 3-dimensional information needed to calculate the correct signal propagation time, the time of flight corrections and the correct local magnetic field values. After all these corrections have been made the fit is repeated once more to improve the results before the final track parameters are stored.

5.3 Track fits at the testbeam

At the testbeam the track fit is considerably less complicated. All the valid tracks are confined to a very small region limited by the active area of the silicon strips (6 x 20 mm^2) and the two finger counters behind the last silicon strip detector with an active area of 10 x 10 mm^2 (see figure 4.7). One of these finger counters determines the zero time of the trigger. Since the tracks are all confined to a small region of the chamber, the time of flight corrections and the signal propagation corrections are identical for all the events. The magnetic field **B** is also known exactly from the start since the field in the region of interest is very homogeneous and well known. The fit procedure is the same as that used in the L3 muon chamber analysis outlined in section 5.2. First a histogram method is used to collect the data followed by the same series of fits to select data. The slope correction is determined iteratively in the same manner as in the L3 analysis program.

All the events with hits in the chamber and in both the silicon strips can be used in the fit. The program produces a data summary file that contains the run and event numbers, the silicon strip hits, the table position readout and the (corrected) TDC data of the events. This file is used by the separate fit program to determine the cellmap function parameters.

To measure the quality of the fit, the track segment found in the test chamber is compared with the track segment calculated from the silicon strip hits, the known magnetic field and the known particle momentum of 50 GeV/c. First the center of the track circle defined by the silicon strips in the laboratory frame is calculated. This point is transformed to the chamber frame (x^{ch}, y^{ch}) by means of the coordinate transformation defined in equation 4.22, which results in the point (x_c^{ch}, y_c^{ch}). For each wire a "silicon strip point" (x_s, y_s), which is the intersection of this circle with the standard drift path, is then determined by solving the equations:

$$y_s = y_w + S_b\alpha(x_s - x_w - x_d)$$

$$(x_s - x_c^{ch})^2 + (y_s - y_c^{ch})^2 = R_o^2$$

The solution (x_s, y_s) is compared with the corresponding point (X_{fit}, Y_{fit}) found from the test chamber. Note that the point (x_s, y_s) depends directly on α, (and therefore on the parameters α_o and α_1 defined in equation 4.11), and via (x_c^{ch}, y_c^{ch}) on the geometry parameters defined in section 4.3.4.

The silicon strip electronics only registered the microstrips that were "hit". No ADC signals were available for a more sophisticated center of gravity calculation. If more than one strip is hit, the event could still be accepted if these hits are direct neighbours (position is the average position of the "cluster" of hit strips). If the strips are not neighbours, then one of the hits is almost certainly a spurious one, quite a frequent occurrence during some of the runs. To minimize the possibility of mistakes, all events

with more than one hit in one of the two strip detectors were rejected. It was attempted to locate the noisy strips using Poisson statistics: if the beam is homogeneously distributed over the micro strip detector, then each micro-strip has the same probability to register a hit. The number of hits registered on the strips for a run of several thousands of events, should show a Poisson distribution. Strips that register significantly more hits than the number expected from this distribution could then be removed. It turned out though, that the distribution did not resemble a Poisson distribution [40]. A very sharp cut on noisy strips was therefore not possible. Some of the very noisy strips were therefore removed from the data by hand in order to reduce the amount of spurious hits.

5.4 Fit procedure

The data collected in the data summary files were used to fit the geometry parameters $\mathbf{g} = \{T_o, R_o, x_o, y_o, L_r, \phi\}$ defined in section 4.3.4 and the cellmap parameters $\mathbf{c} = \{V_{x,o}, c_o, c_1, ..., w_{16}\}$ introduced in section 4.2. Two models were constructed, method I using a fixed drift angle and method II with a drift angle that varies with $\tilde{B}$ and $\tilde{P}$. Both models have some parameters in common, but some parameters are only included in one of the two models. However, for both models the cellmap functions have the general form:

$$X_{fit,i}(t, \mathbf{c}) = \sum_{k=1}^{n_c} T_{k,i} c_k \tag{5.1}$$

where $c_k (k = 1, ..., n_c)$ are the cellmap parameters and $T_{k,i}, (k = 1, ..., n_c)$ the known terms that only depend on t, $\tilde{B}$, $\tilde{S}$ and $\tilde{P}$. The index i runs over all the wires and all the events included in the fit. In this section the fit procedure is described in general.

The dimensions of the parameters c_k are chosen as follows: the coordinates $X(t)$ and $Y(t)$ are always expressed in $[mm]$ and the drift time t in [ns]. Since $\tilde{B}$,$\tilde{P}$ and $\tilde{S}$ are dimensionless quantities, the dimension of all the parameters c_k is [mm], except for those parameters that contribute to the drift velocity, which have dimension [μm /ns].

The parameters were determined from a χ^2-minimization. The χ^2-function that was minimized is:

$$\chi^2 = \sum_{i=1}^{N} w_i (x_{s,i}(\mathbf{g}) - X_{fit,i}(t_i, \mathbf{c}))^2 = \| x_s(\mathbf{g}) - X_{fit}(\mathbf{c}) \| \tag{5.2}$$

where the sum runs over all the wires and all the selected events. N is the total number of accepted hits. Note that the point x_s defined by the silicon strips only depends on the geometry parameters $\mathbf{g}$, and that the point defined by the TDC data X_{fit} depends only on the cellmap parameters $\mathbf{c}$. For the weights the usual expression $w_i = 1/\sigma_i^2$ is used, with some additional corrections that are discussed in section 5.4.1. The optimal values for the parameters $\mathbf{g}$ and $\mathbf{c}$ are those that minimize the quantity χ^2. Usually the

χ^2-function is constructed such that one of the two values (x_s or X_{fit}) is known from a direct measurement, and that the other depends on the unknown parameters that have to be determined. In this problem the parameters are divided over both x_s and X_{fit}. This will only work well if **g** and **c** are independent: if **g** and **c** contain a common parameter, the minimum of the χ^2-function can be ill defined. This problem was taken care of when the functions defined in section 4.2 were constructed. At the minimum of the χ^2-function all the derivatives of χ^2 with respect to the parameters vanish:

$$2\chi\frac{\partial\chi}{\partial c_j} = 0, \quad j = 1,2,...,n_c \tag{5.3}$$

$$2\chi\frac{\partial\chi}{\partial g_l} = 0, \quad l = 1,2,...,n_g \tag{5.4}$$

where n_c and n_g are the number of (linear) parameters in $X(t)$ and the number of (nonlinear) parameters in the geometry respectively.

Since the cellmap function $X(t)$ was constructed to be linear in the parameters c_j, equation 5.3 results in a set of n_c linear equations. Substituting equation 5.1 into 5.3 results in the usual set of linear equations:

$$\sum_i^N w_i x_{s,i} T_{j,i} = \sum_k^{n_c} \left(\sum_i^N w_i T_{j,i} T_{k,i} \right) c_k \quad \text{for } k = 1,...,n_c \tag{5.5}$$

The left hand side is a (calculable) vector of n_c elements, and the right hand side is the product of a (calculable) n_c x n_c matrix and a vector of the unknowns c_j:

$$\vec{B}_j = \mathbf{E}_{j,k}\vec{c}_k \tag{5.6}$$

The χ^2-equation is not linear in the geometry parameters. Equation 5.4 is therefore solved iteratively. Since all the derivatives of $x_{s,i}$ with respect to the geometry parameters exist for all events i, the Jacobian is:

$$Dx_s = \begin{pmatrix} \frac{\partial x_{s,1}}{\partial g_1} & .. & .. & \frac{\partial x_{s,1}}{\partial g_{n_g}} \\ .. & & & .. \\ .. & & & .. \\ \frac{\partial x_{s,N}}{\partial g_1} & .. & .. & \frac{\partial x_{s,N}}{\partial g_{n_g}} \end{pmatrix} \tag{5.7}$$

If $\tilde{\mathbf{g}}$ is close to the correct solution **g** for the geometry parameters, x_s can safely be written as a generalized Taylor series:

$$x_s(\mathbf{g}) = x_s(\tilde{\mathbf{g}}) + Dx_s(\tilde{\mathbf{g}})(\mathbf{g} - \tilde{\mathbf{g}}) + \mathcal{O}(\| \mathbf{g} - \tilde{\mathbf{g}} \|) \tag{5.8}$$

If this expression for x_s is substituted in 5.2, one finds:

$$\chi^2 = \min \| X_{fit,i}(t, \mathbf{c}) - x_s(\tilde{\mathbf{g}}) - Dx_s(\tilde{\mathbf{g}})(\mathbf{g} - \tilde{\mathbf{g}}) \| \tag{5.9}$$

This problem is linear in the "unknowns" $(\mathbf{g} - \tilde{\mathbf{g}})$. If 5.9 is written out in detail, and $J_{k,i}$ is written for $\frac{\partial x_{s,i}}{\partial g_k}$ and h_k for $(g_k - \tilde{g}_k)$, one obtains:

$$\chi^2 = \sum_i^N w_i \{x_{s,i}(\tilde{\mathbf{g}}) - X_{fit,i}(t, \mathbf{c}) + \sum_k^{n_g} J_{k,i} h_k\}^2 \tag{5.10}$$

Working out equation 5.4, where expression 5.10 is substituted for χ^2, results in equations analogous to equations 5.6:

$$\frac{\partial \chi^2}{\partial g_{l'}} = 0 \Longrightarrow$$

$$\sum_i^N w_i (x_{s,i}(\tilde{\mathbf{g}}) - X_{fit,i}(t, \mathbf{c})) J_{l',i} = \sum_k^{n_g} \left(\sum_i^N w_i J_{l',i} J_{k',i} \right) h_k \quad \text{for } k = 1, ..., 8$$

The left hand side is again a vector of n_g elements and the right side is the product of a n_g x n_g matrix and the unknowns h_k:

$$\vec{B}'_j = \mathbf{E}'_{l'k'} h_{k'} \tag{5.11}$$

The minimization problem is equivalent to solving the matrix equations 5.11 and 5.6 simultaneously. First a set of initial values $\mathbf{c}$ and $\tilde{\mathbf{g}}$ is selected. New values are determined by solving:

$$\begin{pmatrix} \vec{B} \\ \vec{B}' \end{pmatrix} = \begin{pmatrix} \mathbf{E} & \emptyset \\ \emptyset & \mathbf{E}' \end{pmatrix} \begin{pmatrix} \mathbf{c} \\ \mathbf{g} - \tilde{\mathbf{g}} \end{pmatrix} \tag{5.12}$$

The matrix inversion is calculated with a standard, double precision CERN program library routine MATIN2. The solution vector $(\mathbf{c}, \mathbf{g} - \tilde{\mathbf{g}})$ defines new approximations $\mathbf{c}$ and $\mathbf{g}$ for the cellmap and geometry parameters. This method always gave stable results for the up to 40 x 40 matrix inversions performed. After each iteration the new parameters were compared with the previous set. If the variation in each of the parameters became less than $10^{-5} - 10^{-6}$ the procedure was stopped, which approximately corresponds to the statement that

$$\chi^2 = \| \, x_s(\mathbf{g}) - X_{fit}(\mathbf{c}) \, \|$$

reached its minimum. The results of the different fits are presented in sections 5.5 and 5.6 for method I and method II fits respectively.

5.4.1 Calculation of the weights w_i

After one fit was made to the testbeam data, the resolution of the test chamber as function of drift distance and drift angle was determined. The resolution was fitted to a polynomial function of the form:

$$\sigma^2(x, S) = 0.011 + 0.00074 \cdot x + 0.026 \cdot S + 0.0058 \cdot (x - 3)^2 + 0.027 \cdot (x - 50)^2 \tag{5.13}$$

The last two terms are only included for $x \leq 3$ mm or $x \geq 50$ mm respectively. The resolution σ^2 was determined from early fits to method I (equation 4.9) and is assumed not to depend on the precise shape of the cellmap function. If one or more of the parameters in the cellmap function deviate from the ideal value, this will result in a shift for all the data points in the cell. A fit to these shifted data points results in a shifted track but with (almost) the same resolution (same shift for all the points or different shifts that "rotate" the track in the case of V_x errors). This resolution function is fixed throughout the different fits described in the following sections.

The weights w_i in the χ^2-fit (equation 5.2) depend on the resolution function as $w_i = 1/\sigma(x, \tilde{S})^2$. The data were collected at 3 different pressures and 3 different magnetic field values. It is preferable if data at all various drift angles and positions, and for all the pressure and magnetic field settings give roughly the same contribution to the χ^2 calculation. To compensate for the uneven distribution of the events at different pressures and magnetic field values, a scaling factor is applied:

$$w_i = \frac{1}{\sigma(x, \tilde{S})^2 \cdot n_{x,\tilde{S},B,P}}$$

where $n_{x,\tilde{S},B,P}$ is the fraction of hits at a given magnetic field and pressure and in given x and $\tilde{S}$ ranges. The drift range was subdivided in 26 bins, the slope in 5 bins and the magnetic field and pressure in 3 bins each.

The other quantity in equation 5.2 is the "fit error" $D = x_{s,i}(\mathbf{g}) - X_{fit,i}(t_i, \mathbf{c})$. The two points $x_{s,i}(\mathbf{g})$ and $X_{fit,i}(t_i, \mathbf{c})$ are directly calculated from the cellmap function and the silicon strip data. The quantity that actually has to be minimized is the distance from X_{fit} to the track, the perpendicular error. The dependence on the slope of this error (see figure 5.1) is absorbed in the weight factor as:

$$w_i = \frac{\cos(\alpha + \zeta)}{\cos(\alpha)\sigma(x, \tilde{S})^2 \cdot n_{x,\tilde{S},B,P}} \tag{5.14}$$

This is the final form of the weights which is used in all the fits described in the following sections.

5.4.2 Covariance matrix and error estimation

The covariance or error matrix $Cov(c_j, c_k)$ is defined as:

$$Cov(c_j, c_k) = \{\sigma_{jk}\} = (\mathbf{A})^{-1}_{jk}$$

where the matrix $\mathbf{A}$ is given by:

$$(\mathbf{A})_{jk} = \frac{1}{2}\left\{\frac{\partial^2 \chi^2}{\partial c_j \partial c_k}\right\}$$

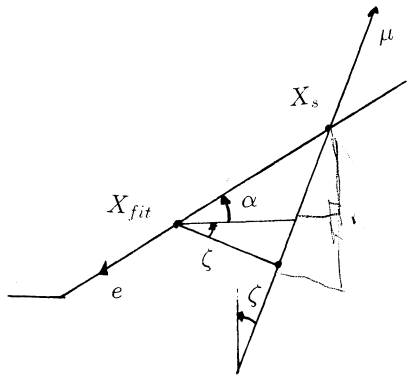

Figure 5.1: The weights absorb the dependence of the perpendicular error in order to calculate the distance between the cellmap point (X_{fit}, Y_{fit}) and the track defined by the silicon strips.

This matrix is used to estimate the errors of the fitted parameters: the diagonal elements of the matrix correspond to the variances of the parameters $\sigma_k = (\mathbf{A})^{-1}_{kk}$, and the off-diagonal elements correspond with the covariance $Cov(c_j, c_k)$ between different parameters. The correlation coefficient $\rho(c_j, c_k)$, which is defined by

$$\rho(c_j, c_k) = \frac{Cov(c_j, c_k)}{\sqrt{\sigma_j \cdot \sigma_k}}$$

is a measure of the "independence" of the parameters.

For the linear cellmap parameters the matrix **A** corresponds to the matrix **E** in equation 5.6. For the non-linear geometry parameters the matrix **A** is approximated by **E** in equation 5.11, which corresponds to the approximation

$$\frac{1}{2}\frac{\partial^2\chi^2}{\partial c_j \partial c_k} = \frac{1}{2}\frac{\partial\chi}{\partial g_j}\frac{\partial\chi}{\partial g_k}$$

where all the second order derivatives are ignored. For some of the fits the correlation matrix is presented in the following sections.

5.5 Method I: fixed drift angle

The first model fitted to the testbeam data was method I, defined in equation 4.9. In this model a constant drift angle is assumed [41]. Equation 4.9 is rewritten in the standard

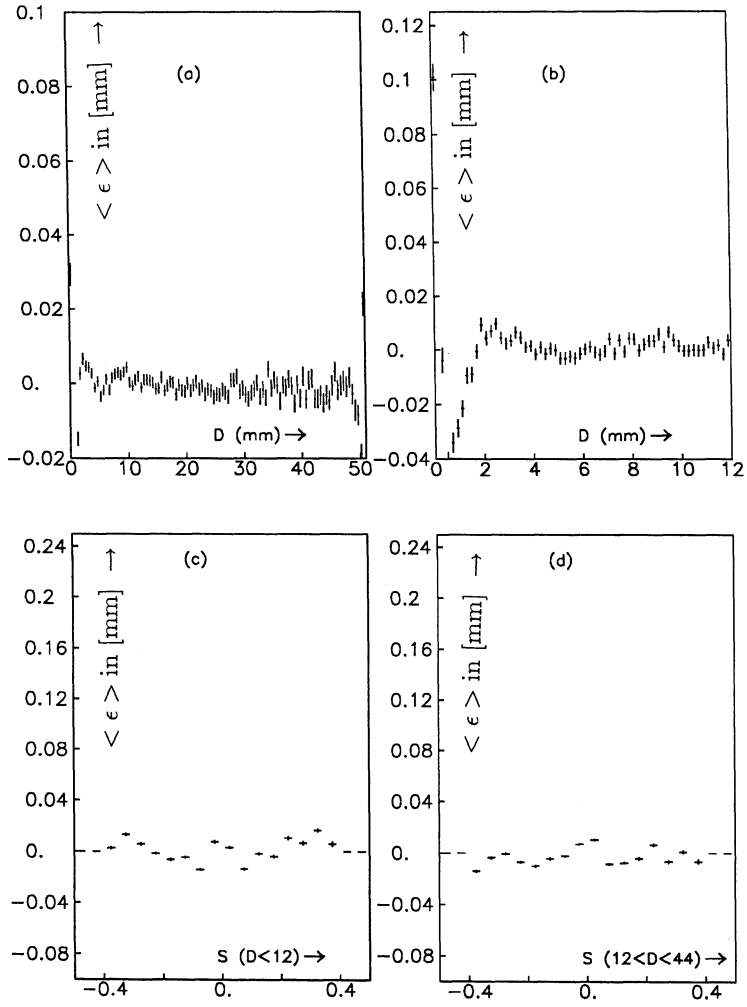

Figure 5.2: Fit errors of method I fit, versus drift distance (a), vs drift distance for $x \leq 12$ mm(b), versus slope for $x \leq 12$ mm(c) and versus slope for 12 mm $\leq x \leq 44$ mm (d).

form by renaming the parameters:

$$\begin{aligned} X_1(t) &= c_1 + c_2 \cdot t + c_3 \cdot \tilde{S} + c_4 \cdot \tilde{S}^2 + c_5 \cdot \tilde{S}^3 + c_6 \cdot \tilde{S}^4 + c_7 \cdot 0.049 \cdot t \cdot \tilde{S} \\ &+ (c_8 + c_9 \cdot t + c_{10} \cdot \tilde{S} + c_{11} \cdot t \cdot \tilde{S} + c_{12} \cdot t \cdot \tilde{S}^2) \cdot \tilde{B} \\ &+ (c_{13} + c_{14} \cdot t + c_{15} \cdot \tilde{S} + c_{16} \cdot t \cdot \tilde{S} + c_{17} \cdot t \cdot \tilde{P}) \cdot \tilde{P} \\ &+ \text{near-wire corrections} \\ Y_1(t)) &= y_w + I_b \cdot \tan(18^\circ) \cdot (X(t) - d_r) \end{aligned} \tag{5.15}$$

The results for the fitted parameters which describe the middle region are presented in table 5.1. The average fit error $< \varepsilon >$ with $\varepsilon = (x_{s,i}(\mathbf{g}) - X_{fit,i}(t_i, \mathbf{c}))$ is plotted as function of drift distance and as function of slope in figure 5.2. These plots show that the fit converges very well. The average fit errors are very small ($\varepsilon \leq 5\,\mu$m) in the middle region between 10 mm and 46 mm. Near the sense wire plane $< \varepsilon >$ is limited to a maximum of 8 μm , and between 0.5 mm and 2 mm to 40 μm . For distances smaller than 0.25 mm the error increases rapidly up to above 100 μm . At the mesh plane the error is limited to 10 μm for distances up to 50.5 mm. For $x \geq 50.5$ mm the error increases to about 50 μm . Beyond 51.5 mm the error grows very rapidly to about 150 μm . These results show that, using method I, the data for which $x \leq 0.25$ mm or $x \geq 51.5$ mm should be rejected from the data. It is very unlikely that many hits of a given track will lay in these two regions, implying that the loss in statistics will be very limited.

	parameter value	fit-error		parameter value	fit-error
c_1	-0.6825	0.0012	$c_{10} \cdot \tilde{S}\tilde{B}$	0.5914	0.032
$c_2 \cdot t$	48.291	0.002	$c_{11} \cdot \tilde{S}\tilde{B}t$	-0.0069	0.00006
$c_3 \cdot \tilde{S}$	-0.0183	0.0025	$c_{12} \cdot \tilde{S}^2\tilde{B}t$	-0.0005	0.00006
$c_4 \cdot \tilde{S}^2$	0.6440	0.0038	$c_{13} \cdot \tilde{P}$	-0.4793	0.057
$c_5 \cdot \tilde{S}^3$	0.0253	0.0027	$c_{14} \cdot \tilde{P}t$	0.0122	0.0003
$c_6 \cdot \tilde{S}^4$	-0.1490	0.0045	$c_{15} \cdot \tilde{S}\tilde{P}$	0.3768	0.1
c_7	-0.0011	0.00006	$c_{16} \cdot \tilde{S}\tilde{P}t$	0.0016	0.0002
$c_8 \cdot \tilde{B}$	0.3684	0.019	$c_{17} \cdot \tilde{P}^2t$	0.3029	0.014
$c_9 \cdot \tilde{B}t$	-0.0045	0.00004			

Table 5.1: Fitted parameters for the Monte Carlo data and for the testbeam data using method I.

5.6 Method II: variable drift angle

In this section the results of fits using method II are presented. Contrary to method I, this method includes a drift angle that varies with pressure and temperature. Since the drift angle parameters α_o and α_1 defined in equation 4.10 contribute nonlinearly to the silicon strip point x_{si}, the fit to these two parameters is incorporated into the fit problem 5.12 in a manner analogous to the fit to the geometry parameters. This work was carried out at a later stage, and was done in several steps. The cell is divided in three regions: the near-sense region ($x \leq 12$ mm), the middle region (12 mm $\leq$ 46 mm) and the near-mesh region ($x \geq 46$ mm). First a fit was made to the geometry parameters, the drift angle parameters and the 11 parameters that describe the middle region of the cell (see equation 4.11). Only data in the middle region of the cell were accepted. The geometry

and cellmap parameters and the corresponding error matrices are discussed in section 5.6.1. The average fit error $< \varepsilon >=< (x_{s,i}(\mathbf{g}) - X_{fit,i}(t_i, \mathbf{c})) >$ of this fit suggests near-wire corrections of exactly the form presented in section 4.2.5. The second fit described included all the near-wire corrections discussed in section 4.2.5. In total 37 parameters were fitted simultaneously. These results are presented in section 5.6.2. The resulting function gives good results with $< \varepsilon > \leq 15\,\mu$m for the range of $2\,\text{mm} \leq x \leq 48\,\text{mm}$. Finally, it was attempted to remove as many as possible of the near-wire corrections without losing too much of the accuracy. Results of different test are presented in section 5.6.3.

The interpretation of the results and a discussion on the applicability of the cellmap functions to the real L3 muon chambers is the subject of section 5.9. It is shown that the fit error of individual runs is sometimes large, although the fit error averaged over all the runs at different pressure and magnetic field settings is small. It is argued that this is partly due to the limited accuracy of the testbeam data, and partly to systematic errors in the fitted cellmap function parameters. The results can be improved by "refitting" some of the parameters for individual runs. This will be the typical situation at L3: one will not be able to fit as many parameters as was possible with the testbeam setup. Most of the parameters found at the testbeam have to be taken "as they are". Some parameters have to be determined from cosmic rays or highly energetic muons in the L3 data. In section 5.9 a scheme is introduced which can be used to fit a few parameters in the L3 muon chambers.

5.6.1 Method II without near-wire corrections

Equation 4.11 for method II as presented in section 4.2 is rewritten in the general form:

$$\begin{aligned} X_2(t) &= c_1 + (c_2 + c_3\tilde{P} + c_4\tilde{P}^2 + c_5.\tilde{B}).t + c_6.\tilde{S} + c_7.\tilde{S}^2 + c_8.\tilde{S}^3 + c_9.\tilde{S}^4 + c_{10}.\tilde{P} + c_{11}.\tilde{B} \\ Y_2(t) &= y_w + I_b.(X(t) - d_r).(\alpha_o.B + \alpha_1.\tilde{P}) \end{aligned} \tag{5.16}$$

First consider a fit to data for which $10\,\text{mm} \leq x \leq 44\,\text{mm}$. Since the near-wire corrections take effect only for $x \leq 10\,\text{mm}$ and for $x \geq 45\,\text{mm}$ the near-wire corrections are not included in this fit. In total 7 iterations were needed before all the parameters converged. First the geometry parameters resulting from this fit are discussed. Since the resolution of the chamber is best in the region selected in this fit, the data can be considered more accurate than the data near the wire planes: the errors in the geometry parameters fitted from these data will be smaller than those in the parameters fitted to all the data that include data very close to the wire planes.

Geometry parameters

The geometry parameters are determined simultaneously with the cellmap param-

eters. The geometry parameters, together with the estimated values from preliminary surveys and design drawings are tabulated in table 5.2. The (simplified) correlation matrix is presented in table 5.3. Only the correlation between the geometry parameters is shown. The correlation between any of the geometry parameters and any of the cellmap parameters was found to be smaller than 0.1. This shows that the applied method to fit both geometry parameters and cellmap parameters simultaneously from the same data is valid and works satisfactorily. The length of the rotation arm, which was specified by

index-number	geometry 1 parameters	fit errors	estimated values
T_o	-21.4059	0.0008	-
T_r	9.23	0.03	-
L_r	434.34	0.03	434.40 mm
x_o	25.68	0.07	25 mm
y_o	-0.22	0.01	0 mm
ψ	-0.18251	0.00007	-0.1833 (= $10^0 30'$)

Table 5.2: Geometry parameters determined from fit compared with expected values.

ETH-Zürich, is accurately reproduced by the fit. The fixed angle ψ of the table was estimated by the CERN-SPS survey group and set to $10°30'$ with respect to the beam axis: this number is also close to the number found in the the fit. The rotation point (x_o, y_o) depends on the test chamber. The chamber was designed to have the rotation point in the middle of the chamber, thus x=25 mm and y=0 mm. No means were available to relate the actual wire plane positions inside the torsion box to a reference on the outside. The differences between the estimated and fitted values of x_o and y_o are therefore quite acceptable. Some of the correlation coefficients are relatively large (0.9). The coupling

	T_o	T_r	L_r	x_o	y_o	ψ
T_o	1	-.3	0	-.6	-.6	.4
T_r	-.3	1	0	0	.1	-.9
L_r	0	0	1	0	0	.1
x_o	-.6	0	0	1	.9	0
y_o	-.6	.1	0	.9	1	0
ψ	.4	-.9	.1	0	0	1

Table 5.3: Correlation between the geometry parameters

between T_r (the rotation readout offset) and ψ (the fixed table rotation offset) is easily understood: it is clear that a change in T_r can be compensated with a corresponding change in ψ (see figure 4.1. A change in the translation offset T_o results in a change in the rotation center (x_o, y_o) that can at least partly be compensated by corresponding changes in x_o and y_o. All the other geometry parameters are well defined. For the cellmap function $X(t)$ the actual value of the geometry parameters is unimportant. The only thing

that matters for the cellmap fit is that the fitted geometry parameters result in a valid coordinate transformation. If some of the geometry parameters are strongly correlated, as is the case in the used geometry description, the same coordinate transformation can be described by a different set of these parameters (for instance, a larger rotation offset, and smaller ψ).

Cellmap parameters.

The fit is performed to all the collected data for which $10\,\text{mm} \leq x \leq 44\,\text{mm}$. Only the parameters that describe the behaviour of the drift time - drift distance relation in the middle region of the drift cell ($10\,\text{mm} \leq x \leq 44\,\text{mm}$) are fitted. The parameters and their errors are tabulated in table 5.4. To indicate the significance of each parameter in the cellmap function, the maximum contribution to $X_{fit}(\mathbf{c})$ of the term $c_k \cdot T_k$ is also included in this table.

para-meter	fitted value	fit errors	max cont.
c_1	-0.686	0.002	0.69
c_2	48.283	0.003	48.28
c_3	0.0140	0.0003	0.42
c_4	0.39	0.01	0.35
c_5	-0.00434	0.00007	0.20
c_6	0.016	0.003	0.016
c_7	0.676	0.006	0.68
c_8	0.014	0.004	0.014
c_9	-0.180	0.007	0.18
c_{10}	-0.45	0.13	0.01
c_{11}	0.31	0.04	0.01

Table 5.4: Fitted parameters of method II. Only data in the middle region with $10\,\text{mm} \leq x \leq 44\,\text{mm}$ were used in the fits.

The fit error $< \varepsilon >=< x_{si} - X_{fit} >$ averaged over all slopes is presented in figure 5.3. The error is plotted versus the drift distance $D = |x_{si} - x_w|$ calculated from the silicon strip data. Here x_{si} is the point calculated from the silicon strips and x_w the x-coordinate of the wire. The fit error in the middle region ($10\,\text{mm} \leq x \leq 44\,\text{mm}$) is very small (figure 5.3(d)), which suggests that the 11 parameters used for this region are enough to describe the drift time - drift distance relation accurately. Close to the sense wire the fit error increases quadratically. Figure 5.3 (d) shows that the cellmap function extends up to 52 mm, beyond the mesh plane. This effect is caused by slanted tracks. Without any additional near mesh-plane corrections the errors in this region become unacceptable large. In figure 5.4 the fit error is plotted versus the slope S averaged for different drift distances, which shows the quality of the slope corrections (c_6, c_7, c_8 and c_9). Again, in the middle region of the cell the errors are small (figure 5.4(b)). Closer to the wire planes (figures 5.4(a)), the error increases again, to errors up to 300 μm for

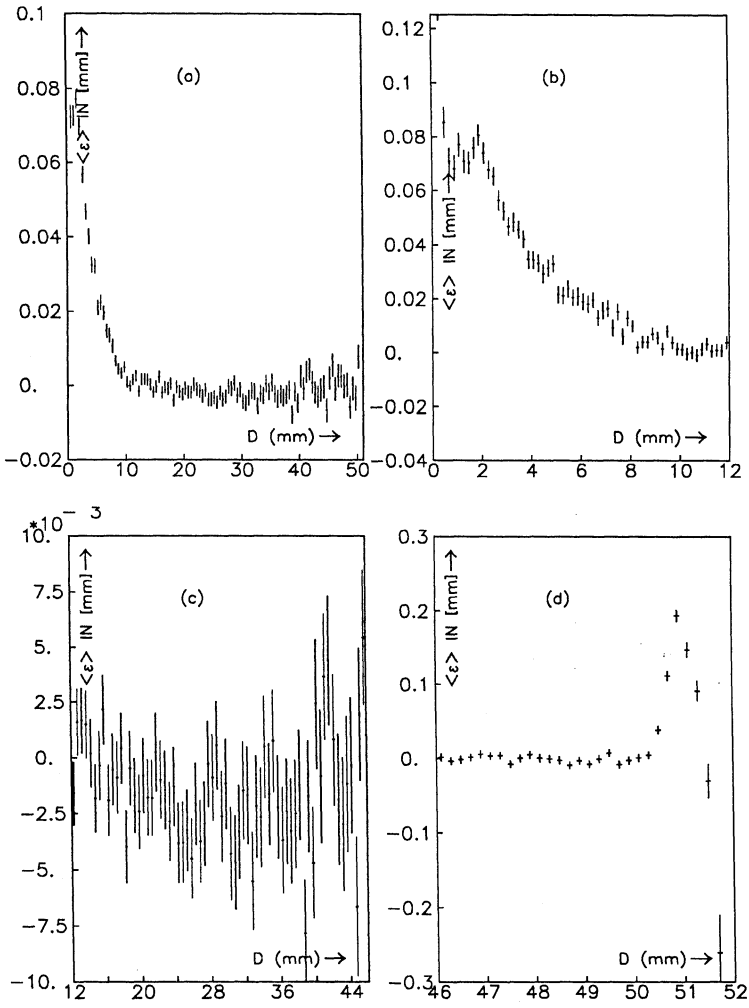

Figure 5.3: Average fit error $< \varepsilon >=< x_{si} - X_{fit} >$ as function of drift distance for the whole cell (a), near the sense plane (b), the middle region (c) and near the mesh plane (d). Only the parameters in the middle region are fitted. All data were fitted in the histograms to show the need of near-wire corrections.

large slopes and distances $x < 2$ mm. The shape of the error curves in these plots and in figure 5.3 (b),(d) suggest that additional corrections are needed. 4.2.5.

	c_1	c_2	c_3	c_4	c_5	c_6	c_7	c_8	c_9	c_{10}	c_{11}
c_1	1	-.9	-.3	0	-.2	.2	-.3	0 .	.2	.6	.2
c_2	-.9	1	.5	.1	.3	-.2	0	0	0	-.6	-.2
c_3	-.3	.5	.1	.8	0	-.1	0	0	0	-.6	0
c_4	0	.1	.8	1	0	0	0	0	0	0	0
c_5	-.2	.3	0	0	1	0	0	0	0	.1	-.9
c_6	.2	-.2	-.1	0	0	1	.3	-.7	-.3	.2	0
c_7	-.3	0	0	0	0	.3	1	-.3	-.9	0	0
c_8	0	0	0	0	0	-.7	-.3	1	.3	-.1	0
c_9	.2	0	0	0	0	-.3	-.9	.3	1	0	0
c_{10}	.6	-.6	-.6	0	.1	.2	0	-.1	0	1	-.1
c_{11}	.2	-.2	0	0	-.9	0	0	0	0	-.1	1

Table 5.5: Correlation between the "middle region" parameters

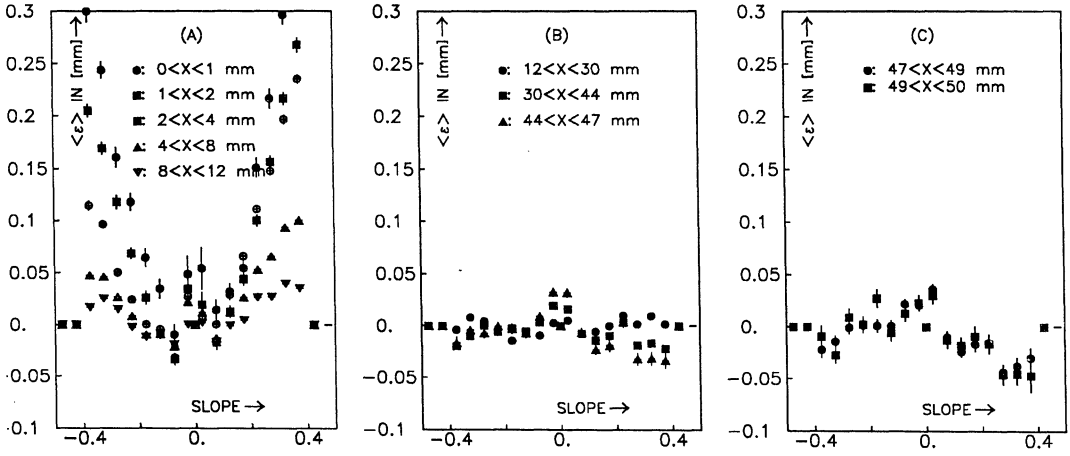

Figure 5.4: Average fit error $< \varepsilon >=< x_s - X_{fit,i}(t_i, \mathbf{c}) >$ as function of slope for different regions of the drift distance D: In the left figure for the near sense region ($x < 12$ mm), in the middle plot for the middle region ($12\,\text{mm} < x < 47$ mm) and in the right plot for the near mesh region ($x \geq 47$ mm).

Table 5.5 shows the correlation between the 11 middle region parameters. The main correlation is between the offset and the drift velocity $\rho(1,2)$, between the two pressure corrections in the drift velocity $\rho(3,4)$, the two magnetic field corrections $\rho(5,11)$ and between the odd and even slope corrections , $\rho(6,8)$ and $\rho(7,9)$ respectively. All these correlations are reasonable and do not suggest an overdetermined system.

Conclusions: If only 11 cellmap parameters and 2 drift angle parameters are fitted, the resulting cellmap function is accurate in the region 10 mm $\leq x \leq$ 46 mm. Additional corrections close to the wire planes are needed to extend the range in x. For very small

slopes the error is slightly larger due to induced charge effects. Special attention is needed to tune the cellmap function for small slopes. This effect can not be treated with the currently used polynomial slope corrections.

5.6.2 Method II including all the near-wire corrections

The fit described in this section is a fit to method II, but this time with all the near-wire corrections that were described in section 4.2.5. The total function now becomes:

$$\begin{aligned} X_2(t) &= c_1 + (c_2 + c_3\tilde{P} + c_4\tilde{P}^2 + c_5.\tilde{B}).t + c_6.\tilde{S} + c_7.\tilde{S}^2 + c_8.\tilde{S}^3 + c_9.\tilde{S}^4 + c_{10}.\tilde{P} + c_{11}.\tilde{B} \\ &+ \text{near-wire plane corrections} \\ Y_2(t) &= y_w + I_b.(X(t) - d_\tau).(\alpha_o.B + \alpha_1.\tilde{P}) \end{aligned} \tag{5.17}$$

The near-wire correction parameters were defined in section 4.2.5. The numbering of the parameters is as follows:

$$\begin{aligned} F_{10}(\tilde{S}) &= c_{12} + c_{13}.\tilde{S} + c_{14}.\tilde{S}^2 + c_{15}.\tilde{S}^3 \\ F_6(\tilde{S}) &= c_{16} + c_{17}.\tilde{S} + c_{18}.\tilde{S}^2 + c_{19}.\tilde{S}^3 \\ F_3(\tilde{S}) &= c_{20} + c_{21}.\tilde{S} + c_{22}.\tilde{S}^2 + c_{23}.\tilde{S}^3 \\ F_{45}(\tilde{S}) &= c_{24} + c_{25}.\tilde{S}^2 \\ F_{48}(\tilde{S}) &= c_{26} \\ F_{50}(\tilde{S}) &= c_{27} \end{aligned} \tag{5.18}$$

Detailed tests on the stability of the near wire corrections [45] showed that near wire correction near the mesh plane for $x \geq 51$ mm could cause instabilities. Each time the correction was calculated the resulting point was further away from the stable solution defined in equation 4.16. The rms fit error $< \varepsilon >=< x_s - X_{fit,i}(t_i, \mathbf{c}) >$ as function of distance is shown in figure 5.5. Note that the errors in the regions $0 \leq x \leq 12$ mm and $x \geq 50.7$ mm are significantly smaller than those presented in figure 5.3. The near sense wire region can now be reduced to a distance of 2 mm from the sense wire. For distances $x \leq 2$ mm the error increases again. The second region with large fit errors is very close to, and beyond the mesh plane. Data for which $x \geq 50.7$ mm should be dropped from the fit. The rms error as function of slope is presented in figure 5.6. For all the figures the calculated rms error $< \varepsilon >$ is less than 25 μm , except for very large slopes and short drift distances. The single wire resolution as function of distance and slope is presented in figure 5.7. The solid curve corresponds to the resolution calculated with the resolution function presented in equation 5.13, each time averaged over the other parameter. As stated before, the numerical values for the parameters used in $\sigma^2(x, S)$ in equation 5.13 were calculated from results of method I fits. The curves in figure 5.7 show that the resolution is not sensitive to the chosen parametrisation of the cellmap function $X(t)$, which agrees with the statement made in section 5.4.1. Note that the function

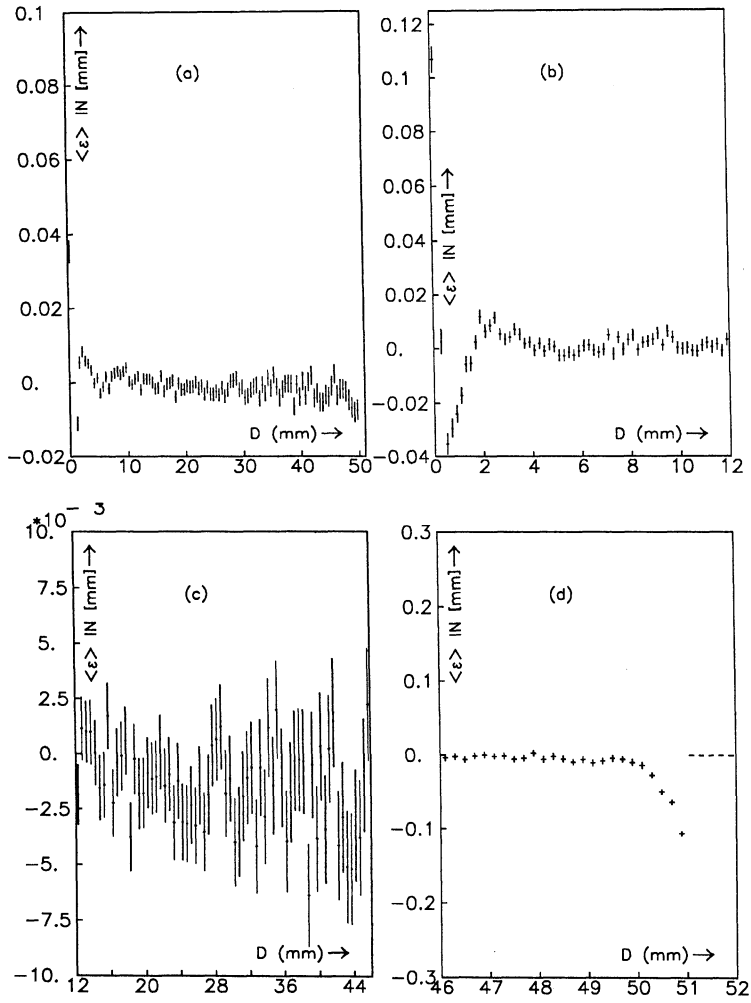

Figure 5.5: Same errors as in figure 5.3, but now for cellmap function including all the near-wire corrections specified in chapter 4.

$\sigma^2(x, S)$ does not very well describe the resolution for small slopes (see figure 5.7(b)). For very small slopes, induced charge effects play an important role and these were not incorporated in the cellmap function. For parallel tracks all the signals arrive almost at the same time. The induced charge of the neighbouring sense wires where the avalanche arrived just a little earlier affects the timing, which results in a small error. This effect

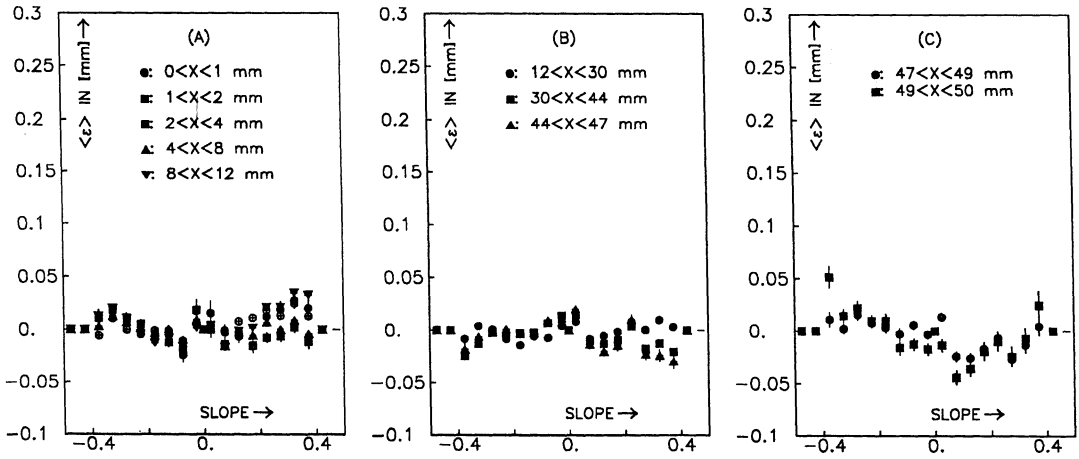

Figure 5.6: The rms fit error $< \varepsilon >=< x_s - X_{fit,i}(t_i, \mathbf{c}) >$ versus slope for distances $x \leq 12$ mm in (a), for distances 12 mm $\leq x \leq 47$ mm in figure (b) and for distances $x > 47$ mm in (c).

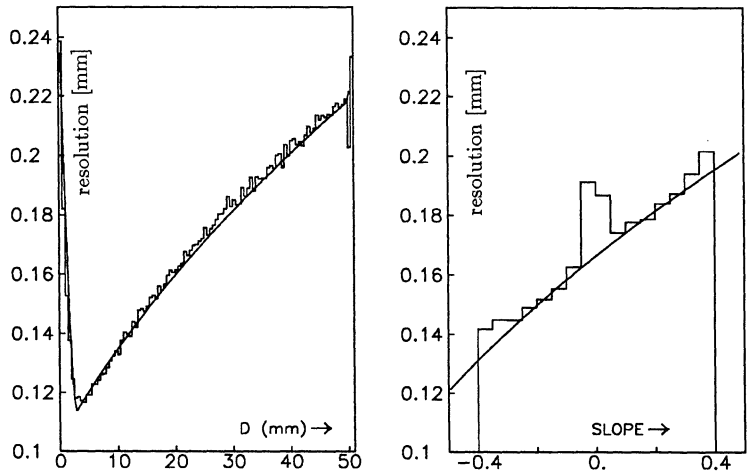

Figure 5.7: Single wire resolution vs distance (a) and vs slope (b)

is understood and has been described theoretically [43][44] [16]. Because there are no terms in the cellmap function to fit the small slope effect, this effect is absorbed in the fit error and in the resolution. If the cellmap function is modified to include some "small slope" corrections, the resolution for small slopes should improve.

parameter	one loop	six loops	fit error	parameter	one loop	six loops	fit error
c_1	-0.685	-0.685	0.001	$c_{18}(F_6)$	0.27	0.27	0.04
$c_2 t$	48.297	48.297	0.002	$c_{19}(F_6)$	-0.06	-0.05	0.07
$c_3 \tilde{P} t$	0.0106	0.0106	0.0003	$c_{20}(F_3)$	0.0037	0.0036	0.01
$c_4 \tilde{P}^2 t$	0.23	0.23	0.01	$c_{21}(F_3)$	-0.05	-0.04	0.04
$c_5 \tilde{B} t$	-0.00438	-0.00438	0.00003	$c_{22}(F_3)$	-0.151	-0.151	0.031
$c_6 \tilde{S}$	0.011	0.010	0.002	$c_{23}(F_3)$	0.06	0.05	0.06
$c_7 \tilde{S}^2$	0.644	0.645	0.004				
$c_8 \tilde{S}^3$	0.023	0.022	0.003	$c_{24}(F_{45})$	-0.050	-0.020	0.007
$c_9 \tilde{S}^4$	-0.149	-0.149	0.004	$c_{25}(F_{45})$	0.184	0.136	0.007
$c_{10} \tilde{P}$	-0.50	-0.50	0.06	$c_{26}(F_{48})$	-0.02	-0.12	0.02
$c_{11} \tilde{B}$	0.31	0.31	0.02	$c_{27}(F_{50})$	-0.74	0.16	0.04
$c_{12}(F_{10})$	0.062	0.063	0.008				
$c_{13}(F_{10})$	-0.25	-0.25	0.02	α_1	13.299	13.299	0.006
$c_{14}(F_{10})$	-0.63	-0.63	0.02	α_2	-0.114	-0.116	0.008
$c_{15}(F_{10})$	-0.027	-0.027	0.036	c_{37}	-0.031	-0.031	0.002
$c_{16}(F_6)$	-0.014	-0.014	0.016				
$c_{17}(F_6)$	0.29	0.29	0.05				

Table 5.6: Fitted parameters of method II including near-wire corrections. Both the results for one iteration and 6 iterations in the near-wire correction calculation are presented. For almost all the parameters the difference between the parameters is smaller than the fit error. Note that c_2 and c_{37} are given in μm /ns.

As discussed in section 4.2.5 the near-wire correction should be iterated in order to be able to calculate the exact inverse function for the Monte Carlo method. To test the dependence of the cellmap parameters on the number of iterations, two fits were performed. The first fit, called "one loop fit", calculated the near-wire corrections once, and did not loop through the corrections. For the second fit, called "six loop fit", the near-wire correction loop was iterated 6 times. The two fits gave comparable results. The cellmap parameters from both fits and the fit errors are tabulated in table 5.6. To compare the effect of the number of iterations on the cellmap function, the difference between X^1_{fit} calculated with the one-loop parameters and X^6_{fit} calculated with the six-loop parameters is shown in figure 5.8(a). Only in the near-wire region and for large slopes the differences are significant. But if, again, the data for which $x \leq 2$ mm are not accepted for the fit, the differences between X^1_{fit} and X^6_{fit} are limited to only a few microns. For comparison, figure 5.8(b) shows the difference between X^1_{fit} and X^6_{fit} but now calculated with the same parameters as used in X^1_{fit}. These results justify a fit to the near-wire correction parameters without looping through the corrections. From figures 5.3(b) and 5.5(b) it is clear that the near-wire corrections are needed to extend the range where the chamber gives accurate results down to 2 mm at the sense wires. For $x \leq 2$ mm the error increases, but a 40 μm error is still acceptable compared with

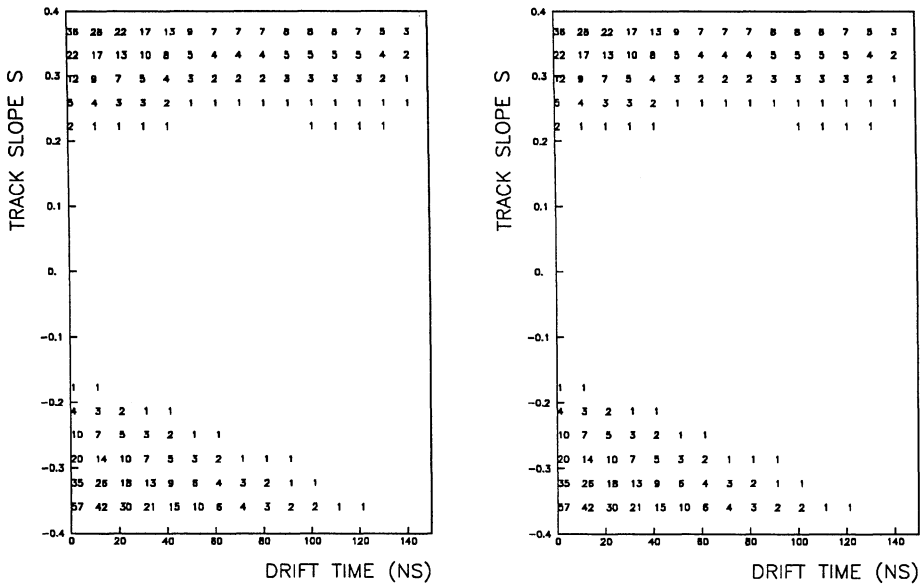

Figure 5.8: Difference in the near sense region between the "one-loop" and the "six-loop" cellmap functions. The numbers in the plots are the difference in μm

the single wire resolution in this region. For $x \leq 0.5\,\mathrm{mm}$ the error is too large. Data in this small range should be excluded from the fit.

5.6.3 Method II with simplified near-wire corrections

In the cellmap function discussed sofar the errors in the near-wire regions were reduced by introducing a relatively large number of additional parameters: 12 parameters for the near-sense and 6 for the near-mesh plane, compared to only 11 parameters for the middle region. This large number of near wire corrections can be reduced at the cost of a small increase of the accuracy of the segment. In this section the results from a fit with only a few near-wire corrections are presented. The near-wire correction functions now are (see also equation 5.18):

$$\begin{aligned} F_{10}(\tilde{S}) &= c_{12} + c_{13} \cdot \tilde{S}^2 + c_{14} \cdot \tilde{S}^4 \\ F_{45}(\tilde{S}) &= c_{15} + c_{16} \cdot \tilde{S}^2 \end{aligned} \tag{5.19}$$

The choice for only even terms in $\tilde{S}$ is suggested by figure 5.4, where the fit error $< \varepsilon >$ was plotted versus the track slope. The odd terms in $\tilde{S}$ should be small, and are ignored

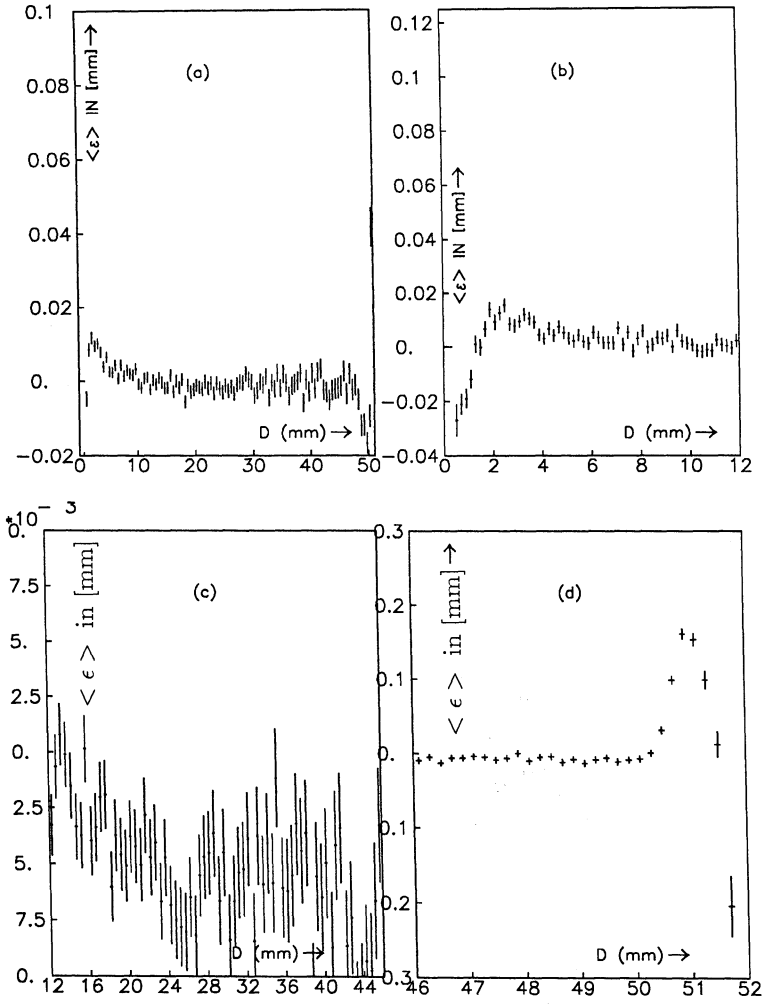

Figure 5.9: Average fit error $< \varepsilon >=< x_{si} - X_{fit} >$ as function of drift distance for the whole cell (a), near the sense plane (b), the middle region (c) and near the mesh plane (d).

in the current model. The fit converged within 7 iterations. The 11 cellmap parameters in the middle region are not significantly different from the numbers tabulated in table 5.6. The values for the five near-wire correction constants are given in table 5.7. The average fit error $< \varepsilon >$ versus distance and slope is shown in figures 5.9 and 5.10. The

parameter	value	fit error
$c_{12}(F_{10})$	0.069	0.003
$c_{13}(F_{10})$	-0.44	0.01
$c_{14}(F_{10})$	-0.489	0.008
$c_{15}(F_{45})$	-0.07	0.01
$c_{16}(F_{45})$	-0.058	0.005

Table 5.7: The near-wire parameters and their errors for the simplified cellmap function.

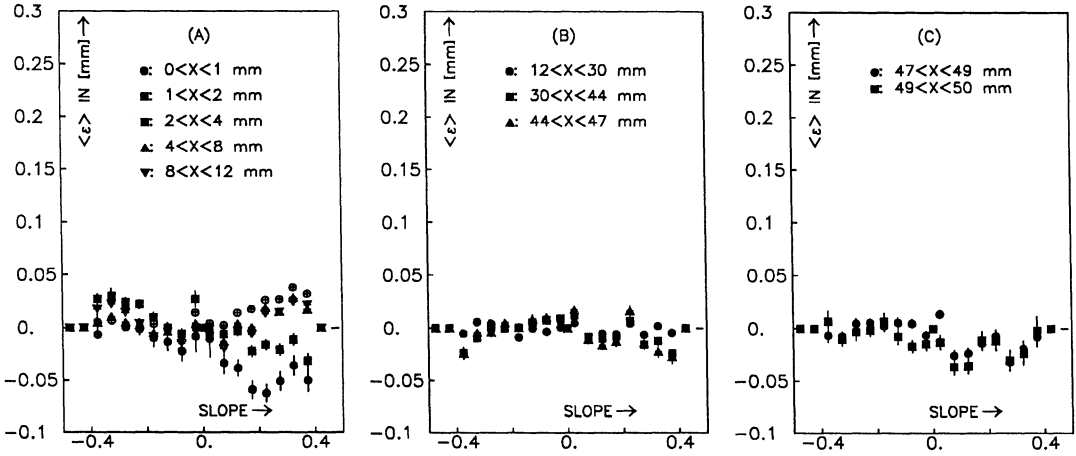

Figure 5.10: Rms fit error $< \varepsilon >=< x_s - X_{fit,i}(t_i, \mathbf{c}) >$ versus slope for distances $x \leq 12$ mm in (a), for distances 12 mm $\leq x \leq 47$ mm in figure (b) and for distances $x > 47$ mm in (c), corresponding to the simplified cellmap function with only a few near wire corrections.

fit errors near the sense plane are very acceptable, especially for $x \leq 2$ mm where the fit errors are within 20 μm : the previous fits showed errors up to 40 μm in this region. The average fit error in the middle region is very small, and near the mesh plane acceptable up to $x \leq 50.5$ mm. For very large x the errors increase too much. If one is willing to reject all the data for which $x \leq 0.5$ mm or $x \geq 50.5$ mm, this simplified function works satisfactorily. The single wire resolution that corresponds with this function is shown in figure 5.11, together with the curve calculated from equation 5.13. These curves are very similar to the results presented in figure 5.7, which once more shows that the single wire resolution is independent of the precise cellmap parametrisation.

Conclusions: In this section a cellmap function with a simplified near-wire correction scheme has been presented. The near-wire fit errors compare well with the near-wire fit

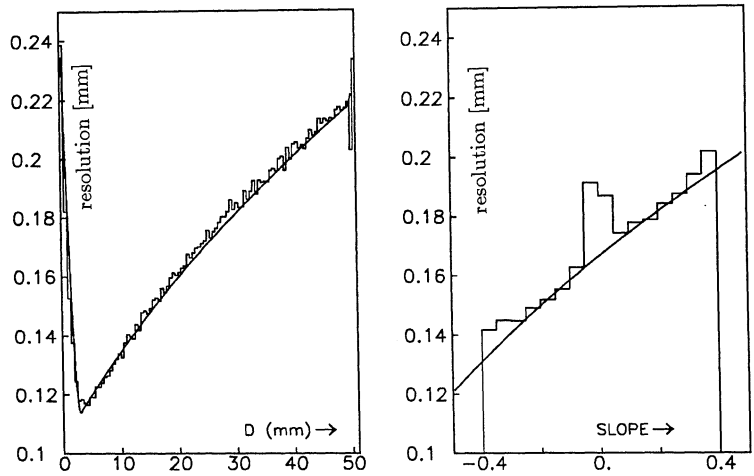

Figure 5.11: single wire resolution vs distance (a) and vs slope (b)

errors found in section 5.6.2, with slightly larger errors for 2 mm $\leq x \leq$ 10 mm, but with smaller errors for $x \leq 2$ mm. The simplified function will be particularly useful in the early phases of the experiment, when slightly larger systematic errors are acceptable.

5.7 Single wire resolution and accuracy

The fit residuals as function of drift distance and track slope were collected to calculate the single wire resolution $\sigma_w(x, \tilde{S})$. The resolution curves for different fits have been presented in figures 5.7 and 5.11. Although the resolution plays an important role in the accuracy of the muon chambers, its importance is in general overestimated. A high resolution is only useful if the systematic errors in the cellmap function are smaller than, or at most comparable to, the effect of the resolution. The actual resolution depends, among others, on the applied data selection criterion. Two methods have been in use which will be compared below. It is shown that the smallest possible resolution does not always imply the most accurate results on the centroid point.

The conventional data selection criterion is the three standard deviations cut (3σ): after a first fit has been made, all data points more than 3σ from the average value are rejected. This method is based on the assumption that the data are normally distributed around the average value. If the data are not normally distributed, too many or too few data are rejected. The alternative data selection criterion is based on the assumption that the data are not normally distributed around the average value. If this assumption is true, one always improves the results by throwing away a fixed fraction of the data

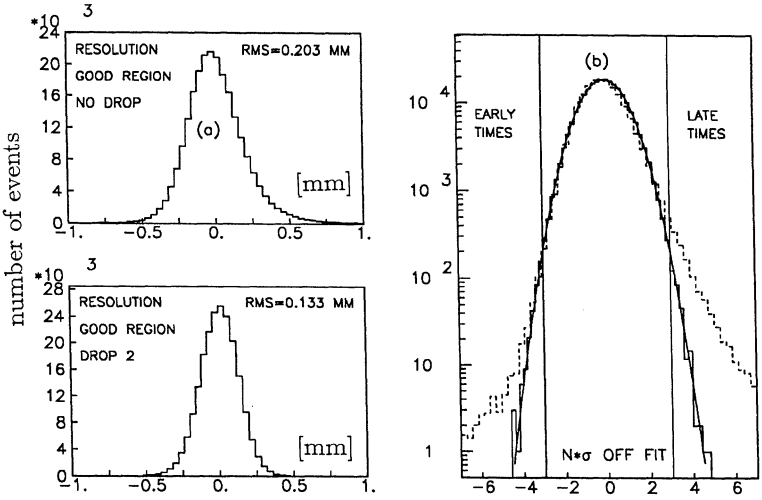

Figure 5.12: Resolution for data in the middle region (10 mm $\leq x \leq$ 46 mm): in figure (a) all data are accepted, in (b) the same curve but with a logarithmic vertical scale, and in (c) after removing the two worst data points from the fit ($\approx$ 10%).

(the part that is worst compared to the average value). This corresponds with cutting away the "tails" of the distribution.

To show which of the two critiria is best in the case of the L3 muon chamber track segment fits, the "3σ" criterion or the "fixed fraction" criterion, the shape of the resolution function and the centroid error were studied in detail. In figure 5.12(a) the rms resolution of the fit is shown: in figure (a) for all the data ($\sigma = 203\,\mu$m), and in figure (c) for the case 10% of the data is rejected (fixed fraction thrown out), which results in $\sigma = 133\,\mu$m . Only data for which 10 mm $\leq x \leq$ 46 mm are used in the histograms. In figure (b) the first resolution curve is plotted again, but now with a logarithmic vertical scale. The corresponding normal distribution with the same σ as found from the data is shown as a parabola. From this figure it is evident that the tail is small. Only with this logarithmic scale the tail shows clearly as a deviation of the data curve (dotted line) from the parabola. The distribution is almost "normal" up to 3σ. If the 3σ criterion is applied, the tail will be cut off without loss of good data. If the fixed (10%) fraction criterion is applied, a significant fraction of good data is thrown out, together with the tail. If good data is thrown away, the centroid error will increase, because this error is proportional to $1/\sqrt{n}$, where n is the number of wires included in the fit [13]. This effect is shown in figure 5.13, where the rms of the centroid error is plotted versus the number of sigmas applied as cut. The rms value is smallest around 3σ, both for method II with all near wire corrections included (solid line) and for method II with only 6 near wire

corrections (dotted curve). This implies that the 3σ cut should be favoured above the fixed fraction cut.

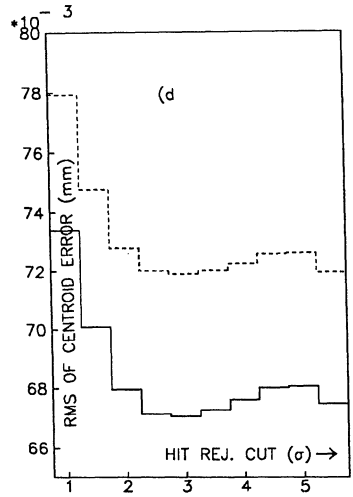

Figure 5.13: The rms of the error in the centroid point of the track segment versus the number of standard deviations used as data selection criterion for method II with all near wire corrections (solid line) and for method II with simplified near wire corrections (dotted line). If too few data are thrown away, the tails will influence the results (to the right in the figure). If the cut is too tight, good data will be lost which deteriorates the result (to the left in the figure).

5.8 Estimate of systematic errors

As was shown in the previous sections fits to method I and method II cellmap functions both give good results. In this section the systematic errors are discussed. Two methods to estimate the systematic error have been applied. The first method uses a statistical argument, the second method compares fit errors of individual runs. It is shown in the following sections that the fit errors of individual runs can be reduced significantly by "hand tuning" only a few parameters, namely the offset c_1 and the drift velocity c_2. This will be the typical situation for L3: it is very unlikely that a cellmap function found with a small model chamber at a testbeam will be perfect for all the muon chambers (MI,MM and MO) for the entire lifetime of the experiment. Small contaminations of the gas or unaccounted errors in the temperature, pressure or magnetic field will introduce systematic errors. At the end of this section a method to detect and remove these errors

from the L3 cellmap function is outlined. With this method it should be possible to keep the systematic errors in the cellmap function below an acceptable level.

5.8.1 Statistical estimate of systematic errors

The first method to estimate the systematic errors in the fit is based on a statistical argument. Consider the average fit error $< \varepsilon >$ introduced in section 5.5. Both the systematic and the statistical fit errors contribute to ε. If one assumes that the statistical and the systematic errors add quadratically, a first estimate of "the systematic error" is given by:

$$\sigma_{sys} \approx \sqrt{\sum_i (\varepsilon_i^2 - \sigma_{stat,i}^2)} \tag{5.20}$$

If this formula is applied to the fits then a systematic error of $\approx$ 25 - 30 μm is found for both method I and method II. This number is not very sensitive to the number of near-wire corrections included in the fit (for instance, method II with only 4 near sense wire and 2 near mesh wire corrections resulted in $\sigma_{sys} = 27$ micrometer, and method II including all 12 near sense and 4 near mesh plane corrections yielded $\sigma_{sys} = 26\,\mu$m). Compared to the limit of 10 μm for individual systematic errors, defined in section 1.3, this number looks too large, but the interpretation of this number is difficult: it is not obvious what the effect of the above calculated number is on the accuracy of the results. In the following subsection some of the systematic effects found in the data of individual runs are discussed.

5.8.2 Systematic errors from individual runs

In this section a second method to estimate the systematic effects is presented, by looking at individual runs containing data at only one pressure and magnetic field setting. In figures 5.14(a) the rms fit error $< x_s - X_{fit} >$ is shown for a run with "large systematic errors" (testbeam run 226), and in 5.14(b) for a run which has smaller systematic errors (run 262). These plots were produced using the method II cellmap function with the simplified near wire corrections introduced in section 5.6.3. Run 226 has the largest systematic errors of all runs accepted in the analysis. Similar effects are found if all the runs in a specific range of P and B are considered. The data were subdivided in nine B-P bins, (low, medium and high B and/or P). For instance, in figure 5.14(c) the rms fit error as function of drift distance is shown for all the data for which $P \leq 755$ mmHg and $0.495 \leq B \leq 0.510$ T. This distribution shows a drift velocity error. If different ranges of B and P are selected, the fit errors are different (and smaller). For instance, in figure (d) the rms fit error is shown found in all the data for which $755 \leq P \leq 765$ mmHg and $B \leq 0.495$ T. this curve only shows the usual larger errors very close to the wire planes, and a small offset error ($\leq 7\,\mu$m). Possible causes for all these errors are:

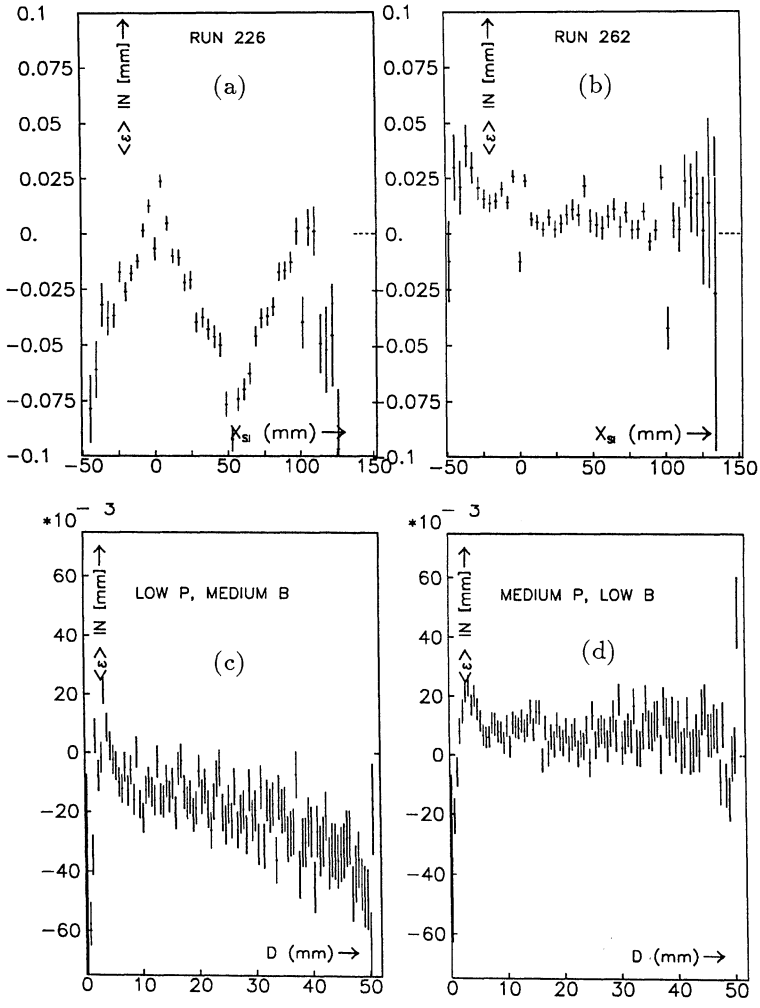

Figure 5.14: Examples of systematic errors. If only data of individual runs at a specific magnetic field and pressure setting are considered, some runs show large errors, like run 226 in figure (a), and some with small errors, like run 262 in figure (b). Similar effects are found if all the runs in one of the B-P bins are considered, as shown for two bins in figures (c),(d).

- The cellmap function is wrong and is not able to handle different pressure and magnetic field settings correctly.

- The systematic errors are caused by systematic errors in the testbeam data.

Since the B and P ranges covered by the testbeam data are small the first possibility is not very likely: small variations in B and P should be described properly by low order expansions in B and P. The second possibility, on the other hand, is more likely to be true: it is not difficult to think of possible sources of error. The pressure, temperature and magnetic field settings were read out manually once per run and the measured values were written in the logbook. These numbers were later used in the analysis of the data of the corresponding run, which, on average lasted some 30 to 45 minutes. The readings were not checked during the run. Since the error bars in figures 5.14 are small compared to the error, a drift in P, T or B is not very likely. The most likely cause for an occasional large discrepancy is a simple read-out error.

The plots collected in figure 5.14 indicate the kind of systematic errors found in the data. Limits for systematic errors in the different parameters are (method II with simplified near wire corrections):

- $|\Delta c_1| \leq 15\,\mu$m and $|\Delta c_2| = |\Delta V_x| \leq 0.075\mu$m/s$(= 0.15\%)$ for individual runs.
- $|\Delta c_1| \leq 7.5\,\mu$m and $|\Delta c_2| = |\delta V_x| \leq 0.040\mu$m/s$(= 0.08\%)$ for any of the nine $B-P$ bins.

The aim for the maximum of any systematic error was $\Delta x_{sys} \leq 10$ μm , as defined in section 1.3. With this number in mind it is clear that the systematic errors found in some of the data are too large. The drift velocity error in run 226 causes errors of up to 75 μm . In the following section it is indicated how one can reduce the systematic errors considerably by analyzing track segments that cross either a sense or a mesh plane.

5.9 Tuning parameters at L3

As stated before, it can not be expected that a cellmap function found with the test chamber will give exactly the same results for the real L3 muon chambers. Firstly because of some (small) differences between the test chamber and a real MM chamber, such as differences in signal shape, and secondly because the testbeam conditions may be slightly different from the real L3 conditions. For instance, almost all the data collected at the testbeam sofar were collected with the discriminator threshold set to 30 mV. During the octant test a level as low as 20 mV was used with lower high voltage settings This affects some of the parameters, especially the slope correction terms [40]. Another difference between the test beam and the L3 experiment is the gas composition. At the test beam pre-mixed bottles of the L3 Argon:Ethane mixture were used. L3 will have a large gas mixing system that is very likely to suffer from small, uncontrolled drifts and fluctuations. It is therefore important to have some means to check the accuracy

of the cellmap function used in L3 with real L3 data, or even to "refit" a few of the cellmap parameters. The most likely parameters to require tuning are the constant offset parameter c_1, the drift velocity parameter $V_x = c_2$, and c_5, the parameter that describes the magnetic field dependence of the drift velocity (method II). Small errors in the global time-zero and gas gain effects are absorbed by adjusting c_1. Effects on the drift velocity caused by readings errors in the pressure or temperature and the effects caused by fluctuations in the gas mixture can be corrected by adjusting c_2. Tuning c_5 may be required because the range of magnetic field values in the muon spectrometer is much larger than the range covered at the testbeam.

To fit these parameters tracks that cross a sense or a mesh plane can be selected. If the value of c_1 is not correct, this will result in a "jump" of the track at a sense plane crossing. Similar, if the drift velocity c_2 is wrong, this will result in a jump at the mesh planes. By adjusting c_1 and c_2 the discontinuities in the measurements at the wire planes can be minimized. To show the improvement that can be achieved by such a fit, figure 5.15 again shows the rms fit error $< \varepsilon >$ in run 226 versus the drift distance, but now after "tuning" the drift velocity parameter c_2. From figure 5.14(a) it was obvious that the drift velocity was wrong during run 226. This appears as a miss-match of $\approx$ 150 μm between the two subsegments at the mesh plane. Instead of actually measuring the miss-match, figure 5.14(a) was used to estimate the error in the drift velocity. In the figure the sense planes are situated at $X_{si} = 0$ mm and at $X_{si} = 101.5$ mm. The mesh plane is at $X_{si} = 50.7$ mm, where X_{si} is the position in the chamber determined by the silicon strips. Note that the offset c_1 is correct: the fit error is about 0 at the sense planes. From the error of -75 μm at the mesh plane, the drift velocity correction has been calculated. The improvement is about a factor 4 for 0 mm $\leq x \leq$ 100 mm(errors $\leq 15\,\mu$m). The optimal procedure at L3 will be the following:

- Select sense plane crossing segments for which $|z| \leq 2$ m. In this region the magnetic field can be considered constant (see chapter 2). These data could be used to optimize the value of c_1.
- Select mesh plane crossing segments in the same region and optimize the drift velocity c_2. These two steps are to be repeated until the segment mis-matches at both the sense and the mesh planes are acceptable (mis-matches at the wire planes $\leq 10\,\mu$m).
- Finally, in order to tune c_5, one can select mesh plane crossing segments for which $|z| \geq 2$ m. In this region the magnetic field starts to vary, and jumps at the mesh plane in regions with low magnetic fields can be used to optimize c_5.

It will be very difficult to tune any more parameters. Firstly, because the number of tracks will be much smaller than at the testbeam, and secondly because all errors have to be deduced from mis-matches at the wire planes.

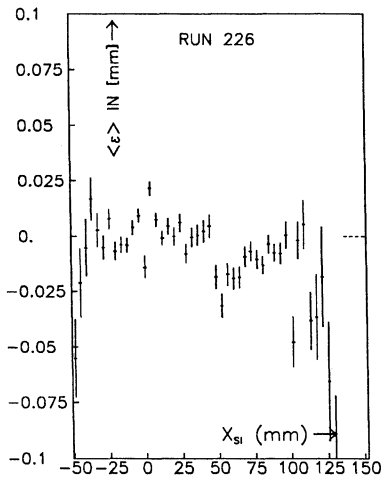

Figure 5.15: The rms fit error $< \varepsilon >$ as function of drift distance after "tuning" one of the cellmap parameters (the drift velocity c_2).

5.10 Conclusions

In this chapter the results of the L3 muon chamber testbeam experiment were presented. It was shown that the testbeam setup works satisfactorily, and that the data can be used to fit geometry parameters to describe the setup, simultaneously with a large number of cellmap parameters. Both models derived in chapter 4 were used to fit to the data with comparable results. The most important difference between the two methods is that method I assumes a constant drift angle, while method II incorporates a variable drift angle. Although the results are comparable, method II should be preferred, because the meaning of the different parameters is easier to understand. Also the magnetic field of L3 is less homogeneous than was originally expected. Therefore the assumption of a fixed drift angle is not strictly correct.

Different versions of method II have been tried. It was shown in section 5.6.1 that the near wire corrections are necessary in order to minimize systematic effects for drift distances $x \leq 12\,\text{mm}$ and $x \geq 46\,\text{mm}$. The function with a very small number of near wire corrections (introduced in section 5.6.3) results in almost the same fit errors as the function which includes all the near wire corrections introduced in chapter 4. The main difference between the two functions is the slightly worse rms (10% increase) of the centroid point in case the simple function is used (see figure 5.13 for a comparison). The simple function should therefore be favoured, at least during the startup period of L3 and in the early phase of the data analysis.

The results presented in this chapter are far from complete: there are several effects

which play an important role in the behaviour of the muon chambers that have not yet been included in the cellmap function. The most important effects are:

- Only one specific gas mixture has been used. If data is collected at different gas mixtures (different fractions of ethane and different O_2 contaminations), the cellmap function can be extended to handle effects caused by the mixture variations.
- There will be large regions in the L3 muon chambers where the B_r component of the magnetic field is significant (up to 0.1 T) and should be included in the cellmap function. The same testbeam setup described in this thesis could be applied to measure effects of B_r on the cellmap function by tilting the chamber in the support arms (this option is already available). Since the drift angle in the z direction will be very small, it should suffice to introduce one additional parameter in the drift velocity incorporate the effect of B_r on the cellmap function.
- The difference in gain between the test chamber and the real chambers should be studied. Knowledge of these differences is necessary in order to be able to use the testbeam measurements of the gas gain effects to adapt the cellmap function for small changes in the HV settings of the chambers or variations of the discriminator threshold settings.

The most important issues are the dependence on the gas composition and the B_r correction. Since it will not be possible to measure these effects accurately at L3, an additional testbeam experiment is needed.

References

[1] L3 Letter of intent, CERN (January 1982)

[2] J.J. Aubert *et al.* , " Experimental observation of a heavy particle J", Phys. Rev. Lett., 33(1974)1404.

[3] Augustin, "Discovery of a Narrow Resonance in e^+e^- annihilation", Phys. Rev. Lett. 33(1974)1406.

[4] S.W. Herb *et al.* , "Observation of a Dimuon Resonance at 9.5 GeV in 400-GeV Proton-Nucleus Collisions", Phys. Rev. Lett. 39(1977)252.

[5] G. Arnison *et al.* , "Experimental observation of lepton pairs of invariant mass around 95 Gev/c^2 at the CERN SPS collider", Phys. Lett. 126B(1983)398.

[6] P. Bagnaia *et al.* , "Evidence for $Z^o \rightarrow e^+e^-$ at the CERN $\bar{p}p$ Collider", Phys. Lett. 129(1983)130.

[7] "The construction of L3", CERN (April 1985)

[8] H.Anderhub *et al.* "Operating experience with the MARK-J time expansion chamber" NIM A265(1988)50

[9] B. Bleichert *et al.* , "Test results from a uranium hadron calorimeter using wire chamber readout", NIM A254 (1987) 529

[10] J.A.Bakken *et al.* "Ionization loss in BGO", NIM A270(1988)397

[11] V. Innocente, CERN, private communication. Results derived from prelimminary Monte Carlo studies. Muons with energy losses $\geq$ 10 GeV/c were removed from the analysis.

[12] B.Adeva *et al.* , "Muon detection in the L3 experiment at LEP", NIM A277(1989)187

[13] P.Duinker *et al.* , "Space resolution of a drift chamber with multiwire sampling", NIM 201 (1982) 251.

[14] P. Duinker *et al.* , "Some methods and tools for testing and optimizing proportional wire chambers", NIM A273 (1988) 814.

[15] Yue Peng, "The muon spectrometer of the L3 detector at LEP", thesis, Univ. of Amsterdam (1988)

[16] D. Antreasyan *et al.* , "The L3 high-resolution muon drift chambers: systematic errors in track postion measurements". NIM A252 (1986) 304.

[17] P. Seiler *et al.* , L3 Muon Chamber Group, ETH Internal Note 85-4, 1985.

[18] F. Hartje *et al.* , "Straight line calibration in drift chambers over eight meters". NIM A269(1988)544.

[19] L3 Technical Proposal to CERN-LEPC (May 1983)

[20] R. Veenhof, "Garfield, a drift-chamber simulatin program". CERN-HELIOS internal note. (1988)

[21] F. Sauli, "Principles of operation of multiwire proportional and drift chambers". CERN, 1977.

[22] F. Hartjes *et al.* , "Electron drift velocity close to a sense wire", submitted to NIM for publication.

[23] A. Peisert, F. Sauli. "Drift and Diffusion of electrons in gases: a compilation". CERN, 1984.

[24] M. Hauschild *et al.* , "The OPAL Jet Chamber Group". (Vienna wire chamber conference 1989, to be published).

[25] D.J. Schotanus. "Magnetic field calculations for the L3 detector using the program POISSON", Univ. of Nijmegen, HEN 283

[26] R. Holsinger and C.Iselin, "The program POISSON". CERN program library no T604.

[27] J.Simkin and C.W.Trowbridge, "Three dimensional computer program (TOSCA) for non-linear electromagnetic fields". Rutherford Laboratory Rl 79-097

[28] F.J.G.H. Crijns, Univ. of Nijmegen, private communication.

[29] F.J.G.H. Crijns. "The L3 magnetic fieldmap" (Univ. of Nijmegen, to be published)

[30] H.Wind, "Evaluating a magnetic field component from boundary observations only". NIM 84(1970)117-124

[31] H.Wind (CERN), You-Hua Hu (Beijing), MAGFIT2. CERN computer library no W1043.

[32] A.C.König, C.Brouwer. "Loading Scheme for the L3 magnetic field measurement system", Univ. of Nijmegen, HEN 290

[33] A.Konig, University of Nijmegen, private communication.

[34] H. Lubbers, D.J. Schotanus. "The magnetic field in the L3 detector and the size of the doorgaps" (Univ. of Nijmegen, HEN 314)

[35] Piuz. "Measurement of the longitudinal diffusion of a single electron in gas mixtures used in proportional counters". NIM 205(1983)425-436

[36] F. Fulda-Quenzer *et al.* , Laboratoire de l'Accélérateru Linéaire, LAL 84/38

[37] F.Hartjes *et al.* , "Diffusion measurements in drift gases", NIM A276(1989)582.

[38] L.G.H.Huxley and R.W.Crompton. "The diffusion and drift of electrons in gases". Wiley Series in Plasma physics, 1974.

[39] W.H.Dijkman, "A system for removing both oxygen and nitrogen from a rare gas-hydrocarbon mixture". NIM A274(1989)171-176

[40] A. van Vucht. Afstudeerverslag Univ. van Amsterdam, 1988.

[41] J. Branson, T. Jie, "Fitting the muon chamber cell map". Muon chamber internal report 86-1, (May 1986).

[42] S. Nagaoka, "Drift Properties of the L3 muon chambers in a magnetic field measured with an UV laser". Afstudeerverslag Univ. Amsterdam (1989)

[43] H. van der Graaf and J.P. Wagenaar, "A calculation in three dimensions of the induced charge on the electrodes of an MWPC", NIM 217(1983)330

[44] H. van der Graaf and J.P. Wagenaar, "Numerical results of calculations in three dimensions of the induced charge in MWPC's", NIM A252(1986)311

[45] T. Foreman, "Description of the cellmap function and its iverse", L3 internal note, NIKHEFH 1989.

Summary

The subject of high energy physics is the study of the ultimate constituents of matter and the fundamental interactions between them. Experiments are carried out by letting a high energy particle beam collide with a fixed target, or with another particle beam, and studying the reaction products in a detector. One of the latest colliders developed for experimental high energy physics is the Large Electron (e^-) Positron (e^+) facility (LEP) at CERN; L3 is one of the four detectors at LEP. L3 itself consists of many parts, each of which measures a specific property of the particles produced in the collisions. The behaviour of the L3 muon drift chambers in a magnetic field is the main subject of this thesis.

In chapter 1 the different parts of the L3 detector are described in some detail. One of the specialities of the L3 detector is the high precision measurement of the momenta of the muons produced in the e^-e^+ collisions. The L3 muon spectrometer consists of 80 large drift chambers divided over three layers that fill a cylindrical volume of 12 meter in length, 5 meter inner diameter and 12 meter outer diameter. The whole detector is placed inside a magnetic field of about 0.5 Tesla in order to curve the muon trajectories. The curved track is measured at three points in the three layers of muon chambers. From the curvature of the particle tracks the corresponding momenta are calculated.

Chapter 2 deals with the magnetic field of the L3 detector. First the effects of errors in the magnetic field upon the error in the muon momentum measurement are discussed. The L3 magnetic field will be measured during run time with magnetic probes mounted on the detector surfaces. This chapter describes 2- and 3-dimensional simulations of the field, which were used to determine the magnetic field probe positions and to test the magnetic field reconstruction algorithms. Several methods to reconstruct the magnetic field at any point in the detector from the (≤ 1000) probe readings are presented, together with preliminary results of the reconstruction of 2-dimensional simulations.

In chapter 3 results of different drift velocity and diffusion measurements are presented. The drift velocity as function of the electric field has been measured at B=0.5 Tesla. This measurement is important in order to determine the plateau value, where the drift velocity dependence on the electric field variations is minimal. The dependence of the drift velocity on the N_2 concentration and the longitudinal diffusion as function of electric field have been measured at B=0 Tesla.

In chapter 4 various effects that play a role in the drift time - drift distance relation $X(t)$ are discussed. An algebraic form for $X(t)$ is presented that contains the effects of

pressure, temperature and magnetic field variations, as well as some geometrical effects. A small test chamber was constructed in order to measure the parameters in this relation in a testbeam experiment performed at one of the SPS testbeams at CERN. A translation table for the chamber was produced at ETH-Zürich and silicon strip detectors made at the Physics Institute Zeuthen were used for external beam definition. The setup of this experiment is described in the second part of chapter 4.

In chapter 5 the analysis and results of the testbeam data are presented. Different forms of the drift time - drift distance relation $X(t)$ were fitted to the testbeam data and compared. The simplest form that will be generally applicable has only 18 parameters and results in fit errors smaller than 25 μm. At the end of chapter 5 it is shown that the testbeam data contained some systematic errors. A technique is suggested to remove these final systematic errors. This technique will also be applicable to the real L3 muon chamber data, both to remove such errors, and to refit a few parameters in order to compensate for the differences between the real chambers and the test chamber. The relation $X(t)$, together with the values of the parameters as fitted from the test beam data, is integrated in the L3 reconstruction software.

Samenvatting

Het zoeken naar de elementaire bouwstenen van de materie en naar de krachten tussen deze bouwstenen is het onderwerp van de hoge-energiefysica. Experimenten worden uitgevoerd door in een versneller hoog energetische deeltjes te laten botsen met een doelwit of met andere versnelde deeltjes en de bij deze botsingen vrijkomende producten te bestuderen in een detector. Een van de laatste versnellers die voor dit doel gebouwd is, is de Large Electron Positron (LEP) collider te CERN; L3 is één van de vier detectoren die bij LEP gebouwd worden. Het gedrag van de L3 muon driftkamers in een magnetisch veld is het belangrijkste onderwerp van dit proefschrift.

In hoofdstuk 1 wordt nader ingegaan op de verschillende delen van de L3 detector. Een van de specialiteiten van L3 is het nauwkeurig meten van de impuls van bij de botsingen vrijgekomen muonen. De L3 muon spectrometer bestaat uit 80 grote driftkamers, verdeeld over drie lagen die een cylindrische ruimte vullen van 12 meter in lengte, 5 meter binnendiameter en 12 meter buitendiameter. De hele detector is geplaatst in een magnetisch veld van 0.5 Tesla om de banen van de muonen af te buigen. Met behulp van de drie lagen van muonkamers worden van deze kromme baan drie punten gemeten. Uit de mate van kromming wordt de impuls van de deeltjes berekend.

Hoofdstuk 2 behandelt het magneetveld van L3. Eerst wordt ingegaan op de invloed van fouten in het magneetveld op de nauwkeurigheid van de impulsmetingen. Het L3 magnetisch veld zal tijdens de experimenten worden gemeten met magnetische detectoren die op de muonkamers zijn gemonteerd. In dit hoofdstuk worden de resultaten van 2- en 3-dimensionale simulaties van het magneetveld gepresenteerd die gebruikt zijn om de verdeling van de magneetprobes te bepalen en om de reconstructiemethodes te testen. Verschillende methodes om het magneetveld in een willekeurig punt van de L3 detector te bepalen met behulp van de minder dan 1000 veld metingen worden besproken.

In hoofdstuk 3 worden verschillende driftsnelheids- en diffusiemetingen gepresenteerd. De driftsnelheid is gemeten als functie van het electrische veld in een magneet veld van 0.5 Tesla. Deze meting is belangrijk om de plateauwaarde te bepalen, waar de driftsnelheid het minst afhankelijk is van variaties in het electrische veld. De invloed van de N_2 concentratie in het driftgas op de driftsnelheid, en de longitudinale diffusie als functie van het electrische veld, zijn gemeten bij B=0 Tesla.

In hoofdstuk 4 worden verschillende belangrijke effecten besproken die een rol spelen in de drifttijd - driftafstandsrelatie $X(t)$. Er wordt een algebraïsche vergelijking voor $X(t)$ gepresenteerd die de $X(t)$ afhankelijkheid van druk, temperatuur, magneetveld en

van geometrische effecten beschrijft. Er is een kleine testkamer geconstrueerd waarmee in een testbeam van de SPS te CERN metingen zijn gedaan om de parameters in $X(t)$ te kunnen bepalen. De gebruikte opstelling wordt besproken in de tweede helft van hoofdstuk 4.

In hoofdstuk 5 worden de resultaten van het testbeamexperiment besproken. Verschillende vormen van de drifttijd-driftafstandsrelatie zijn gefit aan de data en vergeleken. De simpelste algemeen toepasbare vorm van $X(t)$ heeft slechts 18 parameters en resulteert in fitfouten van minder dan 25 μm. Aan het einde van hoofdstuk 5 wordt ingegaan op in de testbeam data gevonden systematische fouten. Er wordt aangegeven hoe die fouten vermeden kunnen worden. De gebruikte methode zal ook voor de echte L3 driftkamerdata kunnen worden gebruikt om voor dit soort fouten te corrigeren. De methode maakt het tevens mogelijk om verschillen tussen de echte en de model driftkamers te compenseren door een paar parameters opnieuw te fitten. De relatie $X(t)$, met de uit de testbeam data bepaalde parameters, is geintegreerd in de L3 reconstructiesoftware.

Acknowledgements

The work described in this thesis is the result of a combined effort of many people. I would like to mention some of them by name, at the risk of doing injustice to the help of many others.

Jaap Schotanus, Frans Crijns, Adriaan König, Klaus Freudenreich and Dave Luckey have contributed to the work on the L3 magnetic field described in chapter 2. I would like to thank J. Simkin from VECTOR FIELDS for his free help on TOSCA, even though at that time we did not plan to buy a copy of his program. Rutherford Appleton Laboratory generously made available their computer facilities for my attempts to get acquainted with this package. I should also mention prof. H. Hofer from ETH-Zürich who made it possible for me to work on the Swiss super computer facilities at Lausanne and SIN.

The measurements described in chapter 3 were performed with the help of Fred Hartjes, partly at NIKHEF and partly at CERN. Fred also introduced me into the art of adapting (electronic-) hardware to my specific wishes.

Many people of the L3 muon chamber group have contributed to the testbeam experiment. Large contributions came, among others, from Jim Branson, Torre Wenaus, Konrad Deiters, Luis Martinez and Enrique Gonzalez. I wish to thank the mechanical and electronical workshops at NIKHEF where the test chamber and readout electronics was produced, ETH-Zürich for the moving table and the Physics Institute Zeuthen (DDR) for the silicon strip detector system.

Finally I would like to thank my two promotors, prof. D. Harting and prof. J. Branson, for reading my manuscript several times and for the many discussions both on physics and beyond.